Master's thesis

NTNU
Norwegian University of Science and Technology
Faculty of Engineering
Department of Mechanical and Industrial Engineering

Giulia Collina

Consequences associated to the Boiling Liquid Expanding Vapour Explosion for liquid hydrogen tanks: assessment and mitigation

Master's thesis in Reliability, Availability, Maintainability and Safety
Supervisor: Professor Nicola Paltrinieri
Co-supervisor: Professor Federico Ustolin, Leonardo Giannini
January 2023

NTNU
Norwegian University of Science and Technology

Giulia Collina

Consequences associated to the Boiling Liquid Expanding Vapour Explosion for liquid hydrogen tanks: assessment and mitigation

Master's thesis in Reliability, Availability, Maintainability and Safety
Supervisor: Professor Nicola Paltrinieri
Co-supervisor: Professor Federico Ustolin, Leonardo Giannini
January 2023

Norwegian University of Science and Technology
Faculty of Engineering
Department of Mechanical and Industrial Engineering

NTNU
Norwegian University of
Science and Technology

Abstract

Nowadays the urgency to address climate change and global warming is growing rapidly: the industry and the energy sector must be decarbonized. Hydrogen can play a key role in the energy transition: it is expected to progressively replace fossil fuels, penetrating economies and gaining interest from the public. However, this new possible energy scenario requires further investigation on safety aspects, which currently represent a challenge. The present study aims at making a little contribution to this field. The focus is on the analysis and modeling of hazardous scenarios concerning liquid hydrogen. The investigation of BLEVEs (*Boiling Liquid Expanding Vapor Explosion*) consequences lies at the core of this research: among various consequences (overpressure, radiation), the interest is on the generation and projection of fragments. The goal is to investigate whether the models developed for conventional fuels and tanks give good predictions also when handling hydrogen.
The experimental data from the SH_2IFT - *Safe Hydrogen Fuel Handling and Use for Efficient Implementation* project are used to validate those models. This project's objective was to increase competence within safety of hydrogen technology, especially focusing on consequences of handling large amounts of this substance.

Contents

List of Figures

List of Tables

Acronyms

AICHE	American Institute of Chemical Engineers
BLEVE	Boiling Liquid Expanding Vapour Explosion
BOG	Boil-off gas
CFD	Computational Fluid Dynamics
CFF	Considering Fluid Dynamic Forces
CGH_2	Compressed gaseous hydrogen
ETA	Event tree analysis
FEM	Finite Element Method
HDPE	High denisty polyethylene
IGB	Ideal Gas Behaviour
LFL	Lower Flammability Limit
LH_2	Liquid hydrogen
LNG	Liquified natural gas
LOC	Loss of Containment
LPG	Liquified petroleum gas
MLI	Multilayer insulation
NFF	Neglecting Fluid Dynamic Forces
RGB	Real Gas Behaviour
SH_2IFT	Safe Hydrogen Fuel Handling and Use for Efficient Implementation
UFL	Upper Flammability Limit
(U)VCE	(Unconfined) Vapour Cloud Explosion
QRA	Quantitative Risk Analysis

Symbols

T_{sl}	Superheat limit temperature
P_o	Atmospheric pressure
P_{exp}	Pressure before explosion
V^{*}	Expanding volume of the fluid
γ	Specific heat ratio
T_c	Critical temperature
T_0	Liquid phase temperature inside the vessel before the explosion
T_b	Boiling temperature
$\Delta h_{v,0}$	Latent heat of vaporisation at boling point
M_v	Mass of the vessel
E_{av}	Available energy after the explosion
g	Gravitational acceleration
v_i	Initial velocity of fragment
M_F	Mass of fragment
ρ_v	Vapour phase density
ρ_l	Liquid phase density
$c_{p,L0}$	Specific heat of the liquid at the boiling temperature
V_{TANK}	Volume of outer tank
$m_{H2_{LIMIT}}$	Lower limit of hydrogen mass before the explosion
$m_{H2_{INITIAL}}$	Initial value of hydrogen mass
m_l	Mass of liquid before the explosion
M_l^{ft}	First try liquid mass
V_l^{ft}	First try liquid volume
V_v^{ft}	First try vapour volume
M_v^{ft}	First try vapour mass
M_l^{st}	Second try liquid mass
u_{vis}	Specific internal energy after the isoentropic expansion (vapour)
u_{lis}	Specific internal energy after the isoentropic expansion (liquid)
x_v	Entropy ratio (vapour)
x_l	Entropy ratio (liquid)

E_{av}	Mechanical energy released from the explosion
λ	Mechanical energy fraction for fragment generation
v_i	Fragment initial velocity
R	Fragment horizontal range
α	Fragment initial angle
C_D	Drag coefficient
A_D	Drag area
C_L	Lift coefficient
A_L	Lift area
$\bar{v}_i$	Dimensionless velocity (CFF method)
ρ_a	Air density
$\bar{R}_i$	Dimensionless range (CFF method)
d_v	Vessel diameter
A_{strip}	Area of the plate fragment
d_{F-V}	Distance between fragment no. 4 and propane tank
d_{F-T}	Distance between fragment no. 4 and LH2 vessel
δ_{OV}	Outer vessel thickness
δ_{IV}	Inner vessel thickness
ρ_{OV}	Outer vessel density
ρ_{IV}	Inner vessel density
$R_{OV,IV}$	Radius of the inner, or outer vessel
C_{DA} C_{DB} C_{DC} C_{DD}	Factors for drag coefficient
x_1 x_2	Fragments coordinates
δt	Frame rate of the camera
n	Frame number
v_{exp}	Experimental initial velocity of fragments
R_{exp}	Experimental horizontal range

1 Introduction

The 21^{st} century appears to be a period in need of change. Environmental pollution, global warming, and climate change are the most debated challenges of this period, both within the scientific community and in public society. Agreements such as the UNFCCC (United Nations Framework Convention on Climate Change), the Kyoto Protocol, and the Paris Agreement have been established to address the issue of human-induced climate change. Countries are now more determined than ever to achieve decarbonization. The main goal is to replace fossil fuels with more environmentally friendly and renewable energy sources and carriers.

In June 2019, the International Energy Agency (IEA) declared in its report titled "The Future of Hydrogen" [1]: "the time is right to tap into hydrogen's potential to play a key role in a clean, secure and affordable energy future". Hydrogen is the most suitable candidate to to partly replace fossil fuels. It is a valuable energy carrier since it has a high gravimetric energy content (118.8 MJ/kg [2]); it is not toxic, it has a carbon neutral combustion reaction, meaning its combustion produces just water and not carbon dioxide, and it can also be renewable, in the sense that its production and use not impactful on the environment.
However, the implementation of hydrogen in several sectors faces a number of safety issues. Hydrogen is the smallest existing molecule, it can escape through microscopic holes, making it difficult to contain. Furthermore, it is extremely flammable: its minimum ignition energy is 0.017 mJ and its flammability range in air is 4 - 75%vol [3], [4]. Additionally, it can be corrosive to certain materials commonly used in fuel systems. More specific hazards are related to the peculiar storage conditions required since it is the lightest existing molecule, with a density of 0.0899 kg/m^3 at 0°C and 1 atm [5]. It is not feasible to transport large quantities in these conditions: it must be compressed or liquefied to increase its storage capacity. The compression process up to 700 bar leads to a density value of 40 kg/m^3 [5]; the liquefaction process at 20.3 K can increase the density up to 70.9 kg/m^3 [6]. Depending on the type of storage, several final accident scenarios may occur, as it will be explained in the following chapters.

The willingness to expand the range of applications of hydrogen requires a thorough investigation of safety aspects. In recent years, research attention has shifted in this direction: proof of this is the SH_2IFT - *Safe Hydrogen Fuel Handling and Use for Efficient Implementation* project, whose purpose is the analysis of the consequences of liquid hydrogen catastrophic release.
This thesis project follows the same line and focuses on the study and modeling of hazardous scenarios concerning liquid hydrogen, starting from the experimental activities conducted during the aforementioned project. The mentioned experiments concern a catastrophic explosion following the loss of integrity of a liquid hydrogen cryogenic vessel engulfed in propane flames. To be more specific, these kinds of explosions are usually referred as BLEVE (*Boiling Liquid Expanding Vapor Explosion*), which is considered an *Atypical Accident Scenario* [7], since its probability to happen is low. BLEVEs involve the violent expansion of both the vapor and the liquid phases. Like many types of explosions, the consequences include the generation of a shock wave, the projection of the fragments of the blasted tank, and a potential fireball, in case of a flammable substance.

The main focus of this thesis is to analyse of the fragments developed after the catastrophic rupture of the hydrogen tank. Most relevant aspects to be considered during the consequence analysis are the horizontal distribution of the fragments and the horizontal range since they are key parameters to the definition of the hazardous distance. This analysis stems from an interest in investigating whether the models developed for conventional fuels and tanks give good predictions also when it comes to hydrogen.
The first stage of the analysis involves the observation and processing of experimental data; the second stage focuses on the attempt to validate the models for the horizontal range estimation. Finally, the topic of mitigating consequences is addressed.

2 State of the art

In the first part of this chapter, an overview of different hydrogen storage methodologies is proposed. From these, the major accident hazards that can arise from hydrogen storage are described. A more detailed description is provided for the *Boiling Liquid Expanding Vapor Explosion* (BLEVE) accident scenario that is considered as atypical. In order to estimate the consequences related to the production of fragments, the models available in the literature for assessing the mechanical energy released by an explosion and those for assessing the distance traveled by fragments are described at the end of this chapter.

2.1 Hydrogen storage

Molecular hydrogen is a gas having an extremely low molecular weight and with a density of 0.0899 kg/m^3 at 0°C and 1 atm [5]. Hydrogen has an excellent gravimetric energy density with a lower heating value (LHV) of 118.8 MJ/kg [2], but it possesses a very low volumetric energy density of approximately 10.7 kJ/L [2] at ambient conditions (temperature and pressure of 20°C and 1 atm, respectively). These characteristics pose the largest challenge in hydrogen utilization; therefore, developing and adopting an effective storage method for hydrogen is crucial.

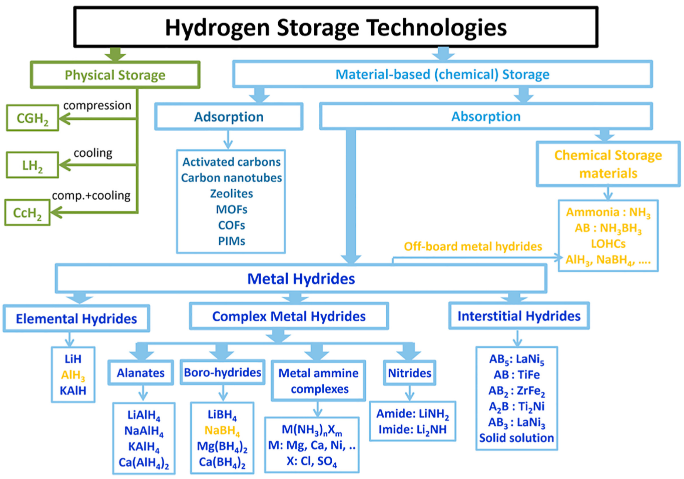

Figure 2.1: Hydrogen storage processes [5].

As shown in Figure 2.1, there is a large number of hydrogen storage technologies today that can be divided into physical and chemical. However, a more detailed description is provided only for physical storage methods.

2.1.1 Compressed gaseous hydrogen

High pressure storage is one of the most accomplished way to store hydrogen [5]. As pressure increases from 1 o 700 bar, the hydrogen density increases from 0.1 kg/m^3 to 40 kg/m^3 and consequently energy volumetric density increased from 3.3 kWh/L to 1320 kWh/m^3 respectively [5].
Cylindrical vessels are generally used for this technology, but they can also be polymorph, toroid or spherical. There are four different types of tanks for this type of application [8]:

- Type I: fully metallic (normally aluminum or steel) pressure vessels. This is the most conventional, least expensive and can withstand up to 50 MPa;
- Type II: steel pressure vessel with a glass fiber composite overwrap. It is more expensive than type I ($\sim$ 50 times higher) but it is lighter ($\sim 30-40$ times less) and it offers the highest pressure tolerance;
- Type III: full composite wrap (carbon fiber composite for structural load) with metal liner (aluminum for sealing purpose). It weighs half as much as type II but costs twice as much and it has proven to be reliable for 45 MPa working pressure;
- Type IV : fully composite (typically high denisty polyethylene - HDPE - as liner and carbon fiber or carbon-glass composites for structural load). The price is high but it is the lightest of all types and it can bear pressures up to 100 MPa.

The schematics of these types of tanks are shown in Figure 2.2.

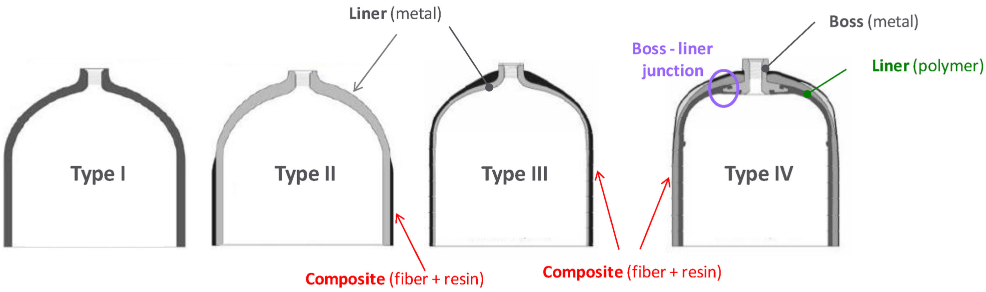

Figure 2.2: Representation of type I, II, III and IV [9].

2.1.2 Liquid hydrogen

The liquefaction process can increase the hydrogen density up to 70.9 kg/m^3 at ambient pressure and 20.3 K (-253 °C) [6], leading to a reduction in the volumes required for transport with obvious advantages. Nowadays hydrogen liquefaction and storage are very well developed technologies that have been used for decades, mostly for space applications and petrochemicals; the main drawback of this technology is that the process is both time consuming and energy intensive: indeed, up to 35% of the energy content can be lost in the process [10], compared to about 10% energy loss in compressed gaseous hydrogen storage. Another disavdantage is that liquid hydrogen (LH2) is difficult to store over a long period due to the boil-off gas (BOG) formation; for this reason, hydrogen is most often converted from normal composition (75% ortho-hydrogen, 25% para-hydrogen) to 100% para-hydrogen both to increase stability and to reduce evaporation [11]. In addition to the ortho-para transition, two different alternatives are available to handle storage at 20.3 K (-253 °C): usually LH2 tanks have highly efficient insulated (vacuum) vessels and sometimes vapour cooled shields, exploiting the cold BOG to refrigerate the tank contents.

Double-walled vacuum insulated vessels

Double-walled vacuum insulated vessels are illustrated in Figure 2.3 and consist of an inner pressure vessel and an outer vessel. In order to reduce the thermal conductivity

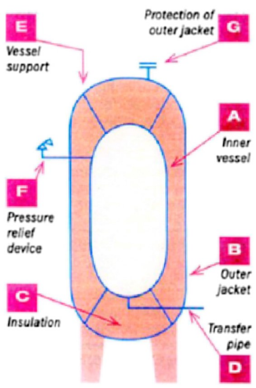

Figure 2.3: Illustration of a double jacket sotrage [9].

of the space between the inner and the outer vessel, perlite (powder structure) or multilayer insulation (wrapping with layers of aluminium and polymer films) are used. To reduce thermal conductivity even further, the part between the two tanks is vacuum held: the effect of this choice can be seen in Figure 2.4. The part between the two vessels where there is insulation is called vacuum jacket.

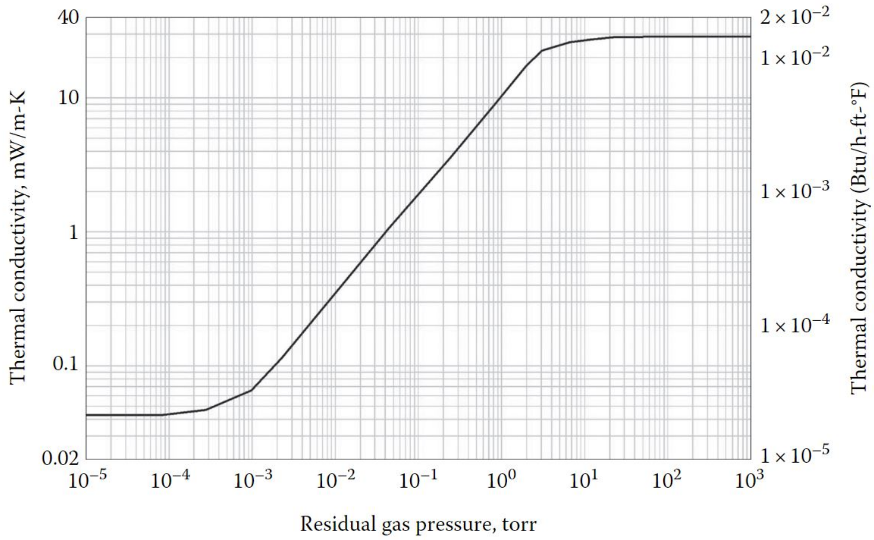

Figure 2.4: Variation of the thermal conductivity with residual gas pressure for a typical Multi-layer Insulation (MLI) [12].

2.1.3 Cryo compressed hydrogen

This technology combines properties of both compressed gaseous hydrogen and cryogenic hydrogen storage systems. It requires hydrogen to be stored at cryogenic temperatures and high pressures (at least 30 MPa). The graph in Figure 2.5 shows how convenient this technology is from the point of view of the density.

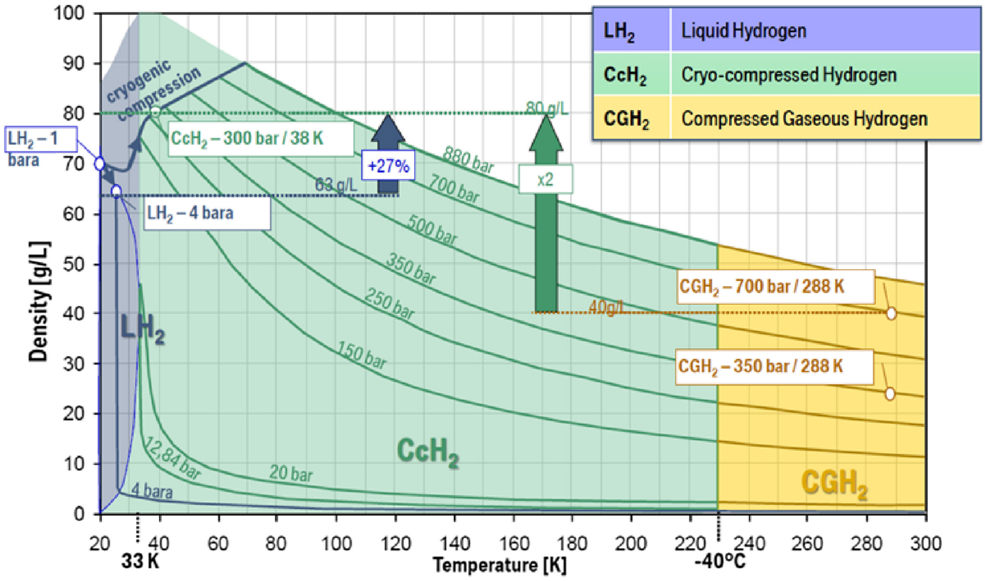

Figure 2.5: Hydrogen density versus pressure and temperature [13].

2.2 Possible hazards

Before going any further, it is necessary to clearly define what is meant by the concept of *hazards*: "an inherent chemical or physical characteristic that has the potential for causing damage to people, property, or the environment" [14]. It is therefore clear that this concept is different from the definition of *risk*: "a measure of human injury, environmental damage, or economic loss in terms of both the incident likelihood and the magnitude of the injury or loss" [14]. The safety aspect is a crucial point in the development of hydrogen technologies because of its special properties. This is why it is necessary to mention the properties in question before describing the hazards involved: first of all, hydrogen is odourless and colourless, making it difficult to detect. What makes hydrogen more dangerous than current fuels is:

- Flammability range (4 - 75 %vol): the values of concentrations of the flammable vapors in air for which the mixture flammable-air burns if ignited. This range is delimited, by the flammability limits: LFL (Lower Flammability Limit) and UFL (Upper Flammability Limit). It is evident that the wider the flammability range, the more hazardous is the substance.

- Denotability range (13 - 59 %vol): the values of volumetric fraction required to generate a detonation, which leads to much harsher consequences.

- Minimum ignition energy (0.02 mJ): minimum energy necessary to ignite a mixture flammable air having a specific composition and in specific pressure and temperature conditions.

The hazardous properties of hydrogen are compared to those of two current fuels in the following table:

Table 2.1: Comparison of fuels properties [3] [4].

Property	**Hydrogen**	**Methane**	**Gasoline**
Flammability limits in air (% vol)	4 - 75	5 - 15	1 - 7.6
Detonability limits in air (% vol)	13 - 59	6.3 - 14	1.1 - 3.3
Minimum ignition energy (mJ)	0.02	0.29	0.24

In addition, more specific hazards are related to storage conditions (Section 2.1) and arise from high pressure, low temperature or a combination of the two.

2.2.1 Overview of final accident scenarios

Hydrogen safety aspects can be investigated using event tree analysis (ETA), an inductive procedure that shows all possible outcomes resulting from an accidental event (top events). In the tree there is a branch - the release - and a series of nodes, each corresponding to an intermediate event. From each node, two branches depart; the upper branch corresponds to the occurrence of the event associated with the node, the lower branch to its non-occurrence. When it comes to hydrogen, the top events correspond to releases or loss of containment (LOC) that are either instantaneous (t<10min), like a catastrophic rupture of a vessel, or continuous (t>10min), like a leak from a hole. The intermediate event are: direct ignition, delayed ignition and containment. The final accident scenarios can be divided into fires and explosions. Clearly the use of this tool provides different results depending on the physical state of hydrogen (liquid or gaseous) as it is shown in the following figures.

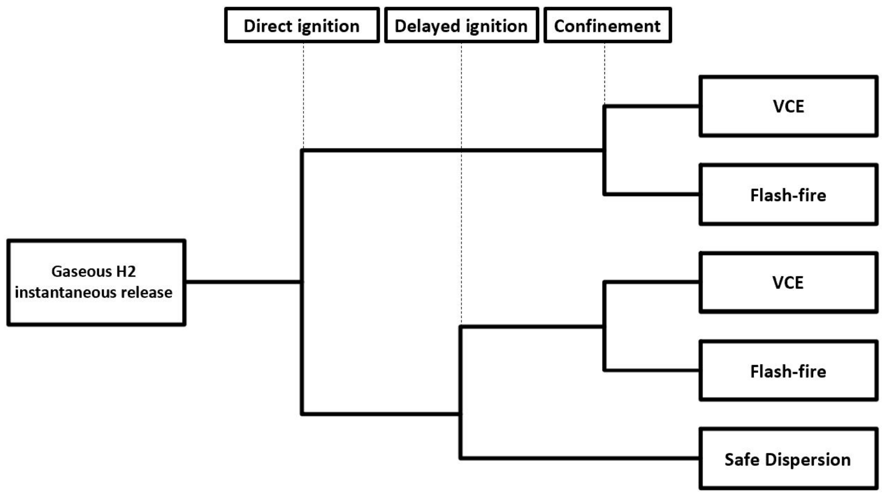

Figure 2.6: Event tree for a gaseous instantaneous release.

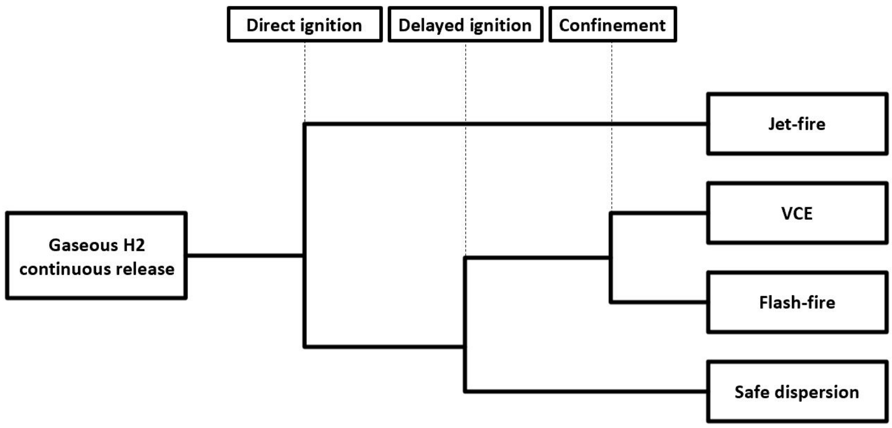

Figure 2.7: Event tree for a gaseous contineous release.

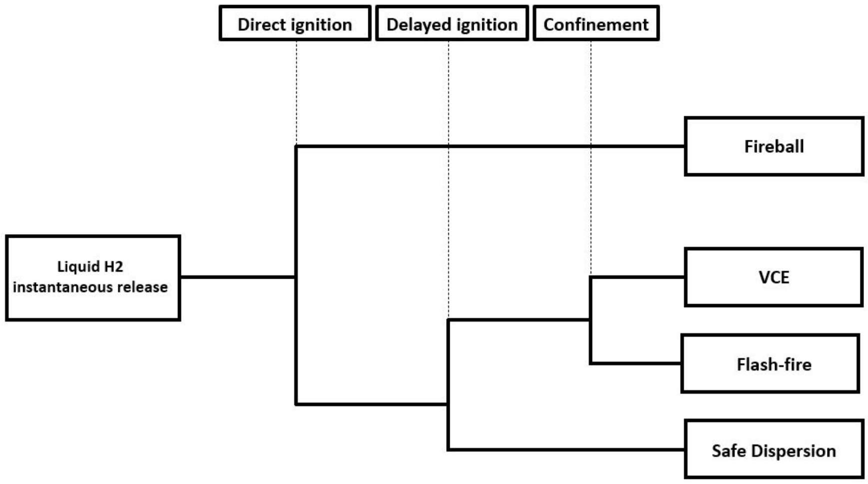

Figure 2.8: Event tree for a liquid instantaneous release.

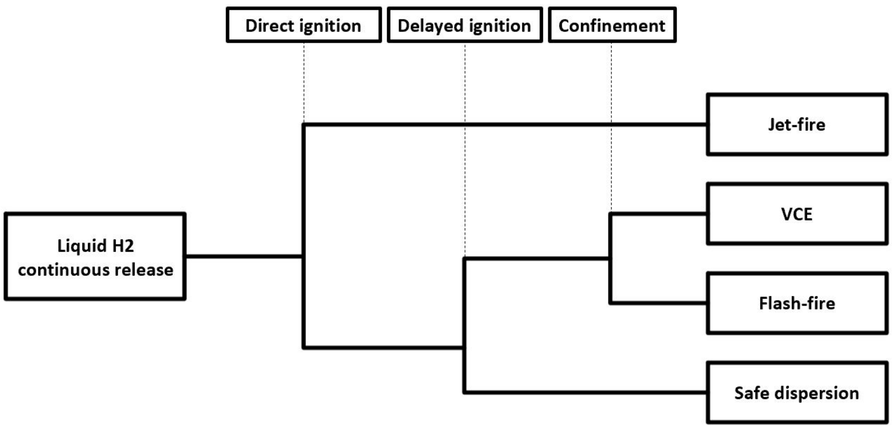

Figure 2.9: Event tree for a liquid contineous release.

Fire

Fire is an undesired or uncontrolled combustion reaction accompanied by the release of thermal energy, flames and eventually smoke. The harmful effects of fires are direct contact with the flame and radiation outside the flame. In the process industry there are four different types of fires:

- Pool-fire: can occur as consequence of leaks and spills if they lead to the formation of a liquid pool that is ignited (see Figure 2.10).
- Jet-fire: can arise from releases of gaseous, flashing liquid (two phase) and pure liquid inventories. It is a turbulent diffusion flame resulting from the combustion of a fuel continuously released with some significant momentum in a particular

Figure 2.10: Example of LNG pool-fires experiment [15].

direction or directions (see Figure 2.11).

Figure 2.11: Example of a liquid hydrogen jet-fire [16].

- Fireball: a fire caused by the immediate ignition of a flammable aerosol mass (see Figure 2.12; it is often generated by a BLEVE (see Subsection 2.2.2).
- Flash-fire: a brief fire from the ignition of a flammable cloud.

Explosion

Explosion is a phenomenon involving a release of energy in a very short time (1ms [18]) and usually in a very small space, and associated with a pressure wave having the characteristics of a blast wave (see Figure 2.13). Explosions are primarily categorised into physical (bursting of a vessel containing a pressurised fluid) and chemical (chemical reaction against a fluid). Chemical explosions can be classified as either confined or unconfined vapour cloud explosions (UVCE) and also as deflagrations or detonations depending on the flame front speed. The harmful effects of explosions are overpressure and projection of missiles: the vessel is shattered and its pieces are propelled outwards

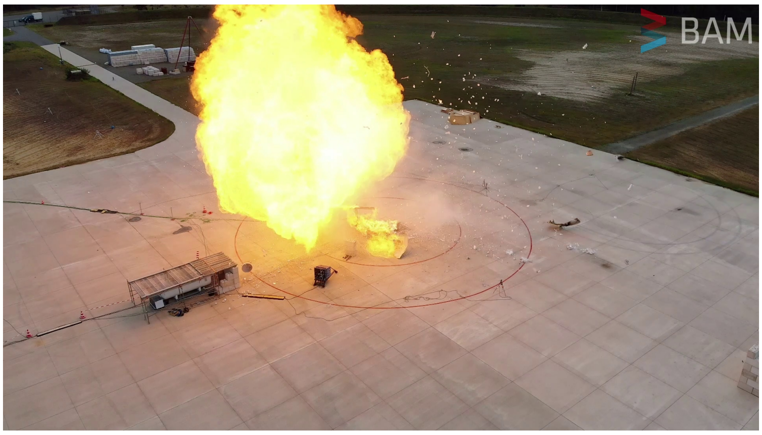

Figure 2.12: Liquid hydrogen fireball [17].

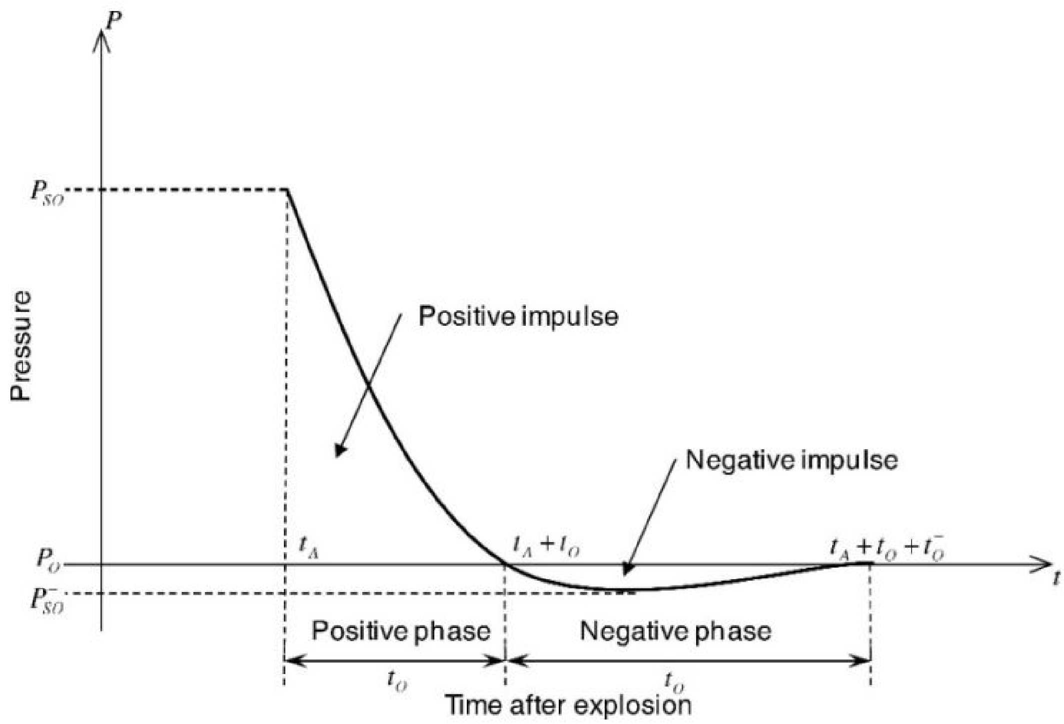

Figure 2.13: Shock wave pressure [19].

at high velocities in all directions. These missiles may cause fatalities, injuries and asset damage; moreover, the interaction of the projected fragments with specific target equipment may result in secondary accidents, escalating to domino scenarios [20].

2.2.2 Boiling Liquid Expanding Vapor Explosions

Boiling Liquid Expanding Vapor Explosion (BLEVE) is a physical explosion, the most general and correct definition of which is: "A BLEVE is the explosion of a vessel containing a liquid (or liquid plus vapor) at a temperature significantly above its boiling point at atmospheric pressure" [21]. In Figure 2.14a, a vessel containing a liquid in equilibrium with its vapour phase is shown; it is at temperature T and a generic pressure P>P_o. Figure 2.14b shows what can happen when the vessel undergoes rapid depressurisation to P_o: thermal equilibrium, by contrast to mechanical equilibrium, is not reached immediately, so the superheated liquid reaches a metastable state (T, P_o). At the end the thermodynamic equilibrium is reached because a part of the liquid vaporises in order to make the system temperature the same as the saturation temperature (T_o), as shown in Figure 2.14c. This phenomenon can occur whether there

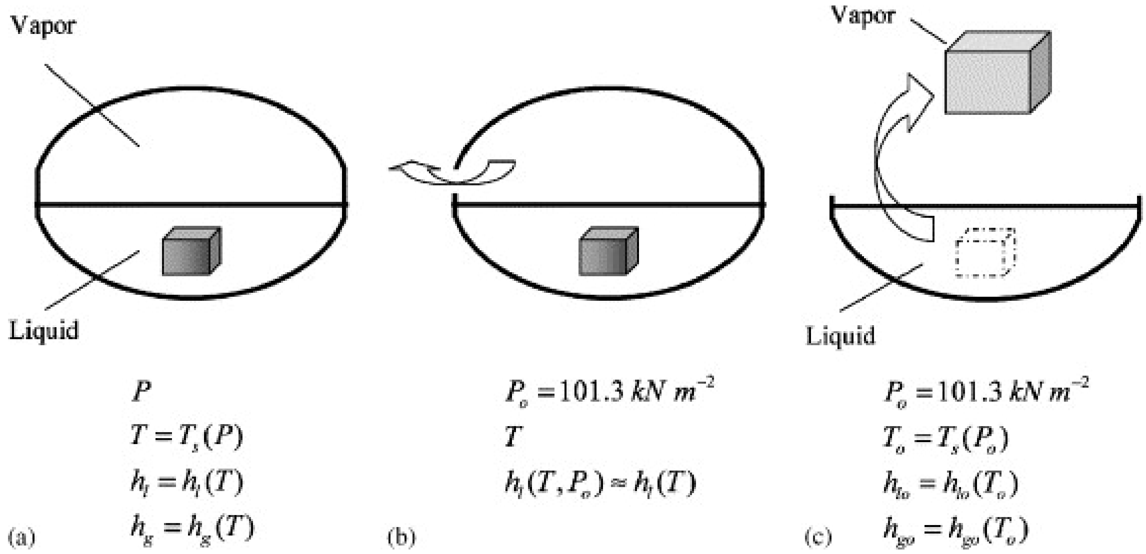

Figure 2.14: A hot liquid undergoing sudden depressurisation in a tank [22].

is a flammable or non-flammable substance in a tank: in the first case, the explosion is followed by a fireball; thus the aftermaths of BLEVEs are the blast wave generated by the expansion of the compressed vapour phase and the flashing of the liquid, the debris of the vessel but also the radiation due to the fire. This event is well known and described for many substances, such as ammonia, propane, LPG and LNG, since several accidents occurred in the period 1926-2004 (see Table 2.2).
The BLEVEs have been categorised in "fired" or "unfired" depending on the cause of the loss of containment [25]:

- fired (or "hot") BLEVE occurs when a vessel is engulfed by an external fire; to evaporation of the substance and thus to an increase in internal pressure. At the same time, in addition to the stress due to the increase in pressure, the rise in temperature weakens the tank material, affecting its mechanical properties.

- unfired (or "cold") BLEVE is not thermally induced and it is caused by a pressure relief failure or by a violent impact, such as a road accident or domino effect due to fragments from a nearby explosion.

Table 2.2: List of BLEVE in the period 1926-2004 [23], [24].

Substance	**Classification**	**No. of accidents**	**Fatalities**	**Injured**
Propane	Flammable	24	121	7761
LPG	Flammable	17	12	35127
Chlorine	Toxic	7	139	-
Ammonia	Toxic	6	55	25
Butane	Flammable		394	7510
Gasoline	Flammable	3	10	2
Acrolein	Flammable	2	-	-
Carbon dioxide	Non-flammable, non-toxic	2	9	-
Ethylene oxide	Flammable	2	1	5
LNG	Flammable	2	14	76
Propylene	Flammable	2	213	-
Vinyl chloride	Flammable, toxic	2	1	50
Borane-tetrahydrofuran	Flammable, toxic	1	-	2
Butadiene	Flammable, toxic	1	57	-
Chlorobutadiene	Toxic	1	3	-
Ethyl ether	Flammable	1	209	-
Hydrogen	Flammable	1	7	-
Isobutene	Flammable	1	-	1
Maltodextrin and other chemicals	Toxic	1	-	-
Methyl bromide	Toxic	1	2	-
Nitrogen	Non-flammable, non-toxic	1	-	-
Phosgene	Toxic	1	11	171
Steam	Non-flammable, non-toxic	1	4	7
Water	Non-flammable, non-toxic	1	7	-

Superheat limit temperature theory

In the past, there was a strong theory introduced by Reid ([26]) that BLEVEs can only occur if the liquid is at a temperature above the superheat limit temperature: the temperature above which a substance cannot exist in liquid phase, and it varies with pressure and, of course, depends on the type of the substance. Therefore, each substance has its own *spinoidal curve*, which is the locus of points of T_{sl} at different pressures (see Figure 2.15). Nevertheless, it should be taken into account that T_{sl} is an interesting parameter because at this value correspond the maximum energy transferred adiabatically between the cooling liquid and the vaporizing liquid fractions [21]. Furthermore, having demonstrated experimentally that the explosion can occur even below the T_{sl}, this theory is still adopted to determine the conditions under which a BLEVE may occur.There are several methods in the literature to estimate this value [7].

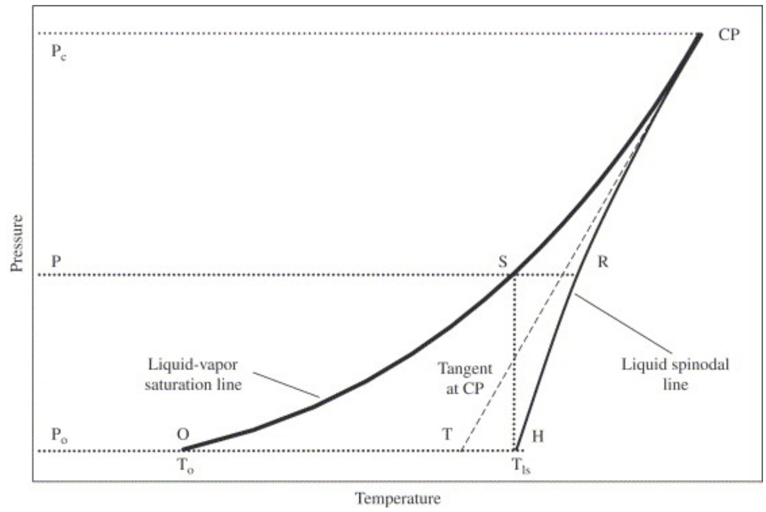

Figure 2.15: Liquid spinodal curve and tangent to the saturation line at the critical point [22].

BLEVE is defined as an atypical scenario ("scenario deviating from normal expectations of unwanted events or worst case reference scenarios and, thus, not deemed credible by the common processes applied for risk assessment" [27]). Indeed, few LH_2 BLEVE accidents can be found in the literature [7]; a first example could be the explosion of the S-IV All Systems Vehicle occurred on January 24, 1964, at the Douglas Aircraft Company, Sacramento. A LH_2 BLEVE accident occurred on January 1st, 1974 and a hot LH_2 BLEVE took place during the Challenger space shuttle disaster in 1986. As far as experiments are concerned, BMW has carried out LH2 BLEVE tests in the period 1992-95 [28]. One of the aims of the *SH2IFT* project (Safe Hydrogen Fuel Handling and Use for Efficient Implementation) is to fill this knowledge gap through some experiment whose intention is to cause an explosion [17].

2.3 Fragment models

A vessel rupture is coupled with the release of the contents and the release of the internal energy. The internal energy is converted into mechanical energy and it is the responsible of damaging shock waves and high velocity fragments. Therefore the blast and fragmentation effects directly depend on the available internal energy, that is a function of the mass stored in the tank and the thermodynamic properties. In light of the above, in order to calculate the flying distance of fragments, it is necessary to assess the energy released by the explosion. For this reason, the next two subsections provide a number of models available in the literature for assessing the mechanical energy (Subsection 2.3.1) and proposed methods for calculating the fragment ranges (see Section 2.3.2).

2.3.1 Mechanical Energy models

Several methods to estimate the energy released after an explosion are available in the literature. They can be categorized in ideal gas behaviour and real gas behaviour. It is important to point out that the models on the following pages have already been validated for common liquid fuels, such as propane and LPG (liquefied petroleoum gas).

Ideal gas behaviour models

The "Ideal gas behaviour" models (IGB) estimate the released energy from the tank volume, the pressure at the explosion, the atmospheric pressure, which is the pressure at the final equilibrium; the only fluid property they take into account is the specific heat ratio. When it comes to BLEVE, it is necessary to apply a correction, no longer considering only the volume of the tank but also the amount of flashing liquid (Equation 2.1). In Table 2.3 the selected models are presented, where:

- P is the pressure inside the tank at the moment of explosion $[Pa]$;
- P_0 is the atmospheric pressure $[Pa]$;
- γ is the specific heat ratio (e.g. 1.4 for hydrogen);
- V^* is the expanding volume of the fluid [m^3], it is the sum of the gaseous phase and the liquid flashing volumes. It is calculated as [29]:

$$V^* = V_{TANK} + m_L \left(\frac{f}{\rho_V} - \frac{1}{\rho_L} \right) \tag{2.1}$$

where f is the liquid flashing factor estimated by the following correlation:

$$f = 1 - exp\left\{-2.63\left[1-\left(\frac{T_c - T_0}{T_c - T_b}\right)^{0.38}\right]\frac{c_{p,L0}}{\Delta h_{v0}}\left(T_c - T_b\right)\right\} \tag{2.2}$$

and:

- T_c is the critical temperature [K];
- T_0 is the liquid phase temperature inside the vessel before the explosion [K];
- T_b is the liquid boiling temperature inside the vessel [K];
- $c_{p,L0}$ is the specific heat of the liquid at the boiling temperature $[\frac{J}{kg \cdot K}]$;
- $\Delta h_{v,0}$ is the latent heat of vaporisation at boling point $[\frac{J}{kg}]$.

Table 2.3: Equations of Ideal Gas Behaviour models.

Assumption	**Equation**	**Ref.**
Isochoric Process	$E_{Brode} = \frac{P - P_0}{\gamma - 1} \cdot V^* \quad (2.3)$	[30]
Isothermal process	$E_{IE} = P \cdot V^* \cdot ln\left(\frac{P}{P_0}\right) \quad (2.4)$	[31]
Thermodynamic availability	$E_{TA} = P \cdot V^* \cdot \left[ln\left(\frac{P}{P_0}\right) - \left(1 - \frac{P}{P_0}\right)\right] \quad (2.5)$	[32]
Adiabatic process	$E_{Prugh} = \frac{P \cdot V^*}{\gamma - 1} \cdot \left(1 - \frac{P_0}{P}\right) \quad (2.6)$	[29]

It is worth noting that when the temperature of the liquid before the explosion reaches the critical temperature, V^* is equal to the total tank volume.
The specific features of each model are well explained by *Ustolin et al.* in their comparative analysis [7], in which the models are described as follows: the equation 2.3 propoesd by Brode [30] estimates the total energy generated by the detonation of a spherical charge of TNT assuming it as an isochoric process. Smith and Van Ness [31] assumed an isothermal expansion process for their model (Equation 2.4). The model proposed by Crowl [32] calculates the maximum mechanical energy extractable from a

substance which reversibly reaches the equilibrium with the surrounding environment from the burst conditions (Equation 2.5). Finally, Prugh [29] proposed to consider the process as adiabatic and to replace the tank volume with the total volume of the expanding fluid in the equation 2.6 developed for high pressure container to liquefied gas vessels.

Real gas behaviour models

With respect to the previously illustrated IGB models, the "real gas behaviour" models (RGB) take into account several thermodynamic properties and variables to evaluate the released energy from an explosion. In Table 2.4 the selected models are presented, and the corresponding parameters and thermodynamic variables are illustrated in Table 2.5, where:

- $u_{v_{is}}$ is the specific internal energy of the vapour phase after the isoentropic expansion $[\frac{J}{kg}]$;
- $u_{l_{is}}$ is the specific internal energy of the liquid phase after the isoentropic expansion $[\frac{J}{kg}]$;
- x_v is the entropy ratio of the vapor phase;
- x_l is the entropy ratio of the liquid phase;
- X is the intersection point between the variation of the internal energy and the adiabatic irreversible expansion work;

To make it clearer, the indexes v, v_0, l, l_0 indicates the vapour and liquid phases before and after (at atmospheric pressure) the explosion.
Again, as with the IGB models, the peculiar characteristics of each model are well explained by Ustolin et al. [7].
The "TNO" model (Equation 2.7 assumes the process as isoentropic and takes into account the expansion of both the liquid and the vapour phase considering their masses (m_l and m_v in [kg]) and their internal energy (u_l and u_v in $[\frac{J}{kg}]$).
The "Planas" model consider the process as adiabatic and irreversible; it takes into account the mass of the tank m_T [kg] and the specific internal energy of the liquid and vapour phase under saturation conditions at atmospheric pressure (u_{l_0} and u_{v_0} in $[\frac{J}{kg}]$).
The "SE" (Superheating) model takes into account the enthalpy difference of the liquid phase before and after the explosion, not considering the vapour phase at all.
The "Genova" model assumes that the flashing liquid process is led by the excess heat stored in the vessel and only the liquid phase is taken into account to the mechanical energy estimation.

Table 2.4: Equations of Real Gas Behaviour models.

Labeled as	**Equation**	**Ref.**
TNO	$E_{TNO} = m_v\,(u_v - u_{v_{is}}) + m_l\,(u_l - u_{l_{is}}) \quad (2.7)$	[18]
Planas	$E_P = -\left[(u_{l_0} - u_{v_0})\, m_T X - m_T\, u_{l_0} + U_i\right] \quad (2.8)$	[33]
SE	$E_{SE} = k\, m_l\,(h_l - h_{l_0}) \quad (2.9)$	[34]
Genova	$E_{GE} = \Psi\, m_l\, c_{pl}\,(T_l - T_{l_0}) \quad (2.10)$	[35]
Birk	$E_{Birk} = m_v\,(u_v - u_{v_{is}}) \quad (2.11)$	[36]

Table 2.5: RGB: definition of parameters.

$$x_v = \frac{s_v - s_{l_0}}{s_{v_0} - s_{l_0}} \tag{2.12}$$

$$x_l = \frac{s_l - s_{l_0}}{s_{v_0} - s_{l_0}} \tag{2.13}$$

$$u_{v_{is}} = (1 - x_l)\, u_{l_0} + x_l\, u_{v_0} \tag{2.14}$$

$$u_{l_{is}} = (1 - x_v)\, u_{l_0} + x_v\, u_{v_0} \tag{2.15}$$

$$X = \frac{m_T\, P_a\, v_{l_0} - V_T\, P_a + m_T\, u_{l_0} - U_i}{\left[(u_{l_0} - u_{v_0}) - (v_{l_0} - v_{v_0})\, P_a\right] m_T} \tag{2.16}$$

The "Birk" model is quite similar to the one proposed by TNO, but it only takes into account the vapour phase.
For the sake of a more comprehensive discussion, it is relevant to point out that, once the energies released by the explosion have been calculated, it would be necessary to consider certain conversion factors (see Table 2.6) in order to estimate the overpressure of the generated blast wave. To be more specific, the "SE" and "Genova" models directly consider the fraction of the mechanical energy converted into the pressure wave generation (k and Ψ, respectively). The other models consider a coefficient to take into account the reflection of the blast wave on the ground; as it is evident in Table 2.6, the "Planas" model suggests two different coefficient: $\alpha = 0.4$ if the failure of the vessel is ductile, $\alpha = 0.8$ if the failure is fragile. As regards the IGB models, the conversion factor is always equal to 1.

Table 2.6: RGB models: energy conversion factors

Model	α	k	Ψ
TNO	2.0	-	-
Planas	0.4 - 0.8	-	-
SE	1.0	0.14	-
Genova	1.0	-	-
Birk	2.0	-	-

2.3.2 Horizontal range estimation

The energy released by an explosion is distributed as shown in the Figure 2.16. As it can be seen, a fraction of the energy is devoted to the generation and projection of the fragments. However, it is difficult to estimate what is the fraction of the mechanical energy (λ) that contributes to this type of consequence: as far as the BLEVE is concerned, several recommended values can be found in the literature:

- $\lambda = 0.04$ [18];
- $\lambda = 0.40$ [37].

Having clarified this, the first step in estimating the distance travelled by the fragments is to estimate the initial velocity. Therefore, considering that part of the energy is translated into kinetic energy (E_k), it is possible to estimate the initial velocity as follows:

$$v_i = \sqrt{\frac{2\ E_k}{M_v}} = \sqrt{\frac{2\ \lambda\ E_{av}}{M_v}} \tag{2.17}$$

where E_{av} is the released energy in $[\frac{J}{kg}]$, α is the fraction of energy responsible for the fragments and M_v is the total mass of the vessel in [kg]. Once the initial velocity has been defined, it should be pointed out that there are two different methods for estimating the flying distance: the first one considers air resistance to be zero and the second one consider the air resistance proportional to the square of the velocity.

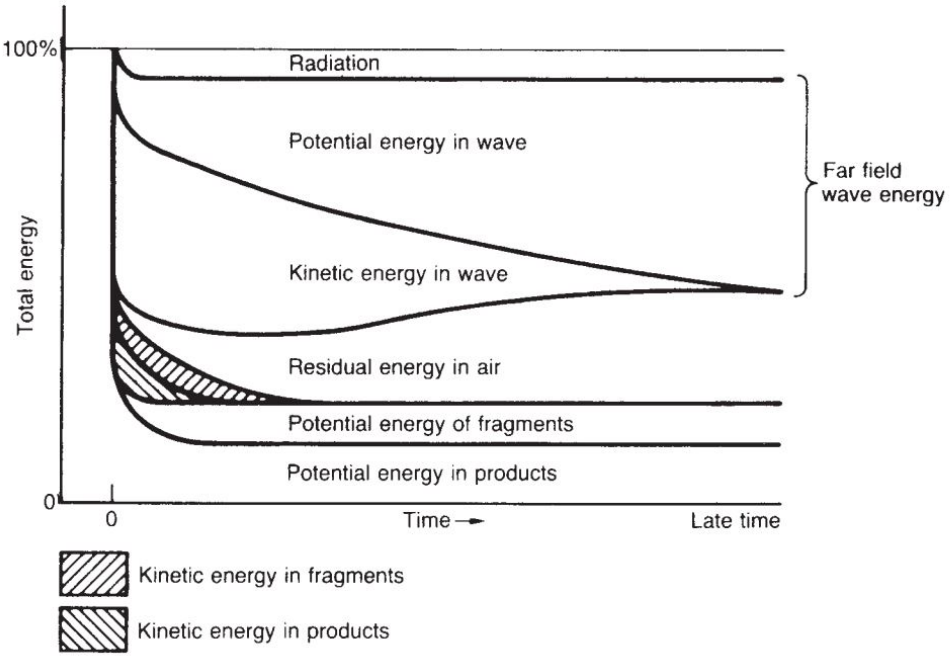

Figure 2.16: Schematic energy distribution in a chemical explosion [38].

Neglecting Fluid Dynamic Forces

This approach neglects the fluid dynamic forces since the fragment characteristics (mass, dimensions and shape) are usually difficut to set a priori. In this case the equations of motion are [38]:

$$\begin{cases} \frac{d^2x}{dt^2} = 0 \\ \frac{d^2y}{dt^2} + g = 0 \end{cases} \tag{2.18}$$

where g is the acceleration due to gravity, t is the time and x and y are the distances in the horizontal and vertical directions, respectively. From these it is possible to obtain the distance travelled:

$$R = \frac{v_i^2 sin\,(2\alpha)}{g} \tag{2.19}$$

According this method, it is clear from the Equation 2.19 that the only parameters affecting the flying distance are the initial velocity and the initial angle of fragments which is typically 5÷10° for cylindrical vessels horizontally placed and 45° if vertically placed [37].

Considering Fluid Dynamic Forces

This approach is base on the fact that after a fragment has acquired an initial velocity it is no longer accelerated by an explosion or pressure rupture, two forces act on the fragment during its flight. These are gravitational forces and fluid dynamic forces. Fluid dynamic forces are visually subdivided into drag and lift components. The effect of drag and lift will depend both on the shape of the fragment and its direction of motion with respect to the relative wind. This method considers a projectile subject to a resistance proportional to the square of the velocity; in this case the equations of motion are [38]:

$$\begin{cases} \frac{d^2x}{dt^2} + k\left(\frac{dx}{dt}\right)^2 = 0 \\ \frac{d^2y}{dt^2} + k\left(\frac{dy}{dt}\right)^2 + g = 0 \end{cases} \tag{2.20}$$

where k is a drag factor. Moreover the fluid dynamic force components of drag and lift at any instant can be expressed as:

$$\begin{cases} F_L = C_L A_L \frac{\rho u^2}{2} \\ F_D = C_D A_D \frac{\rho u^2}{2} \end{cases} \tag{2.21}$$

where A_D is the drag area, A_D is the lift area, C_D is the drag coefficient, C_L is the lift coefficient,F_D is the drag force, F_L is the lift force, u is the velocity of the fragment and ρ is the density of air. The range is obtained by solving the equations of motion for acceleration of the fragment in the horizontal and vertical directions, utilizing for the drag and lift forces Equations 2.21. In order to derive a graphical method it is possible to use the curves in the Figure 2.17, developed by performing a model analysis.
It should be noted that, in generating these curves, several initial trajectory angles were used in the analysis to obtain the maximum range for the respective fragments. This approach requires as input data the mass (M_F), the dimension and the shape of the fragments in order to calculate the dimensionless velocity:

$$\bar{v}_i = \frac{C_D\ A_D\ \rho_o v_i^2}{M_F\ g} \tag{2.22}$$

where ρ_o is the density of the air (1.229 m^3/kg [40]). After estimating this value, the graph (see Figure 2.17) is used to read off the corresponding dimensionless range $\bar{R}$, choosing the correct curve. Finally, it is possible to calculate the flying distance as:

$$R = \frac{\bar{R}\ M_F}{C_D\ A_D\ \rho_o} \tag{2.23}$$

To apply this method properly, it is necessary to evaluate the value for the lift-to-drag ratio $C_L\ A_L/C_D\ A_D$ and a value for $C_D A_D$ (m^2). The values recommended in the literature are given in Table 2.7.

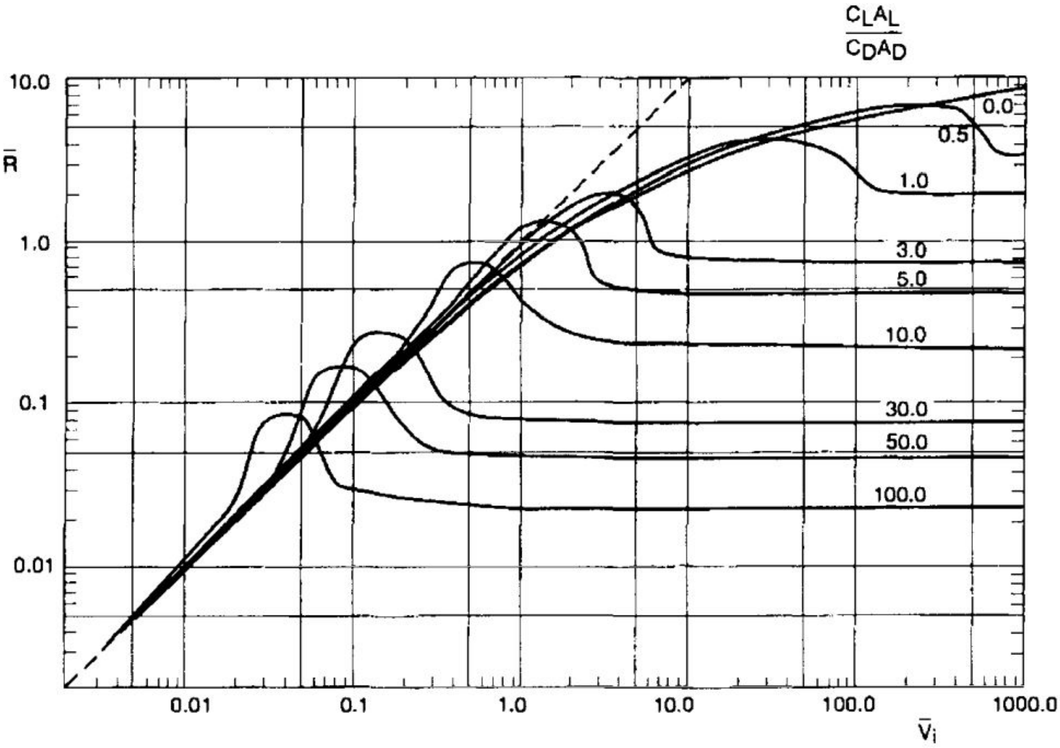

Figure 2.17: Scaled curves for fragments range projection [39].

Table 2.7: Drag and lift of fragments [18].

Shape	$\mathbf{C}_D\mathbf{A}_D$	$\mathbf{C}_L\ \mathbf{A}_L/\mathbf{C}_D\ \mathbf{A}_D$
Plate (tumbling)	0.595 x A_{plate}	0
Plate (no tumbling, face on)	1.17 x A_{plate}	0
Plate (no tumbling, edge on)	0.1 x A_{plate}	0 to 10
Hemisphere (tumbling)	0.615 x $\pi/4$ x d_v^2	0
Hemisphere (no tumbling)	0.47 x $\pi/4$ x d_v^2	0
Half a tank (rocketing)	0.47 x $\pi/4$ x d_v^2	0
Cylinder (edge on)	1.2 x d_v x L_v	0
Strips (tumbling)	0.99 x A_{strip}	0

Therefore it is evident that to apply this method it is necessary to assume the mass, the dimension and the shape of the fragments as well as the initial velocity (Equation 2.17).

3 SH2IFT project

SH_2IFT - *Safe Hydrogen Fuel Handling and Use for Efficient Implementation* project lasted from 2018 to the third quarter of 2022. One of the goals of this project is to cover up the lack of knowledge in LH_2 BLEVE accidents through some experiments whose purposes are to investigate the consequences of an atypical scenario. In the first part of this chapter those experiments are described. The second part focuses on one experiment and on the data collection used as input to modeling activity for the fragmentation range estimation.

3.1 Experimental description

Experiments have been perfomed to investigate the consequences of a storage tank containing liquefied hydrogen (LH2) engulfed by a fire. The goal was to induce a fired BLEVE (see Section 2.2.2). The tests were performed at the Test Site Technical Safety of the Bundesanstalt für Materialforschung und -prüfung (BAM) in Germany within a cooperation between BAM and Gexcon. The tanks to be tested are three double-walled vacuum insulated vessels of 1 m^3 volume with different orientation and different insulation material (Perlite or MLI), as it is shown in Figure 3.1 and 3.2.

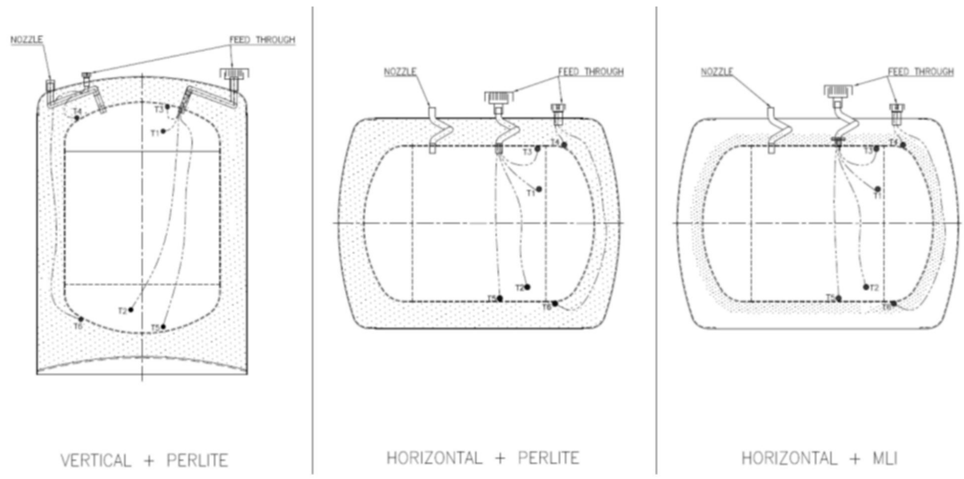

Figure 3.1: The layout of the LH2 storage vessels used during the SH_2IFT experiments [17].

Figure 3.2: The LH2 vessels before the tests.

In order to induce the tank explosion, heat was applied to the tanks by an array of propane burners located underneath the vessels and the safety valves were deactivated to force a pressure build-up. The results of each test are described below:

1. Horizontal + PERLITE: after approximately 50 minutes the outer vessel imploded partly; a leaking started through the seal of one of the valves on top of the vessel leading to a jet-fire.

2. Horizontal + MLI: after 1 hour the vessel failed to cause a fireball, blast waves and fragments.

3. Vertical + PERLITE: after a short period the vessel's outer shell imploded, as in the first experiment; after 4 hours the test had to be aborted because of the lack of propane to provide heat and no critical failure was detected.

3.2 Data Collection

In this section the focus is given to the successful experiment in terms of obtaining BLEVE, the final accident scenario to be analysed. At the beginning of that experiment the hydrogen mass inside the tank was 27 kg and the pressure was higher than the atmospheric pressure. As the tank was loaded with heat, the internal pressure increased; after 40 minutes the vessel started to leak through a blow-off line exiting far away from the area of the experiment, leading to a stop of the rise of the inner pressure which stayed constant at 50 bar (see Figure 3.3). After slightly longer than an hour the explosion occurred. The conditions inside the tank at the time of the explosion are not entirely clear: the total mass is uncertain due to the leak, as is the amount of liquid in the vessel and its temperature. The temperature of the vapour phase at the time of the explosion is about -180°C.

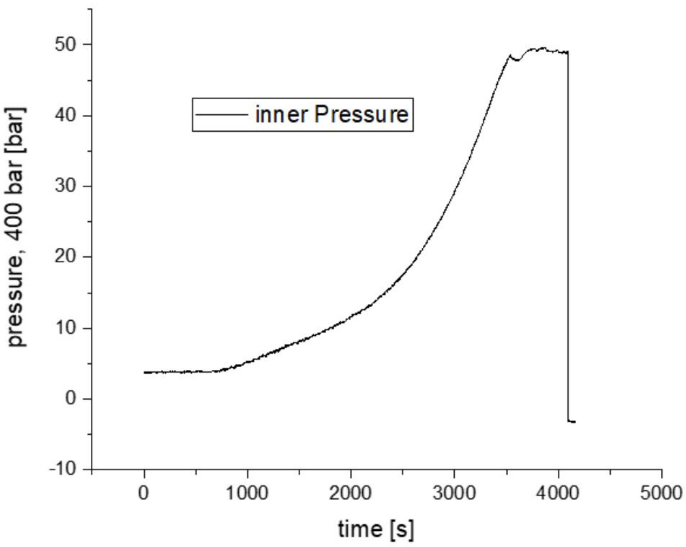

Figure 3.3: Pressure inside the inner vessel during the second BLEVE test of the SH_2IFT project.

3.2.1 Fragments

The total number of fragments catalogued is 53 and for each one the coordinates (x, y) and mass are listed in the table 6.1 in Annex A. These results show that the failure of the vessel resulted in generation of six main fragments. The outer vessel broke into 4 parts: two end caps (no. 38, 47) and two parts of the shell (no. 19, 48). One of the latter (no. 19) remained attached to the support. The inner vessel broke into 2 pieces: an end cap (no. 4) and the shell attached to the other end cap (no. 1).

3.2.2 Video of the explosion

In order to conduct a thorough analysis, videos of the explosions are available: four GoPros (60fps) were used to monitor the events, one on board of a drone and one for each direction around the vessel (Nord, South, East and West). Through the software *Kinovea* [41] the videos have been split into frames available in Annex B. The time between the frames is 17 ms: this information will be used for an estimation of the initial fragment velocity (see section 4.2.2).

3.2.3 Blast wave and Fireball

For the sake of completeness, the data concering other two effects of BLEVE are given below:

- Overpressure: it was measured by two blast pencils positioned at two different distances from the vessel. Figure 2.13 shows that a maximum pressure of 133 mbar and 99 mbar were detected at 22.5 m and 26.4 m from the tank, respectively.

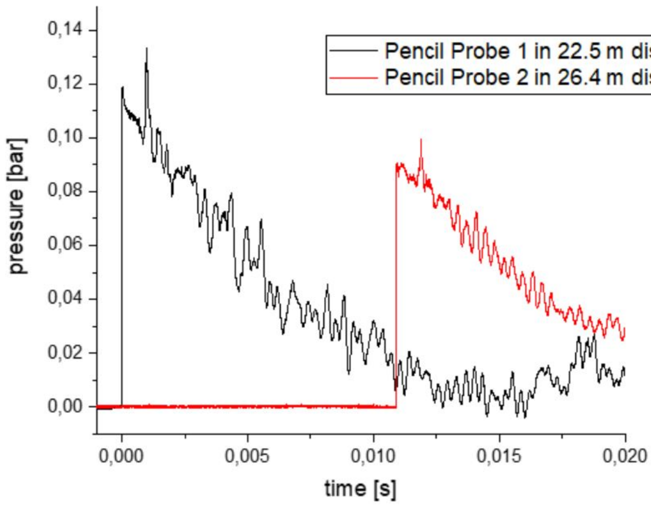

Figure 3.4: Blast waves measured at distances of 22.5 m and 26.4 m from the vessel [17].

- Fireball: the maximum diameter was about 20 m and the total duration was about 5 s, with lift-off occurring after 2 s. The heat radiations were measured by bolometers: maximum incident heat radiation levels of 2.1 kW/m2 at 70 m and 1.2 kW/m2 at 90 m. The bolometer at 50 m distance was in overload mode with incident heat radiation exceeding 2.4 kW/m^2. The measures are collected in Figure 3.6 and the fireball is shown in Figure 3.5.

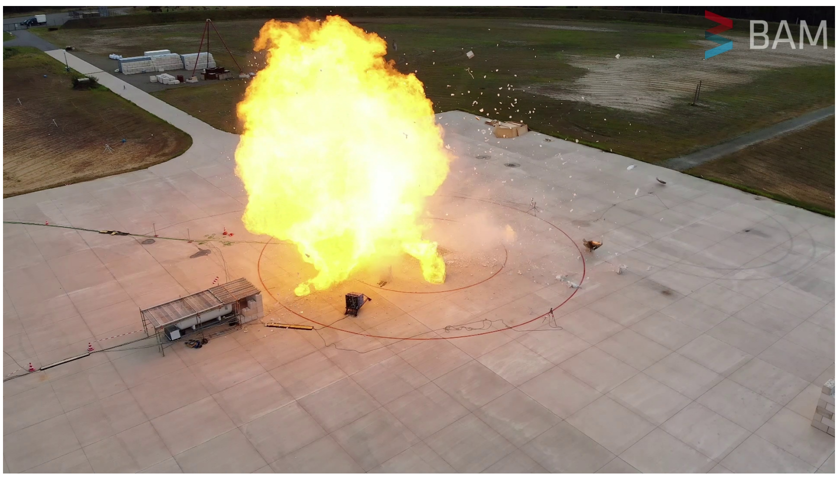

Figure 3.5: Fireball from the drone.

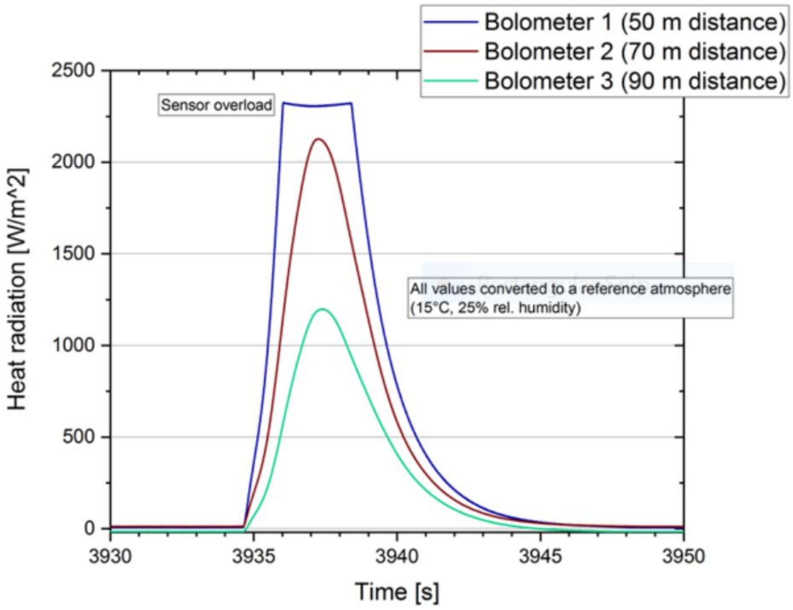

Figure 3.6: Incident heat radiation measured at distance of 50 m, 70 m and 90 m from the vessel [17].

4 Material and methods

This chapter is dedicated to the description of the implemented methodology to perform a consequence analysis of the SH_2IFT project BLEVE. The focus is on the study of fragments, while the effects of overpressure caused by the shock wave and fireball consequences are not discussed. The first section of this chapter introduces the method used to process and analyse data. In the second section, selected models for the analysis of fragment consequences are provided. The assumptions needed to carry out the modeling are presented together with the procedure.

4.1 Data processing

First of all, raw data from the experiment are processed: the coordinates of the tank are set at (0,0) and consequently all fragment coordinates are recalculated (x^*,y^*). Then the distance of the fragments from the original position of the tank is calculated. The coordinates of fragment number 4 (10,1) are reprocessed in order to avoid underestimation, since the video analysis shows that it crashes into the protective wall of the propane tank immediately after the explosion (see Figure 4.1). The actual distance value is estimated by adding the back and forth path from the tabulated distance to the propane tank (d_{F-T}), as follows:

$$d_4^* = d_{F-V} + 2d_{F-T} \tag{4.1}$$

The results of data compilation is used as a basis for comparison with the results of modelling, which is described in the following paragraphs.

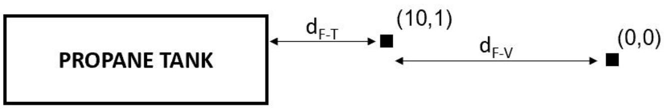

Figure 4.1: Scheme for reprocessing data: d_{F-T} is the distance between fragment and propane tank; d_{F-V} is the distance between fragment and LH2 vessel.

4.1.1 Fragment classification

Checking the fragmentation pattern and the fragment shape is necessary to determine whether they are consistent with those resulting from same types of explosions of tanks containing conventional fuels. To this end, the classification of fragmentation pattern, shown in Figure 4.2 and proposed by Gubinelli et al. [42], is used: for BLEVE explosion with conventional fuels the most commons are CV2 and CV7 [42].

ID	Fragmentation pattern	Expected fragment reference shapes	Number of fragments
CV1	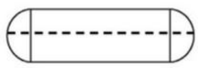	Axial fracture starts and propagates in two opposite directions: the equipment may not be deformed (cylinder fragment) or may be flattened (plate fragment).	1
CV2		The fracture starts in the axial direction, and it may propagate in the circumferential direction generating two tube-ends. An alternative is the generation of a plate if the axial crack propagates on the tube-ends and stops.	2
CV3		Similar to CV2, but one tube-end is separated in 2 fragments.	3
CV4		Similar to CV2, but one tube-end is separated in 3 fragments, one of which is generally flatted.	4
CV7	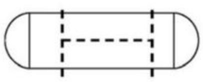	An axial crack may propagate in circumferential direction: the result is the generation of two tube-ends and a flattened shell.	3
CV11	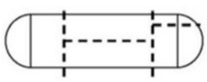	Similar to CV7, but one tube-end is separated in 2 fragments.	4
CV21	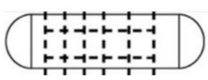	Similar to CV7, but the shell is separated in more than one fragment.	>5

Figure 4.2: Expected fragment reference shapes and expected number of fragments for credible vessel fragmentation patterns, [42].

4.1.2 Fragment distribution

Fragments projection is the BLEVE consequence which affects the largest area from the centre of the explosions [43]. This is why it is important to predict this value; however, the distribution of fragments in the horizontal plane is also very crucial. According to literature, it is evident that not all directions are equally probable following the explosive failure of the tank [44]. Taking into account industrial accidents reported by Holden [45], a preferential direction of projection is observed within a zone having 30° of angle aperture from a longitudinal (or principal) vessel axis (see Figure 4.3).

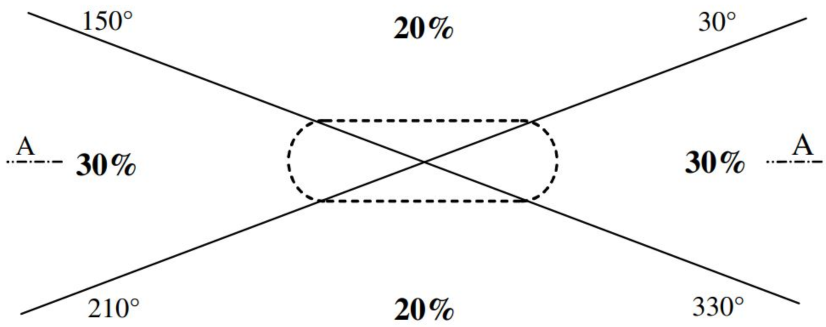

Figure 4.3: Fragment distribution for cylindrical vessel explosion [46].

For this reason, a similar graph must also be produced when processing this experiment, to investigate whether the specific features of a double tank and the peculiarities of hydrogen might lead to different results.

4.2 Modeling

The purpose of this section is to estimate the horizontal range and distribution of the fragments. To achieve this goal, the models presented in Section 2.3 are used: as a first step it is necessary to evaluate the mechanical energy released from the explosion; then it is possible to proceed to the analysis of the fragments. The modeling activity requires hydrogen physical and chemical properties as input data: the Cool-Prop package is used to this purpose [47].
A flow diagram (see figure 4.4) is provided to make the comprehension of the modeling phase clearer. Each block in the diagram is explained and discussed in the following pages.

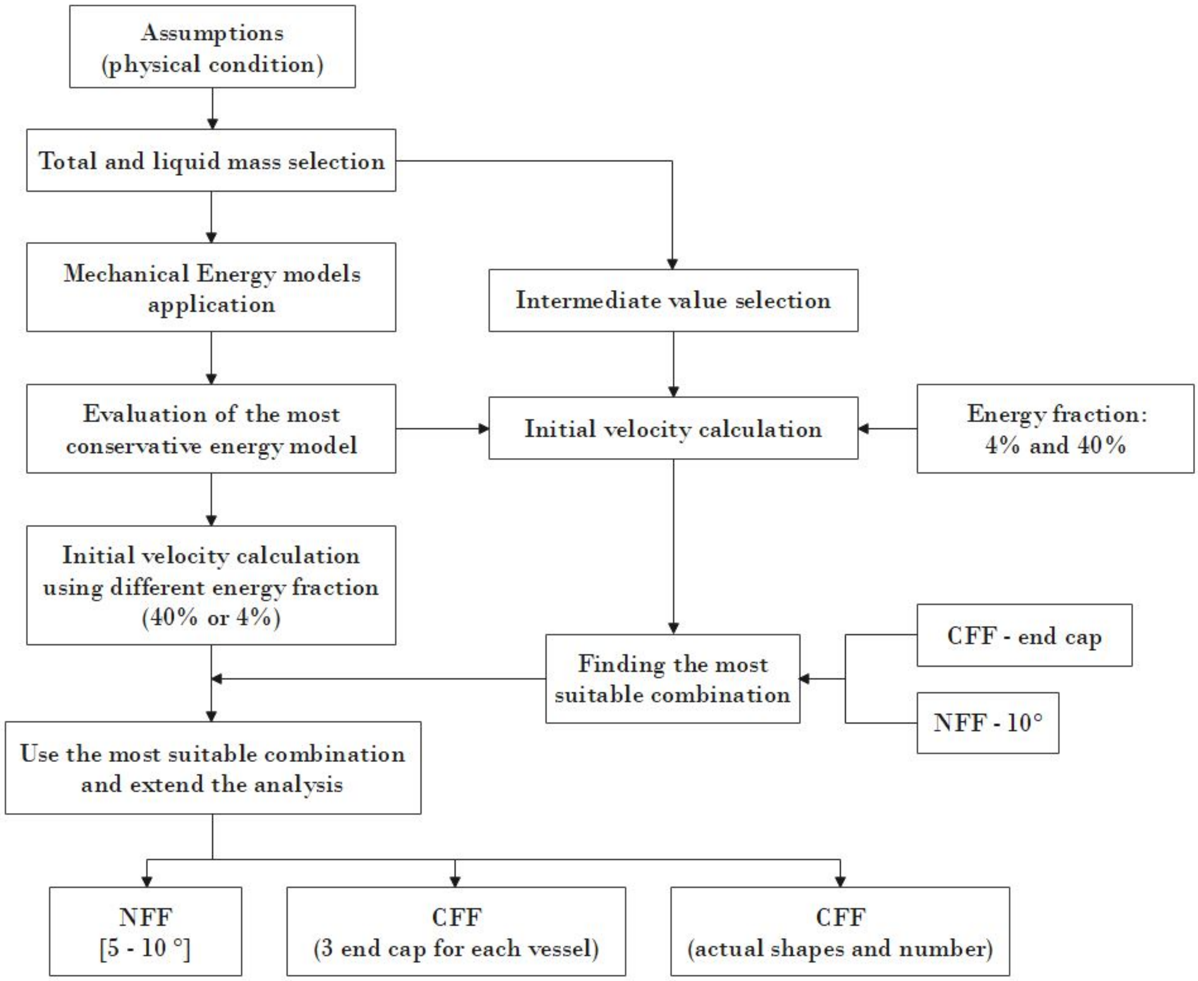

Figure 4.4: Procedure developed in this thesis to carry out the fragment analysis for LH2 tank explosions.

4.2.1 Assumptions

The aforementioned models require the knowledge of vapour and liquid phase conditions. As mentioned in Section 3.2, a leak occurred during the experiment: therefore the exact value of hydrogen mass in the vessel at the time of the explosion is unknown. In equation 4.2, the lower limit of this value is estimated assuming that the vapour phase is the only one present and its temperature and pressure are assumed to be respectively equal to -180°C and 50 bar, as mentioned in Section 3.2.

$$m_{H2_{LIMIT}} = \rho_v\,(-180\,°C,\,50\,bar)\cdot V_{TANK} \tag{4.2}$$

Five different values of hydrogen mass are considered in order to carry out the analysis:

$$m_{H2} = [m_{H2_{LIMIT}}, m_{H2_{INITIAL}}] \tag{4.3}$$

where $m_{H2_{INITIAL}}$ is the initial mass of hydrogen (equal to 27 kg), as mentioned in Section 3.2. The exact condition of the substance before the explosion is not clear: the experimental data show a certain fraction of the liquid phase to be still present. The maximum temperature of this phase is the critical point (T_c=32.8 K). In the analysis, since the temperature and mass of the liquid phase are unknown but crucial in the modeling, they are considered as independent variables: only the maximum value is taken into account for the temperature; the mass of the liquid phase is considered to range between a value of zero kg and the value corresponding to the situation before starting the propane burners at 9.5 bar. This latter value needs the following iterative process to be evaluated:

i. A "first try" liquid mass is set:

$$liquid\,mass = M_l^{ft}\ [kg] \tag{4.4}$$

ii. Considering the vapour phase as saturated vapour at 9.5 bar, the temperature of both phases is determined and consequently also the densities (ρ_l and ρ_v); therefore the liquid mass volume is calculated:

$$liquid\,volume = V_l^{ft} = \frac{M_l^{ft}}{\rho_l}\ [m^3] \tag{4.5}$$

iii. Through the known total volume of the vessel, it is possible to determine the volume of the vapour phase by subtraction:

$$vapour\,volume = V_v^{ft} = V_{TANK} - V_l^{ft}\ [m^3] \tag{4.6}$$

iv. Using the calculated density of the vapour phase, the "first try" mass of the vapour is evaluated:

$$vapour\,mass = M_v^{ft} = V_v^{ft} \cdot \rho_v\ [kg] \tag{4.7}$$

v. A "second try" liquid mass is evaluated by subtraction, using the total mass of hydrogen:

$$liquid\,mass = M_l^{st} = M_T - M_v^{ft}\ [kg] \tag{4.8}$$

vi. The "first try" liquid mass is updated with the "second try" value.

The iterative process continues until the difference between the values of M_l^{ft} and M_l^{st} is under 0.01%:

$$err = |M_l^{st} - M_l^{ft}| < 10^{-4} \tag{4.9}$$

These calculations are performed for each value of hydrogen mass in the equation 4.3. Each value of total hydrogen mass has the corresponding maximum value of liquid mass: this means that the analysis is carried out for five different values of total mass (13.3 kg, 16.5 kg, 20 kg, 23.5 kg, 27 kg) and ten values of liquid mass, as it is shown in table 4.1.

Table 4.1: Mass selection for the analysis.

	Varying hydrogen total mass				
Varying liquid mass	$m_{1,1}$	$m_{1,2}$	$m_{1,3}$	$m_{1,4}$	$m_{1,5}$
	$m_{2,1}$	$m_{2,2}$	$m_{2,3}$	$m_{2,4}$	$m_{2,5}$
	$m_{3,1}$	$m_{3,2}$	$m_{3,3}$	$m_{3,4}$	$m_{3,5}$
	$m_{4,1}$	$m_{4,2}$	$m_{4,3}$	$m_{4,4}$	$m_{4,5}$
	$m_{5,1}$	$m_{5,2}$	$m_{5,3}$	$m_{5,4}$	$m_{5,5}$
	$m_{6,1}$	$m_{6,2}$	$m_{6,3}$	$m_{6,4}$	$m_{6,5}$
	$m_{7,1}$	$m_{7,2}$	$m_{7,3}$	$m_{7,4}$	$m_{7,5}$
	$m_{8,1}$	$m_{8,2}$	$m_{8,3}$	$m_{8,4}$	$m_{8,5}$
	$m_{9,1}$	$m_{9,2}$	$m_{9,3}$	$m_{9,4}$	$m_{9,5}$
	$m_{10,1}$	$m_{10,2}$	$m_{10,3}$	$m_{10,4}$	$m_{10,5}$

4.2.2 Procedure

Once the physical condition of the substance in the tank at the time of the explosion is clarified for each value of table 4.1, the released energy is calculated using the methods in the section 2.3.1. The most conservative ones are chosen to go further in the analysis: one considering hydrogen as an ideal gas and one considering it as a real gas. The next step is selecting the fraction of mechanical energy and then applying the equation 2.17 to calculate the initial velocity of the fragment. Once this value has been obtained, the models for calculating the horizontal range can be applied, as described in section 2.3.2. A first trial is carried out with an intermediate value of total mass and the corresponding maximum amount of liquid ($m_{10,3}$) to figure out which combination should be excluded, as there are many. In this first trial an angle of 10° is considered with the "neglecting fluid dynamic forces method" (NFF) and an end cap shape is considered with the "considering fluid dynamic method" (CFF).

Once the most adapt combinations are selected, the analysis can be performed thoroughly. When the NFF method is used, the initial angle is a relevant input: to get more comprehensive results a range [5 - 10°] is taken into account for the reason explained in section 2.3.2.

It is important to underline that the initial velocity evaluation is not affected by the number of fragments generated the failure, but when applying the CFF method it becomes an important input. In this respect, the procedure is divided into two stages:

- Firstly, an approximation is made on the mass of the tank: the inner and outer parts have the same mass (365 kg). According to the most common fragmentation pattern (CV7), the CFF model is applied considering three fragments for each vessel, thus resulting in six fragments of the same mass ($\approx$ 122 kg). As it is only the first approach to modeling, the generated fragments are considered as end cap, which gives the most conservative results.

- Secondly, the method is applied to the actual case study; the fracture is considered in the six main fragments (see section 3.2.1) and the exact shape of each of them is taken into account for the estimation of the drag coefficient (see table 2.7). The equations to be adopted are 'Hemisphere (tumbling)' for fragment no. 1, 4, 38 and 47 and 'Strips (tumbling)' for fragment no. 19 and 48; some data are required in order to apply these equations:

Table 4.2: Data input to calculate drag coefficient.

Outer diameter	1.150 m
Inner diameter	0.750 m
A_{strip}	to be discussed

The exact dimensions of fragments 19 and 47 are unknown. The two fragments are schematised as plates, as it is shown in figure 4.5 and then the dimensions are evaluated as follows.

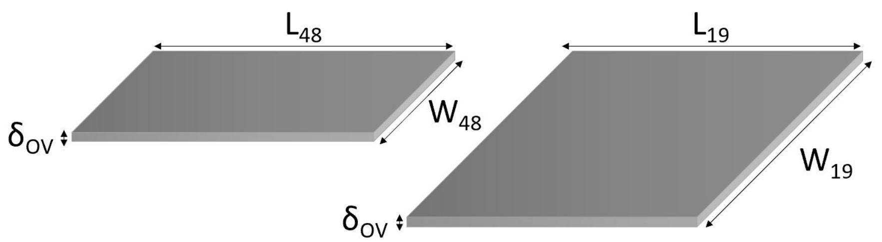

Figure 4.5: Sketch of fragments no. 48 (left) and no.19 (right).

i. The lengths of the two fragments (L_{19} and L_{48} in figure 4.5) are estimated to be about 2 m, against a total length of the outer vessel of 2.2 m.

ii. The thickness of the outer vessel (δ_{OV} in figure 4.5) is 4 mm and the density (ρ_{OV} in figure 4.5) is 7840 kg/m^3.

iii. The depth of the fragment no. 48 is calculated:

$$W_{48} = \frac{A_{48}}{L_F} = \frac{V_{48}}{\delta_{OV} \cdot L_F} = \frac{m_{48}}{\rho_{OV} \cdot \delta_{OV} \cdot L_F} \tag{4.10}$$

iv. The depth of the fragment no.19 is now calculated by subtraction between the circumference of the outer vessel and the depth calculated in (iii):

$$W_{19} = \pi \cdot D_{TANK} - W_{48} \tag{4.11}$$

v. Finally, the two areas are calculated:

$$A_{strip_{19,48}} = W_{19,48} \cdot L_{19,48} \tag{4.12}$$

A final approximation is made in this procedure: the shape of fragment no. 1 is considered to be an end cap, although the shell is still attached to it.

Drag Factor

The importance of estimating the drag coefficient is a crucial point when using the CFF method, as it has been previously pointed out. For this reason, an alternative to the table 2.7 is provided [48]:

- For fragment considered as plates (no. 19 and no. 47) it is possible to use this equation:

$$C_D A_{Dplate} = \frac{C_{DD} + C_{DC} \cdot \frac{\delta_{OV} \cdot min(W,L)}{W \cdot L}}{2 \cdot \delta_{OV} \cdot \rho_{OV}} \cdot M_F \tag{4.13}$$

  where C_{DC} is equal to 2.05 and C_{DD} is equal to 1.17.
  Fragment no. 19 requires particular attention: in this case, the shell plate is attached to the support, creating a complex geometry to consider in terms of drag coefficient. It is therefore considered as a thicker plate:

$$\delta_{19} = \frac{m_{19}}{\rho_{IV} \cdot A_{19}} \tag{4.14}$$

- For fragment considered as tube ends (no. 1, 4, 37 and 48) it is possible to use this equation:

$$C_D A_{Dtube\,end} = \frac{1}{4 \cdot \rho_{OV-IV} \cdot \delta_{OV,IV}} \left[\frac{3 \cdot C_{DA} \cdot R_{OV,IV} \cdot \pi + 4 \cdot C_{DB} \cdot l}{2 \cdot \pi \cdot R_{OV,IV} + 2 \cdot \pi \cdot l} \right] \cdot M_F \tag{4.15}$$

  where R is the radius of the outer or inner vessel and l is the length of the fragment.
  C_{DA} is equal to 0.47 and C_{DB} is equal to 1.2.

The table 4.3 synthesizes all the parameters required to calculate the drag coefficient for each fragment.

Table 4.3: Parameters to calculate the drag coefficient.

Fragment no.	**Parameters**
1	$R_{IV} = 0.375$ m $l = 1.5$ m $M_F = 124\,kg$ $\rho_{IV} = 7900$ kg/m^3 $\delta_{IV} = 3{\cdot}10^{-3}\,m$
4	$R_{IV} = 0.375\,m$ $l = 0$ m $M_F = 62\,kg$ $\rho_{IV} = 7900$ kg/m^3 $\delta_{IV} = 3{\cdot}10^{-3}\,m$
19	$W = 2.5$ m $L = 2$ m $M_F = 271\,kg$ $\rho_{OV} = 7840$ kg/m^3 $\delta_{19} = 6{\cdot}10^{-3}\,m$
38	$R_{OV} = 0.575\,m$ $l = 0$ m $M_F = 72\,kg$ $\rho_{OV} = 7840$ kg/m^3 $\delta_{OV} = 4{\cdot}10^{-3}\,m$
47	$R_{OV} = 0.575\,m$ $l = 0$ m $M_F = 76\,kg$ $\rho_{OV} = 7840$ kg/m^3 $\delta_{OV} = 4{\cdot}10^{-3}\,m$
48	$W = 1$ m $L = 2$ m $\rho_{OV} = 7840$ kg/m^3 $\delta_{OV} = 4{\cdot}10^{-3}\,m$

Initial velocity

Another critical aspect for the application of the models (see section 2.3) is the estimation of the initial velocity:

$$v_i = \sqrt{\frac{2\,E_k}{M_v}} = \sqrt{\frac{2\,E_{k_F}}{M_F}} = \sqrt{\frac{2\,E_k \frac{M_F}{M_v}}{M_F}} \tag{4.16}$$

As the previous equation shows, using the equation 2.17 means considering that mechanical energy is distributed according to the mass.
This assumption leads to uncertainty in the results. For this reason two alternative proceedings are proposed:

- Starting from the values of initial velocity calculated as described in the section 4.2.2, a new range is set: [40 - 120 m/s]. These values are used with both the NFF and CFF methods. The first one is coupled to a range of initial angle: [0 - 20 °]; the second one is applied to each of the six main fragments.

- Observation of videos of the explosion shows that not all fragments fly at the same initial velocity. In order to carry out a more representative analysis, an attempt is made to backtrack the initial velocity of the fragments from the video frames through the software *Kinovea*:

$$v_{exp} = \frac{\sqrt{x_1^2 + x_2^2}}{n \cdot \Delta t} \tag{4.17}$$

  where x_1 and x_2 are the distances observed from two different cardinal directions, Δt is the frame rate of the camera and n is the frame at which those distances are detected. Because of the fireball, visibility is limited and it is not possible to conduct this calculation for all fragments.

Table 4.4: Calculation of initial velocity from video analysis.

Fragment no.	**Coordinates**	**n**
38	$x_{South} = 8\,\mathrm{m}$ $x_{East} = 0.5\,\mathrm{m}$	7
47	$x_{South} = 4\,\mathrm{m}$ $x_{West} = 0.5\,\mathrm{m}$	4
48	$x_{South} = 0.5\,\mathrm{m}$ $x_{West} = 2\,\mathrm{m}$	1

The frames used to obtain the coordinates in table 4.4 are displayed in Annex B.

5 Results and discussion

This chapter focuses on the analysis of the experimental data of the SH_2IFT project. Hence, the emphasis is on presenting the results obtained by modeling as described in the previous chapter. After processing the experimental data and developing the assumptions, the results are proposed following the procedure outlined in the section 4.2.2. The whole analysis is carried out with the purpose to find the most suitable combination of methods to predict the BLEVE consequences concerning the fragment generation.

5.1 Data analysis

This section is dedicated to the analysis of the horizontal fragment distribution from the explosion of the double-walled vessel containing liquid hydrogen. Table 5.1 provides the coordinates with reference to the initial position of the tank, the center of which is located at (0,0), and its longitudinal axis lies along the x-axis.

Table 5.1: Fragment experimental data.

No. of fragment	**m [kg]**	**x**	**y**	**d [m]**
vessel	730	0	0	-
1	**124**	**1**	**7**	**7**
2	1	3	4	5
3	2	3	3	4
4	**61**	**10**	**1**	**10**
5	1	18	-22	29
6	4	21	-26	34
7	<1	19	-36	41

No. of fragment	**m [kg]**	**x**	**y**	**d [m]**
8	<1	-18	-27	33
9	<1	-16	-21	26
10	13	-17	-11	20
11	<1	-17	-7	18
12	<1	-24	-8	25
13	1	-30	-11	32
14	<1	-17	4	17
15	<1	-6	2	6
16	<1	-13	10	16
17	<1	-19	9	21
18	<1	-26	13	29
19	**261**	**-27**	**14**	**30**
20	<1	-26	28	39
21	<1	-27	29	40
22	1	-12	30	32
23	1	-11	30	32
24	<1	-10	32	33
25	<1	-10	33	34
26	<1	-7	34	35
27	<1	-7	19	20
28	2	-2	28	28
29	<1	-1	28	28
30	<1	1	28	28
31	2	4	28	28

No. of fragment	**m [kg]**	**x**	**y**	**d [m]**
32	<1	-2	36	36
33	<1	-2	37	37
34	<1	8	33	34
35	<1	8	21	22
36	1	11	12	16
37	1	11	12	16
38	**72**	**150**	**73**	**167**
39	2	-4	75	75
40	<1	-9	147	148
41	2	-83	106	135
42	1	-81	105	133
43	5	-33	63	71
44	1	-16	56	58
45	2	-13	48	50
46	1	-71	62	94
47	**76**	**-65**	**-11**	**66**
48	**65**	**-57**	**-109**	**123**
49	<1	4	-56	56
50	1	13	-68	69
51	1	34	22	40
52	2	38	-68	78
53	2	41	-68	79

As pointed out in previous chapters, there are six main fragments: four from the outer vessel and two from the inner vessel. The remaining fragments are smaller pieces of the tank or instrumentation. The observed fragment shapes were almost identical to those expected from the figure 4.2. In particular, the inner vessel is associated with CV2: one tube end flew off by itself, while the other remained attached to the cylindrical part of the tank that opened longitudinally. The outer vessel can be associated with CV7, although it is not exactly the same: two tube-ends are generated but the shell broke into two parts. This difference is probably due to the part of the vessel facing the floor that was attached to a support, which held it slightly causing a fracture that was not entirely expected. Apart from the difference given by the outer tank, it is evident that the peculiarity of being a double-walled vessel does not affect the fragmentation patterns, which are the same as those expected from a BLEVE derived from traditional substances (see section 4.1.1).

5.1.1 Fragment distribution

Figure 5.1 shows the distribution in the blast area: the size of the bubbles is related to the mass of the fragment, which is labeled in red.

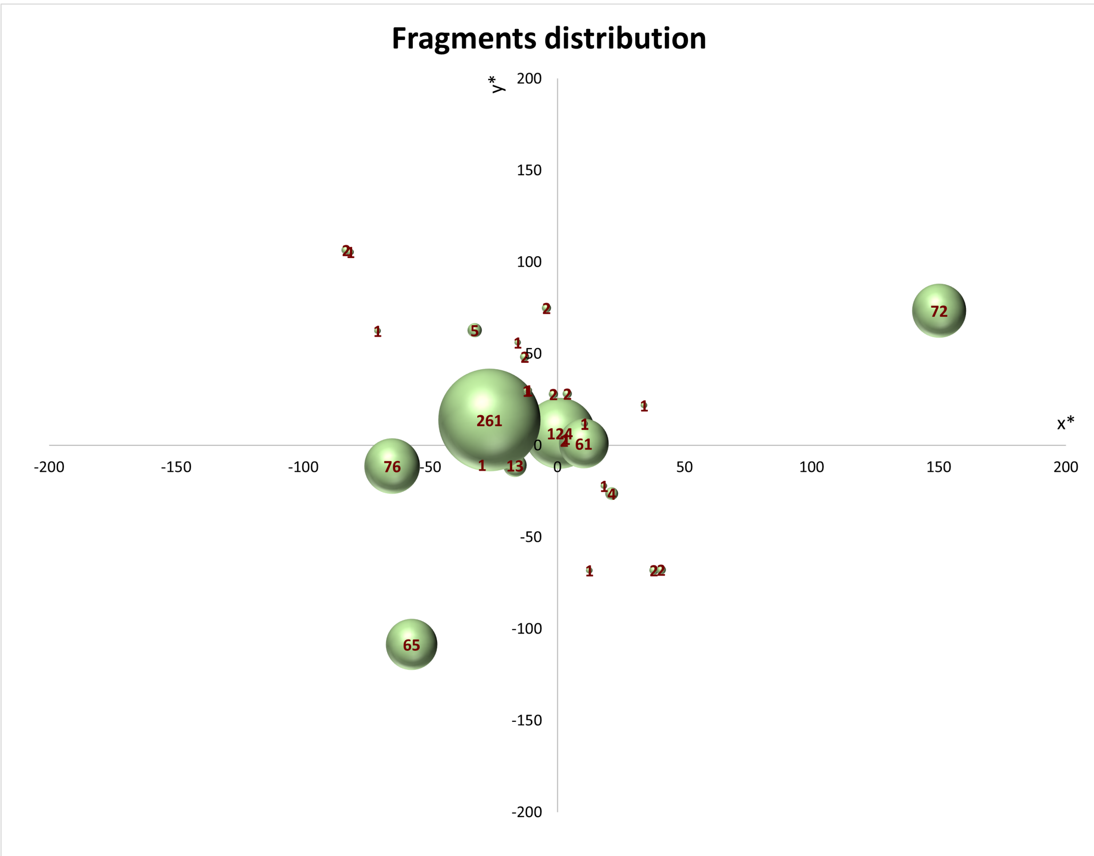

Figure 5.1: Fragment distribution. Red labels correspond to the mass of each fragment.

The same graph is provided by filtering by fragment weight: figure 5.2 shows only the six largest fragments; figure 5.3 shows fragments with a mass up to 15 kg; figure 5.4 shows fragments of negligible mass.

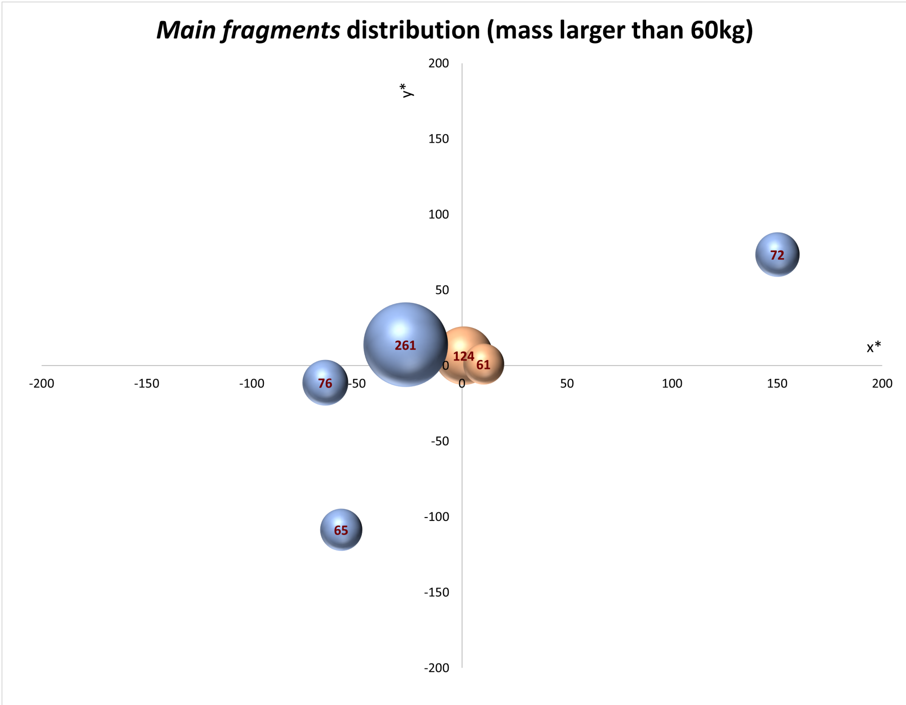

Figure 5.2: Fragment distribution of big fragments (m>60 kg). Red labels correspond to the mass of each fragment. Blue bubbles are fragments of the outer vessel and orange bubbles are fragments of the inner vessel.

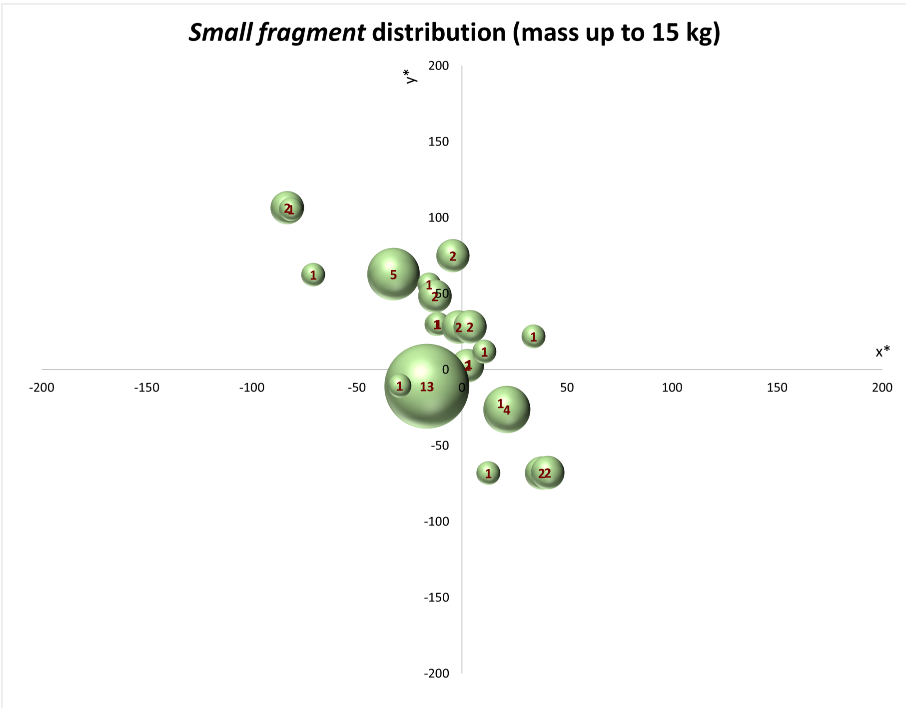

Figure 5.3: Fragment distribution of small fragments 15 kg. Red labels correspond to the mass of each fragment.

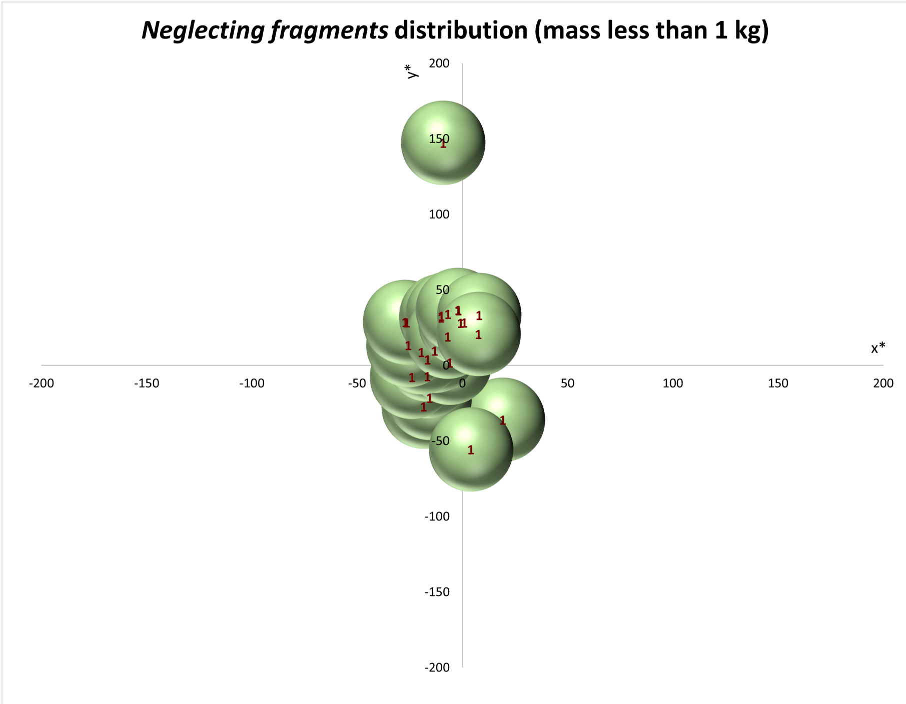

Figure 5.4: Fragment distribution of negligible fragments. Red labels correspond to the mass of each fragment.

It is evident from the figures above (figures 5.2, 5.3 and 5.4) that the main fragments have a preferential direction of projection along the longitudinal axis of the vessel, while the smaller fragments have a more random distribution. Indeed, those with negligible mass (mass less than 1 kg) show a preference for the other direction.
To compare the results of the SH_2IFT experiment with those predicted in the literature, the percentage distribution is evaluated by proposing the following graphs (figures 5.5, 5.6 and 5.7). The area surrounding the tank is divided into 8 zones: 330-30°, 30-60°, 60-120°, 120-150°, 150-210°, 210-240°, 240-300° and 300-330°.
Figure 5.5 shows the distribution without differentiating between fragments, which means that the largest has the same impact as the smallest in the calculation. Different numbers are shown in the image: the gray ones are calculated directly from the experimental data, and the black ones are suggested to provide a symmetrical distribution.
Figure 5.6 shows how the mass is distributed in the different zones, considering the ratio of the mass in each area to the total mass of the vessel ($\frac{\sum M_F}{M_v}$).
Figure 5.7 illustrates the percentage breakdown when only the main components are taken into account. Comparing figures 5.7 and 4.3 shows that the results are consistent with the literature.

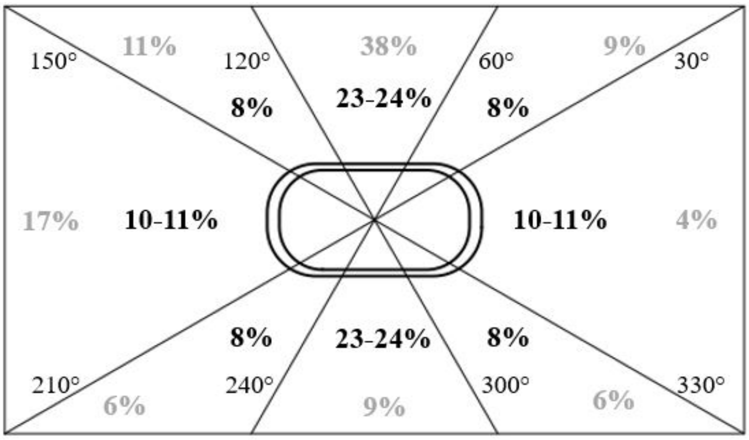

Figure 5.5: Numerical distribution of fragments: observed distribution in grey and proposed distribution in black.

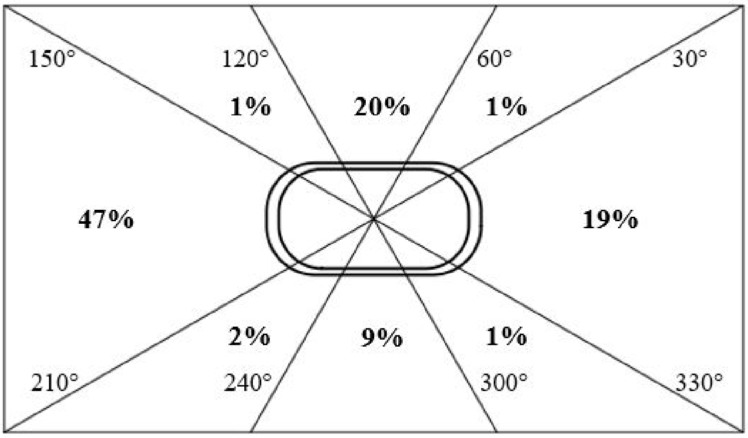

Figure 5.6: Mass distribution of fragments.

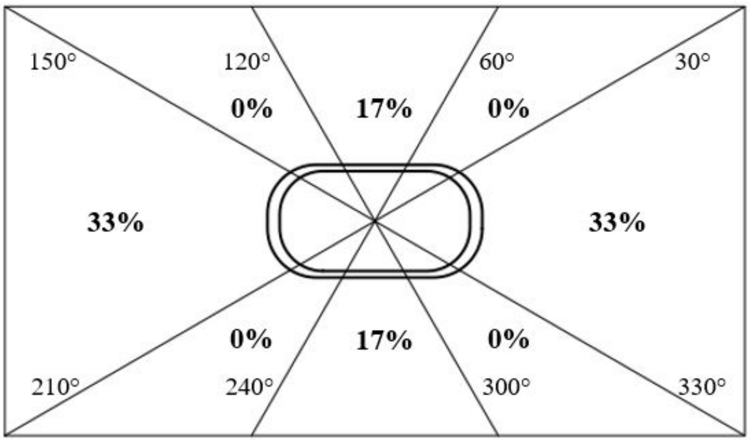

Figure 5.7: Observed and proposed fragment distribution taking into consideration main fragments (m>60 kg).

Before proceeding with the modeling phase, it is necessary to apply the modification explained in section 4.1 about fragment no. 4: taking into account that it ran into the protective wall for the propane tank, the estimated distance (d_4^*) is 23 m. It is worth noting that the considerations stated in the previous pages are not affected by this adjustment.

5.2 Mechanical energy estimation

The first step in applying models that predict the distance traveled by fragments after an explosion is to estimate the mechanical energy. Before the models in section 2.3.1 can be applied, the initial conditions must be clarified. The lower limit for the mass in the tank at 50 bar pressure ($m_{H2_{LIMIT}}$) is estimated to be 13.3 kg. By applying the procedure described by equations 4.4 - 4.8, it is possible to calculate the maximum initial liquid content corresponding to each value of total mass considered. At this point, table 4.1 can be updated with the values investigated, as shown in table 5.2.

Table 5.2: Liquid mass values considered in the modeling.

$\mathbf{m_{H2}}$**[kg]**	13.3	16.5	20.0	23.5	27.0
$\mathbf{m_{LIQ}}$**[kg]**	0	0	0	0	0
	0	0.50	1.02	1.54	2.07
	0	1.00	2.04	3.09	4.13
	0	1.49	3.06	4.63	6.20
	0	1.99	4.08	6.17	8.26
	0	2.49	5.10	7.72	10.33
	0	2.99	6.12	9.26	12.40
	0	3.48	7.14	10.80	14.46
	0	3.98	8.16	12.35	16.53
	0	4.48	9.19	13.89	18.60

The mechanical energy of the explosion is calculated, as mentioned above, through several physical models. The following charts (see figures 5.8 and 5.9) show the mechanical energy estimation in function of the mass of the liquid at the time of the explosion; in the first part of the analysis only the initial total mass is considered (27 kg). The ideal gas model chosen as a result of the comparison is the isothermal expansion (IE), because it is the most conservative as it is evident from figure 5.8. The real gas model chosen as a result of the comparison is the TNO, since it is the most conservative as it is clear from figure 5.9. It is imperative to point out that IGB models tend to be more conservative with respect to the RGB ones.

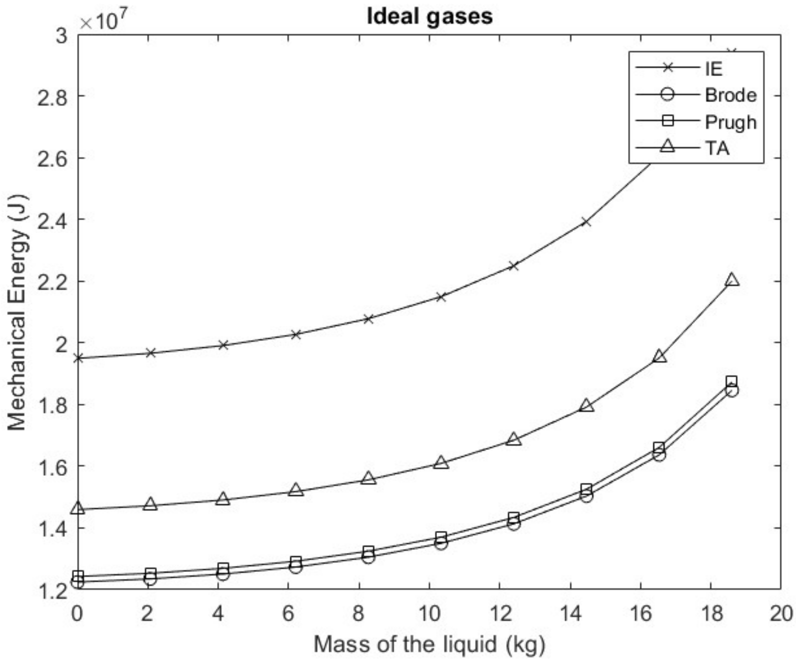

Figure 5.8: Mechanical energy: ideal gas behavior

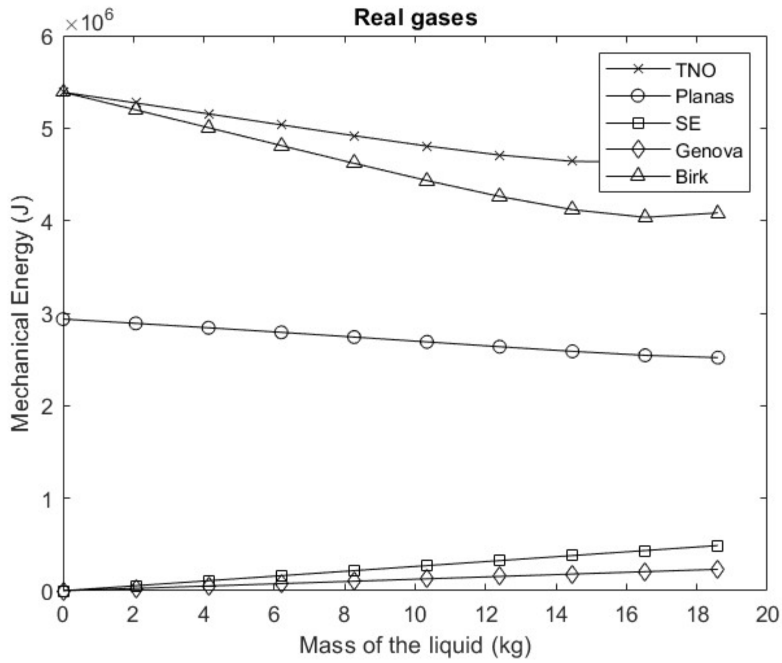

Figure 5.9: Mechanical energy: real gas behavior

At this point, it is possible to extend the analysis and estimate the mechanical energy varying the total mass of hydrogen, thus taking into account the leak during the experiments, which does not allow the exact value to be deductible. Figure 5.10 shows the dependency of the mechanical energy from the total LH2 mass and the fraction of liquid. The results given by the IGB and RGB models are very different, both in terms of order of magnitude and trend. For this reason, figure 5.11 is provided.

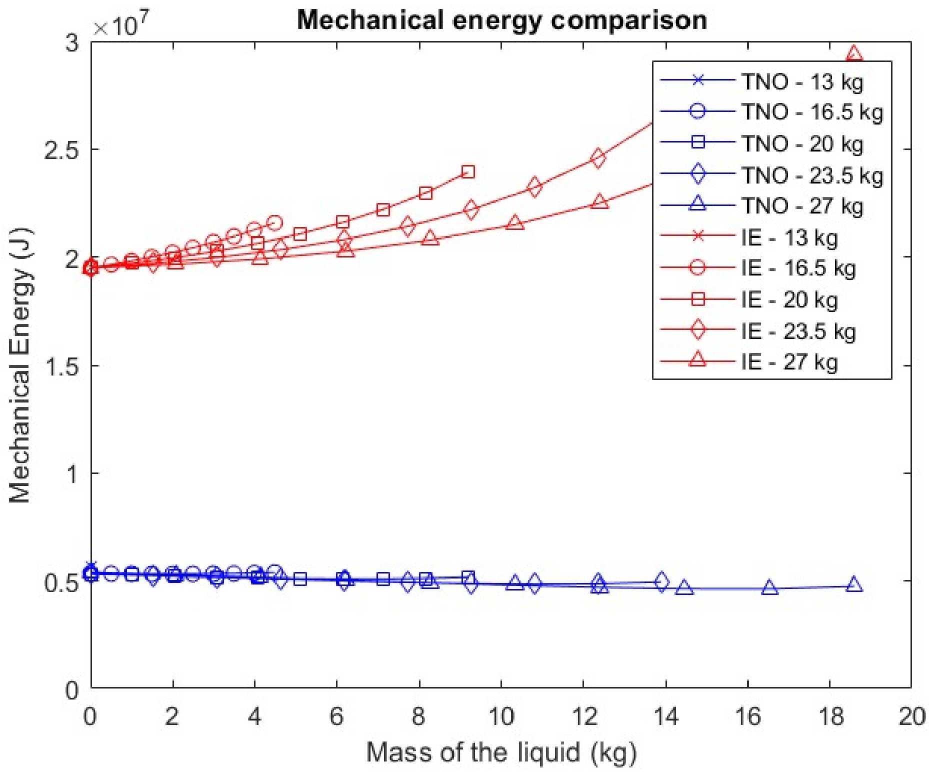

Figure 5.10: Mechanical energy: comparison of the most conservative models of real gas and ideal gas

The IGB model predicts that the energy released is greater when the total mass of hydrogen is greater. In addition, an increase in mechanical energy is associated with increasing liquid mass: this result is predicted by the equation 2.1, in which the expanding volume of the fluid is directly proportional to the mass of the liquid. It is evident that an opposite behavior is obtained when considering the RGB model. The RGB model takes into account also the expansion of the vapor phase. Given the boundary condition and the volume of the reservoir being constant ($V_T = 1$ m^3), if the mass of the liquid increases, the mass, and thus the volume, of the vapor phase decreases. This results in a decrease in the amount of vapor able to expand when the vessel bursts. This trend lasts up to a certain value of liquid mass, above which the liquid expansion contribution begins to be more significant.

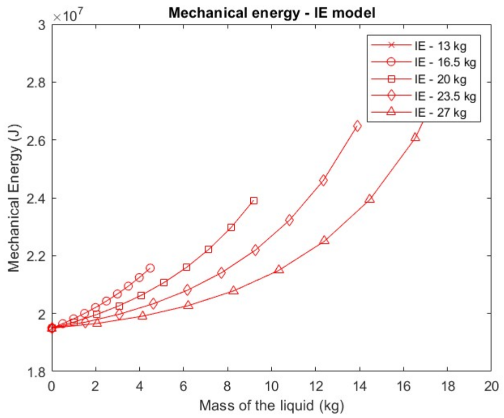

(a) Focus on the most conservative IGB model.

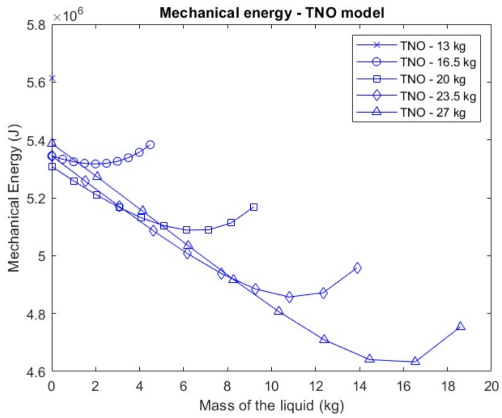

(b) Focus on the most conservative RGB model.

Figure 5.11: Mechanical energy varying the total mass of hydrogen.

5.3 Horizontal range: results

5.3.1 Prescreening

Once the mechanical energy has been evaluated and the two most conservative models have been selected, the initial velocity should be calculated, and then equations estimating the horizontal distance traveled by the fragment can be applied, considering or neglecting fluid dynamic forces. Since there are several combinations an initial screening is carried out considering an intermediate value of total mass and the corresponding maximum value of LH2 (20 kg and 19.2 kg, respectively). The results are available in table 5.3 and in figure 5.12, and they are compared with the experimental data. It is evident that some combinations can be excluded because they yield too conservative results and other combinations for the opposite reason. The analysis will progress by considering the following two combinations:

1. IE - 4 % - CFF;

2. TNO - 40 % - NFF.

In table 5.4 and 5.5 the results for all hydrogen mass values (see table 5.2) are available. Clearly, the values follow the trend of mechanical energy: when using the ideal gas model, a greater mass corresponds to a greater distance, and the opposite is true when using the real gas model.

For the sake of completeness, it is necessary to specify that at this stage only an angle of 10° was considered when applying the NFF model and an end cap shape when applying the CFF model. Then the analysis is extended to other angles and shapes.

Table 5.3: First trial by applying all possible combinations to an intermediate value of mass.

Mechanical energy model	**Energy fraction (λ)**	**NFF**	**CFF**	$\mathbf{R_{exp,MAX}}$
IE	4 %	91.4 m	191 m	167 m
	40 %	914 m	701 m	
TNO	4 %	19.8 m	52.4 m	
	40 %	198 m	322 m	

Table 5.4: Extending the analysis to all the mass: IE - 4% - CFF.

	$\mathbf{m_{TOT}}$**[kg]**				
	13	16.5	20.0	23.5	27.0
Varying liquid mass	163 m	163 m	163 m	163 m	163 m
	163 m	164 m	165 m	165 m	164 m
	163 m	165 m	166 m	166 m	166 m
	163 m	167 m	168 m	169 m	168 m
	163 m	168 m	171 m	172 m	172 m
	163 m	169 m	174 m	176 m	176 m
	163 m	171 m	177 m	181 m	183 m
	163 m	173 m	181 m	187 m	192 m
	163 m	175 m	186 m	196 m	205 m
	163 m	177 m	192 m	207 m	222 m

Table 5.5: Extending the analysis to all the mass: TNO - 40% - NFF.

	$\mathbf{m_{TOT}}$**[kg]**				
	13	16.5	20.0	23.5	27.0
Varying liquid mass	214 m	204 m	203 m	204 m	206 m
	214 m	204 m	201 m	201 m	201 m
	214 m	203 m	199 m	198 m	197 m
	214 m	203 m	197 m	194 m	192 m
	214 m	203 m	196 m	191 m	188 m
	214 m	203 m	195 m	189 m	184 m
	214 m	203 m	194 m	187 m	180 m
	214 m	204 m	194 m	186 m	177 m
	214 m	205 m	195 m	186 m	177 m
	214 m	206 m	197 m	189 m	182 m

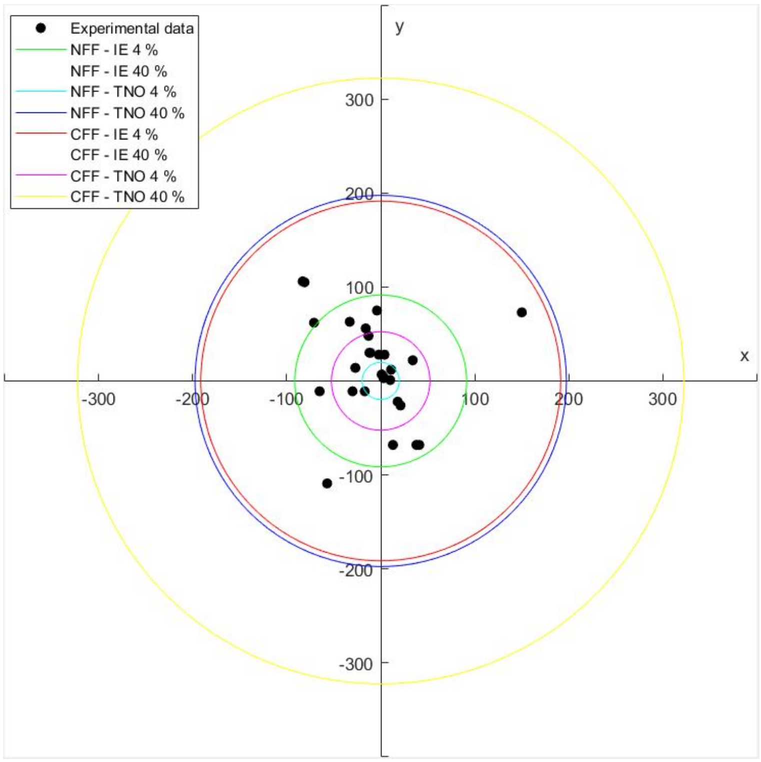

Figure 5.12: Results of different combinations and comparison to experimental data.

5.3.2 Application to experimental data

This section provides the outcomes of using different angles of departure (NFF method) and the actual shapes of each fragment (CFF method).
The initial angle of fragments is typically 5÷10°; tables 5.6-5.11 collect the results. Imposing a departure angle of 10° leads to the most conservative results (table 5.11). Comparing the outcomes with experimental data from the SH_2IFT project, this method can be useful to get a rough estimation of the hazardous distance. It certainly cannot specifically predict the distance of each fragment, since it does not distinguish between mass or shape. Again, this method is coupled with the RGB model: for this reason, it gives more conservative results with smaller liquid mass values, as explained above (section 5.2).

In tables 5.13-5.23 the results of the application of CFF method to each fragment are provided: the actual shapes and the masses are taken into account. More in detail:

- tables 5.13-5.18 show the results corresponding to the estimation of the drag coefficient according to table 4.2
- tables 5.19-5.23 collect the results obtained using equations 4.13 and 4.15 for the calculation of the coefficient.

Table 5.6: NFF - $\alpha = 5°$: results.

	$\mathbf{m_{TOT}[kg]}$				
	13	16.5	20.0	23.5	27.0
Varying liquid mass	109 m	104 m	103 m	104 m	105 m
	109 m	103 m	102 m	102 m	102 m
	109 m	103 m	101 m	100 m	100 m
	109 m	103 m	100 m	99 m	98 m
	109 m	103 m	100 m	97 m	95 m
	109 m	103 m	99 m	96 m	93 m
	109 m	103 m	99 m	95 m	91 m
	109 m	104 m	99 m	94 m	90 m
	109 m	104 m	99 m	95 m	90 m
	109 m	104 m	100 m	96 m	92 m

Table 5.7: NFF - $\alpha = 6°$: results.

	$\mathbf{m_{TOT}[kg]}$				
	13	16.5	20.0	23.5	27.0
Varying liquid mass	130 m	124 m	123 m	124 m	125 m
	130 m	124 m	122 m	122 m	122 m
	130 m	124 m	121 m	120 m	120 m
	130 m	124 m	120 m	118 m	117 m
	130 m	123 m	119 m	116 m	114 m
	130 m	124 m	119 m	115 m	112 m
	130 m	124 m	118 m	113 m	109 m
	130 m	124 m	118 m	113 m	108 m
	130 m	124 m	119 m	113 m	108 m
	130 m	125 m	120 m	115 m	110 m

Table 5.8: NFF - $\alpha = 7°$: results.

	$\mathbf{m_{TOT}}$**[kg]**				
	13	16.5	20.0	23.5	27.0
Varying liquid mass	152 m	144 m	143 m	144 m	146 m
	152 m	144 m	142 m	142 m	142 m
	152 m	144 m	141 m	140 m	139 m
	152 m	144 m	140 m	137 m	136 m
	152 m	144 m	139 m	135 m	133 m
	152 m	144 m	138 m	133 m	130 m
	152 m	144 m	138 m	132 m	127 m
	152 m	144 m	138 m	131 m	125 m
	152 m	145 m	138 m	132 m	125 m
	130 m	125 m	120 m	115 m	110 m

Table 5.9: NFF - $\alpha = 8°$: results.

	$\mathbf{m_{TOT}}$**[kg]**				
	13	16.5	20.0	23.5	27.0
Varying liquid mass	173 m	165 m	163 m	165 m	166 m
	173 m	164 m	162 m	162 m	162 m
	173 m	164 m	160 m	159 m	159 m
	173 m	164 m	159 m	157 m	155 m
	173 m	164 m	158 m	154 m	151 m
	173 m	164 m	157 m	152 m	148 m
	173 m	164 m	157 m	150 m	145 m
	173 m	164 m	157 m	150 m	143 m
	173 m	165 m	157 m	150 m	143 m
	173 m	166 m	159 m	153 m	146 m

Table 5.10: NFF - $\alpha = 9°$: results.

	$\mathbf{m_{TOT}}$**[kg]**				
	13	16.5	20.0	23.5	27.0
Varying liquid mass	194 m	185 m	183 m	185 m	186 m
	194 m	184 m	181 m	181 m	182 m
	194 m	184 m	180 m	178 m	178 m
	194 m	184 m	178 m	176 m	174 m
	194 m	184 m	177 m	173 m	170 m
	194 m	184 m	176 m	170 m	166 m
	194 m	184 m	176 m	169 m	163 m
	194 m	184 m	176 m	168 m	160 m
	194 m	185 m	177 m	168 m	160 m
	194 m	186 m	178 m	171 m	164 m

Table 5.11: NFF - $\alpha = 10°$: results.

	$\mathbf{m_{TOT}}$**[kg]**				
	13	16.5	20.0	23.5	27.0
Varying liquid mass	214 m	204 m	203 m	204 m	206 m
	214 m	204 m	201 m	201 m	201 m
	214 m	203 m	199 m	198 m	197 m
	214 m	203 m	197 m	194 m	192 m
	214 m	203 m	196 m	191 m	188 m
	214 m	203 m	195 m	189 m	184 m
	214 m	203 m	194 m	187 m	180 m
	214 m	204 m	194 m	186 m	177 m
	214 m	205 m	195 m	186 m	177 m
	214 m	206 m	197 m	189 m	182 m

In the latter case, the fragment's thickness is a key parameter for the coefficient estimation. Therefore, it is necessary to emphasize that the calculations are repeated twice for the fragment attached to the support (no. 19). In the first case (table 5.21) the thickness of the outer shell is considered (δ_{OV}), while in the second case (table 5.22) a thicker fragment is considered (δ_{19}) due to the complexity of the geometry. Since the thickness and the shapes are critical factors, fragments no.19 and no.48 give the same results and fragments no.38 and no.47 as well.
For ease of reading, the experimental data for the main fragments are extracted and reported in table 5.12, after applying the correction as in the equation 4.1.

Table 5.12: Experimental data of main fragments

No. of fragment	**m [kg]**	**d [m]**	**Description**
1	124	7	Inner shell + end cap
4	61	23	Inner end
19	261	30	Outer shell + stand
38	72	167	Outer end
47	76	66	Outer end
48	65	123	Outer shell

At this point, it is possible to make some specific considerations for each fragment:

- Fragment no.1: the first way of calculating the drag coefficient is not very reliable because it considers a geometry different from the actual one (see 5.13); however, even considering the correct geometry (see 5.19) the modeling results greatly overestimate the experimental data.

- Fragment no. 4: also in this case the models overestimate the experimental data (see tables 5.14 and 5.20).

- Fragment no. 19: the two methods of calculating the drag coefficient give the same results overestimating the experimental data (see tables 5.15 and 5.21). Even the correction about the thickness does not provide any improvement in the estimation (see table 5.22). It is worth noting that the presence of the support distorts the geometry making it difficult to approximate and probably altered the trajectory of the fragment after the explosion.

- Fragment no. 38: the predictions depend greatly on the mass of liquid hydrogen taken into account. Emphasizing again that this combination of models involves considering hydrogen as an ideal gas, the calculation gives a larger result when a larger mass is considered. Hence, it is possible to predict the experimental data only by using larger values (see tables 5.16 and 5.23).

- Fragment no. 47: the models overestimate the experimental data (see tables 5.17 and 5.23); the reason could be that the tank burst and tilted slightly, turning an end cap toward the ground.
- Fragment no. 48: the two methods of calculating the drag coefficient give different results (see tables 5.18 and 5.21); the second method gives more conservative results, but still underestimates the experimental data.

Overall, this analysis shows that the models are not able to predict the distance traveled by fragments of the inner tank because they flew much closer than those of the outer vessel.

Table 5.13: CFF - Fragment no.1: results.

	$\mathbf{m_{TOT}}$**[kg]**				
	13	16.5	20.0	23.5	27.0
Varying liquid mass	133 m	133 m	133 m	133 m	133 m
	133 m	134 m	134 m	134 m	134 m
	133 m	135 m	135 m	135 m	135 m
	133 m	135 m	136 m	136 m	136 m
	133 m	136 m	138 m	138 m	138 m
	133 m	137 m	139 m	140 m	141 m
	133 m	138 m	141 m	143 m	144 m
	133 m	139 m	143 m	147 m	149 m
	133 m	140 m	146 m	151 m	155 m
	133 m	141 m	149 m	156 m	167 m

Table 5.14: CFF - Fragment no.4: results.

	$\mathbf{m_{TOT}[kg]}$				
	13	16.5	20.0	23.5	27.0
Varying liquid mass	100 m	100 m	100 m	100 m	100 m
	100 m	100 m	100 m	100 m	100 m
	100 m	101 m	101 m	101 m	101 m
	100 m	101 m	101 m	101 m	101 m
	100 m	101 m	102 m	102 m	102 m
	100 m	101 m	102 m	103 m	103 m
	100 m	102 m	103 m	104 m	105 m
	100 m	102 m	104 m	106 m	108 m
	100 m	103 m	106 m	109 m	112 m
	100 m	103 m	108 m	113 m	119 m

Table 5.15: CFF - Fragment no.19: results.

	$\mathbf{m_{TOT}[kg]}$				
	13	16.5	20.0	23.5	27.0
Varying liquid mass	84 m	84 m	84 m	84 m	84 m
	84 m	84 m	84 m	84 m	84 m
	84 m	85 m	85 m	85 m	85 m
	84 m	85 m	86 m	86 m	86 m
	84 m	85 m	86 m	87 m	87 m
	84 m	86 m	87 m	88 m	88 m
	84 m	86 m	88 m	90 m	90 m
	84 m	87 m	90 m	92 m	93 m
	84 m	88 m	91 m	94 m	97 m
	84 m	88 m	93 m	97 m	106 m

Table 5.16: CFF - Fragment no.38: results.

	$\mathbf{m_{TOT}[kg]}$				
	13	16.5	20.0	23.5	27.0
Varying liquid mass	142 m	142 m	142 m	142 m	142 m
	142 m	143 m	144 m	144 m	143 m
	142 m	144 m	145 m	145 m	145 m
	142 m	145 m	146 m	147 m	146 m
	142 m	146 m	148 m	149 m	149 m
	142 m	147 m	150 m	152 m	153 m
	142 m	148 m	153 m	156 m	158 m
	142 m	150 m	156 m	161 m	165 m
	142 m	151 m	160 m	169 m	175 m
	142 m	153 m	165 m	176 m	187 m

Table 5.17: CFF - Fragment no.47: results.

	$\mathbf{m_{TOT}[kg]}$				
	13	16.5	20.0	23.5	27.0
Varying liquid mass	145 m	145 m	145 m	145 m	145 m
	145 m	146 m	146 m	146 m	146 m
	145 m	147 m	147 m	147 m	147 m
	145 m	147 m	149 m	149 m	149 m
	145 m	149 m	151 m	152 m	151 m
	145 m	150 m	153 m	155 m	155 m
	145 m	151 m	156 m	159 m	160 m
	145 m	152 m	159 m	164 m	167 m
	145 m	154 m	163 m	171 m	178 m
	145 m	155 m	167 m	181 m	191 m

Table 5.18: CFF - Fragment no.48: results.

	$\mathbf{m_{TOT}}$[kg]				
	13	16.5	20.0	23.5	27.0
Varying liquid mass	66 m	66 m	66 m	66 m	66 m
	66 m	66 m	66 m	66 m	66 m
	66 m	67 m	67 m	67 m	67 m
	66 m	67 m	67 m	67 m	67 m
	66 m	67 m	67 m	67 m	67 m
	66 m	67 m	68 m	68 m	68 m
	66 m	67 m	68 m	69 m	69 m
	66 m	68 m	69 m	70 m	71 m
	66 m	68 m	70 m	71 m	73 m
	66 m	68 m	71 m	73 m	77 m

Table 5.19: CFF - Fragment no.1, alternative method evaluating drag factor: results.

	$\mathbf{m_{TOT}}$[kg]				
	13	16.5	20.0	23.5	27.0
Varying liquid mass	125 m	125 m	125 m	125 m	125 m
	125 m	126 m	126 m	126 m	126 m
	125 m	127 m	127 m	127 m	127 m
	125 m	127 m	128 m	128 m	128 m
	125 m	128 m	129 m	130 m	130 m
	125 m	129 m	130 m	131 m	132 m
	125 m	129 m	132 m	134 m	135 m
	125 m	130 m	134 m	137 m	139 m
	125 m	131 m	136 m	141 m	147 m
	125 m	132 m	139 m	149 m	161 m

Table 5.20: CFF - Fragment no.4, alternative method evaluating drag factor: results.

	$\mathbf{m_{TOT}[kg]}$				
	13	16.5	20.0	23.5	27.0
Varying liquid mass	129 m	129 m	129 m	129 m	129 m
	129 m	130 m	130 m	130 m	130 m
	129 m	130 m	131 m	131 m	131 m
	129 m	131 m	132 m	132 m	132 m
	129 m	132 m	133 m	134 m	134 m
	129 m	132 m	135 m	136 m	136 m
	129 m	133 m	137 m	138 m	139 m
	129 m	134 m	138 m	141 m	143 m
	129 m	135 m	141 m	145 m	150 m
	129 m	137 m	143 m	152 m	164 m

Table 5.21: CFF - Fragments no.19 and no.48, alternative method evaluating drag factor: results.

	$\mathbf{m_{TOT}[kg]}$				
	13	16.5	20.0	23.5	27.0
Varying liquid mass	84 m	84 m	84 m	84 m	84 m
	84 m	84 m	84 m	84 m	84 m
	84 m	85 m	85 m	85 m	85 m
	84 m	85 m	86 m	86 m	86 m
	84 m	85 m	86 m	87 m	87 m
	84 m	86 m	87 m	88 m	88 m
	84 m	86 m	88 m	90 m	90 m
	84 m	87 m	90 m	92 m	93 m
	84 m	88 m	91 m	94 m	97 m
	84 m	88 m	93 m	97 m	106 m

Table 5.22: CFF - Fragment no.19b, alternative method evaluating drag factor: results.

	$\mathbf{m_{TOT}}$**[kg]**				
	13	16.5	20.0	23.5	27.0
Varying liquid mass	108 m	108 m	108 m	108 m	108 m
	108 m	109 m	109 m	109 m	109 m
	108 m	110 m	110 m	110 m	110 m
	108 m	111 m	112 m	112 m	112 m
	108 m	111 m	113 m	114 m	113 m
	108 m	112 m	115 m	116 m	116 m
	108 m	113 m	117 m	119 m	120 m
	108 m	114 m	119 m	123 m	124 m
	108 m	115 m	122 m	125 m	128 m
	108 m	116 m	124 m	128 m	134 m

Table 5.23: CFF - Fragments no.38 and no.47, alternative method evaluating drag factor: results.

	$\mathbf{m_{TOT}}$**[kg]**				
	13	16.5	20.0	23.5	27.0
Varying liquid mass	141 m	141 m	141 m	141 m	141 m
	141 m	142 m	142 m	142 m	142 m
	141 m	142 m	143 m	143 m	143 m
	141 m	143 m	145 m	145 m	145 m
	141 m	144 m	146 m	147 m	147 m
	141 m	145 m	149 m	150 m	151 m
	141 m	147 m	151 m	155 m	156 m
	141 m	148 m	155 m	160 m	164 m
	141 m	150 m	159 m	166 m	172 m
	141 m	151 m	163 m	173 m	183 m

Focus on the initial velocity: results

As mentioned several times in this thesis, the initial velocity is a key factor in the implementation of these models. For this reason, it was worthwhile to explore this issue further.
From the video analysis of the experiments, it is possible to distinguish only three fragments since the first moment of the vessel burst. For these, the initial velocity was estimated using equation 4.17 and the models were applied respecting the shape of the fragment (CFF model) and proposing a plausible range of angles (NFF model). Tables 5.24 - 5.26 show the results.

Table 5.24: Initial velocity from video analysis: results for fragment no.38.

Fragment no. 38						
m	72 kg					
$\mathbf{R_{exp}}$	167 m					
$\mathbf{v_{exp}}$	67 m/s					
α	10°	11°	12°	13°	14°	15°
$\mathbf{R_{NFF}}$	157 m	172 m	186 m	201 m	215 m	229 m
Drag Coefficient	0.41					
$\mathbf{R_{CFF}}$	225 m					

Table 5.25: Initial velocity from video analysis: results for fragment no.47.

Fragment no. 47						
m	76 kg					
$\mathbf{R_{exp}}$	66 m					
$\mathbf{v_{exp}}$	60 m/s					
α	5°	6°	7°	8°	9°	10°
$\mathbf{R_{NFF}}$	64 m	76 m	89 m	101 m	114 m	126 m
Drag Coefficient	0.43					
$\mathbf{R_{CFF}}$	232 m					

Even using the initial velocity value estimated from the video analysis, the NNF model gives not overly conservative results for assessing the maximum horizontal range (see table 5.24). The CFF model, on the other hand, has so far been applied at lower initial velocity values than the NFF model: the combination IE - 4% provides smaller values than TNO - 40%. At this point, it is obvious that by applying the CFF model with the same initial velocity values as the NFF model, the results are extremely conservative. In fact, considering the same velocity value, the two models give comparable results

Table 5.26: Initial velocity from video analysis: results for fragment no.48.

Fragment no. 48						
m	65 kg					
$\mathbf{R_{exp}}$	123 m					
$\mathbf{v_{exp}}$	121 m/s					
α	10°	11°	12°	13°	14°	15°
$\mathbf{R_{NFF}}$	511 m	559 m	607 m	655 m	700 m	746 m
Drag Coefficient	1.22					
$\mathbf{R_{CFF}}$	362 m					

only when an angle of 45° (horizontal tank) is considered. From the data evaluated from the video analysis, a range of initial velocities was defined, and calculations were repeated for each fragment for each velocity value (see table 5.28). With the NFF model, a change in the departure angle was also considered, being the other critical parameter of the model.

Table 5.27 depcits results for the NFF model: again, the method does not distinguish between fragments. As predicted by the equation 2.17, the velocity dependence is quadratic, so considering a high value leads to conservative results. The angle dependence is less strong, but when coupled with high initial velocities, the result is excessively conservative.

The results for the CFF model are available in table 5.28: for high-velocity values, the considerations already stated for tables 5.24-5.26 are true. The outcomes for the two tube-ends are clearly the same, although the experiments show differences. The reason could be the initial rupture point of thank.

Finally, it is necessary to point out that the horizontal range related to the fragments of the inner reservoir is overestimated by each model. Probably, the cause is the different energy distribution given by the particularity of this tank. However, to build further hypothesis, more experimental data would be needed, which are not available at the moment.

Table 5.27: NFF - Range of initial velocity and initial angle: results.

		α							
		2.5 °	5	7.5°	10°	12.5°	15°	17.5°	20°
$\mathbf{v_i}$ [m/s]	40	14 m	28 m	42 m	56 m	69 m	82 m	94 m	105 m
	50	22 m	44 m	66 m	87 m	108 m	127 m	146 m	164 m
	60	32 m	64 m	95 m	126 m	155 m	183 m	210 m	236 m
	70	44 m	87 m	129 m	171 m	211 m	250 m	286 m	321 m
	80	57 m	113 m	169 m	223 m	276 m	326 m	374 m	419 m
	90	72 m	143 m	214 m	282 m	349 m	413 m	474 m	531 m
	100	89 m	177 m	264 m	349 m	431 m	510 m	585 m	655 m
	110	108 m	214 m	319 m	422 m	521 m	617 m	707 m	793 m
	120	128 m	255 m	380 m	502 m	620 m	734 m	842 m	944 m

Table 5.28: CFF - Range of initial velocity: results.

		Fragment no.					
		1	4	19	37	47	48
$\mathbf{R_{exp}}$		6.7 m	23 m	30 m	167 m	66 m	123 m
$\mathbf{v_i}$**[m/s]**	40	104 m	106 m	91 m	115 m	115 m	75 m
	50	135 m	140 m	121 m	158 m	158 m	91 m
	60	174 m	177 m	141 m	193 m	193 m	112 m
	70	196 m	203 m	163 m	239 m	239 m	124 m
	80	223 m	231 m	189 m	267 m	267 m	141 m
	90	260 m	267 m	205 m	298 m	298 m	154 m
	100	277 m	289 m	228 m	330 m	330 m	168 m
	110	299 m	309 m	248 m	373 m	373 m	177 m
	120	326 m	337 m	264 m	394 m	394 m	189 m

5.4 Mitigation of consequences

In the field of safety, mitigation is defined as “lessening the risk of an accident event sequence by acting on the source in a preventive way by reducing the likelihood of occurrence of the event, or in a protective way by reducing the magnitude of the event and/or the exposure of local persons or property” [14]. In this analysis, the objective is to mitigate the consequences of a BLEVE of a liquid hydrogen tank; thus, reference must be made to the second part of the definition just mentioned. In more detail, the consequence under investigation is the projection of fragments.

The first parameter to consider when acting on mitigation may be the mass of the tank; obviously, a lighter tank would generate lighter and, therefore, potentially less danger-

ous fragments. However, according to model equations for predicting the distance, the range of the fragments may be longer when the same kinetic energy is produced by the explosion. Therefore, reducing the weight of vessels, which is desired in many applications such as automotive, would not necessarily help to lessen the effects of an explosion.
This section provides some mitigation proposals:

- In the SH_2IFT project experiment, the cylindrical part of the outer vessel broke into two parts: one of them (fragment no. 19) was stuck to the stand that had the function of supporting the tank under operating conditions. It can be observed that this fragment traveled a much shorter distance than the other part of the shell (fragment no. 48) as if it had been kept back by the presence of the support. This suggests the possibility of confining the flight of fragments by looking for such a solution for hemispherical bottoms as well.

- Again, in the SH_2IFT project experiment, a fragment of the inner vessel (no. 4) crashed into the protective wall of the propane tank, allowing the horizontal range to be limited. This suggests the possibility of limiting the fragments projection by creating a kind of barrier in the area around the tank that is in danger of exploding. However, confinement could lead to a possible amplification of the pressure wave; a proper balance between the two effects and higher cost must be found.

- As pointed out in the previous chapters, a tank can fail through different fragmentation patterns (see section 4.1.1). In addition to being a probabilistic event, they may depend on the design of the tank. The Finite Element Method (FEM) together with the Computational Fluid Dynamics (CFD) modeling can be adopted to conduct a proper structural analysis of the double-walled tank. Finding the weak points of the tank (e.g. welds) may suggest the best orientation to place the tank, as this may affect the departure angle of the generated fragments.

6 Conclusion

This work focused on the analysis of one of the potential accidents that may arise from a liquid hydrogen tank: BLEVE - *Boiling Liquid Expanding Vapour Explosion*. Models often applied to hazardous scenario concerning conventional fuels (e.g. propane, liquefied petroleum gas) were applied to LH_2 simulated accidents with the purpose to describe one of the aftermaths of the hydrogen BLEVE: the projection of fragments. Indeed, predicting how they are distributed in space and how far they can spread is vital to define the hazardous distance.
Distribution in space showed to be consistent with that for conventional fluids and tanks: the tank axis turned out to be the principal direction.
Two different models were used during the analysis: the Neglecting Fluid dynamic Forces (NFF) model and the Considering Fluid dynamic Forces (CFF) model. Each of these two requires as input data the initial velocity of the fragment, which can be estimated from the mechanical energy released by the explosion and intended for fragment generation. According to previous studies, the conventional models, classified as "Real Gas Behavior" (RGB) and "Ideal Gas Behavior" (IGB), were implemented to estimate the mechanical energy liberated with the explosions and two different factors were considered as the percentage of energy destined to fragment generation and projection. Then, the results of the models were validated with the outcomes of the SH_2IFT project experiments that were previously processed. In addition to initial velocity, the other key parameters for evaluating the distance traveled by fragments are the initial angle (if using the NFF model) and the shape and mass of the fragment (if using the CFF model).

To sum up, results showed which model has to be selected for liquid hydrogen tanks depending if the fluid dynamic forces are considered or not in the analysis to assess the horizontal range of the fragments. The innovation in this analysis was taking into account the peculiarity of the tank required for liquid hydrogen storage: a double-walled vessel. Overall, it has emerged that the NFF model can only be useful in defining the maximum distance a fragment can reach. The CFF model gave more or less accurate results when applied to the fragments of the outer tank. However, when applied to the

fragments of the inner vessel, it gave results that greatly overestimated the experimental data.
The fragments of the inner tank travel a shorter distance compared with those of the outer tank; probably the cause is the uneven distribution of energy between the outer and inner tanks. However, additional considerations and proposed changes to the models must be put on hold until new experimental data are available.

In conclusion, hydrogen has been identified as a potential solution to the need for clean and sustainable energy sources. However, its implementation in new environments may carry several operational uncertainties, given the relatively reduced safety-related experience. The only way to overcome this challenge is to investigate safety during the production, transportation, and final use processes of hydrogen, creating a shared knowledge of its applicability. More research on these processes needs to be conducted to obtain new and essential information. Regarding the fragment projection which is the topic of this work, more experimental data would be needed to further investigate the behavior of the double-walled tank.

Annex A

Table 6.1: Fragment experimental data. "Vessel" denotes the initial coordinates of the tank.

No. of fragment	**m [kg]**	**x**	**y**
vessel	730	392 670 325	5 774 327 492
1	**124**	**392 671 232**	**5 774 334 081**
2	1	392 673 730	5 774 331 114
3	2	392 672 926	5 774 330 026
4	**61**	**392 680 643**	**5 774 328 451**
5	1	392 688 638	5 774 305 413
6	4	392 691 672	5 774 301 201
7	<1	392 689 618	5 774 291 531
8	<1	392 651 980	5 774 300 290
9	<1	392 654 816	5 774 306 013
10	13	392 653 593	5 774 316 580
11	<1	392 653 716	5 774 320 323
12	<1	392 646 420	5 774 319 837
13	1	392 640 636	5 774 316 882
14	<1	392 653 804	5 774 331 442

15	<1	392 664 413	5 774 329 344
16	<1	392 657 236	5 774 337 234
17	<1	392 650 849	5 774 336 288
18	<1	392 644 649	5 774 340 906
19	**261**	**392 643 550**	**5 774 341 289**
20	<1	392 644 005	5 774 355 908
21	<1	392 643 173	5 774 356 207
22	1	392 658 225	5 774 357 310
23	1	392 658 989	5 774 357 477
24	<1	392 660 318	5 774 359 147
25	<1	392 660 382	5 774 360 276
26	<1	392 663 485	5 774 361 550
27	<1	392 663 366	5 774 346 601
28	2	392 668 707	5 774 355 475
29	<1	392 669 479	5 774 355 627
30	<1	392 671 261	5 774 355 882
31	2	392 674 192	5 774 355 685
32	<1	392 668 517	5 774 363 929
33	<1	392 668 247	5 774 364 192
34	<1	392 678 339	5 774 360 846
35	<1	392 677 995	5 774 348 254
36	1	392 681 025	5 774 339 255
37	1	392 680 980	5 774 339 340

38	**72**	**392 820 442**	**5 774 400 942**
39	2	392 665 996	5 774 402 421
40	<1	392 661 245	5 774 474 817
41	2	392 587 217	5 774 433 971
42	1	392 588 932	5 774 432 968
43	5	392 637 738	5 774 390 309
44	1	392 654 666	5 774 383 567
45	2	392 657 457	5 774 375 813
46	1	392 599 551	5 774 389 952
47	**76**	**392 605 295**	**5 774 316 198**
48	**65**	**392 612 936**	**5 774 218 942**
49	<1	392 674 424	5 774 271 929
50	1	392 682 865	5 774 259 334
51	1	392 704 398	5 774 349 298
52	2	392 708 224	5 774 259 409
53	2	392 711 106	5 774 259 681

Annex B

(a)

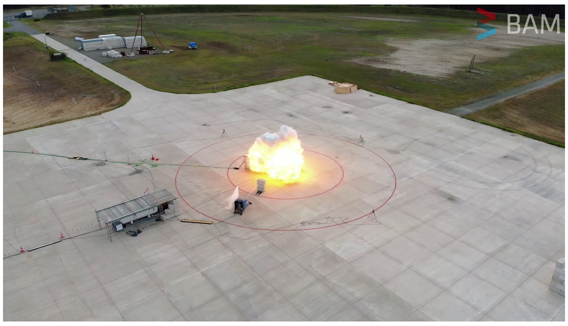

(b)

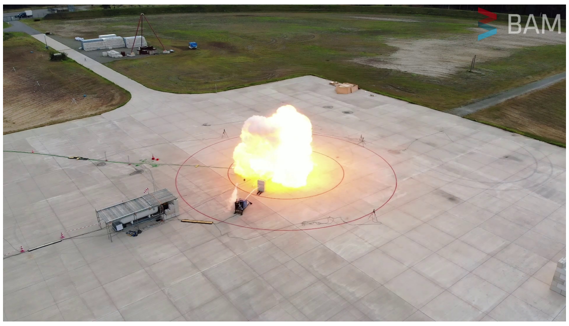

(c)

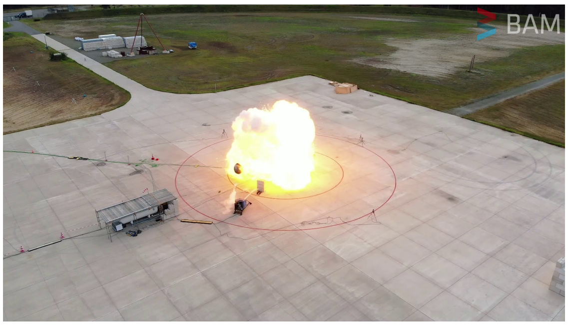

(d)

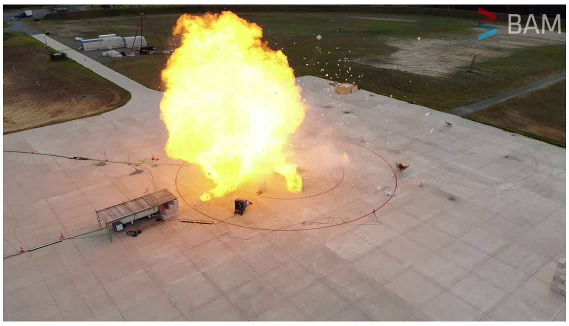

(e)

Figure 6.1: Pictures from Drone.

(a)

(b)

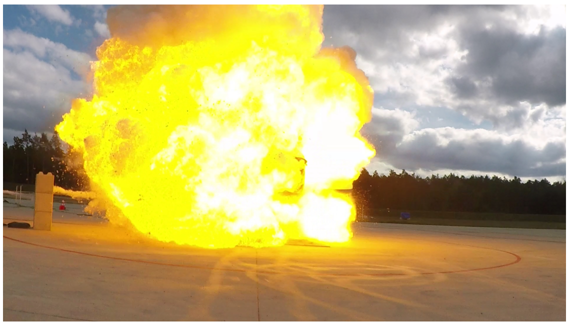

(c)

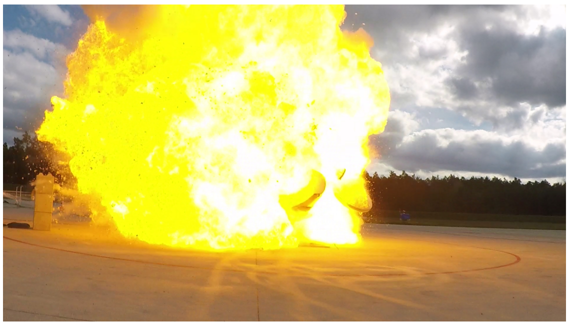

(d)

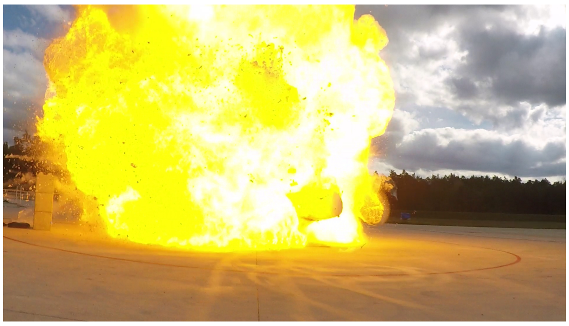

(e)

Figure 6.2: Pictures from GoPro - North.

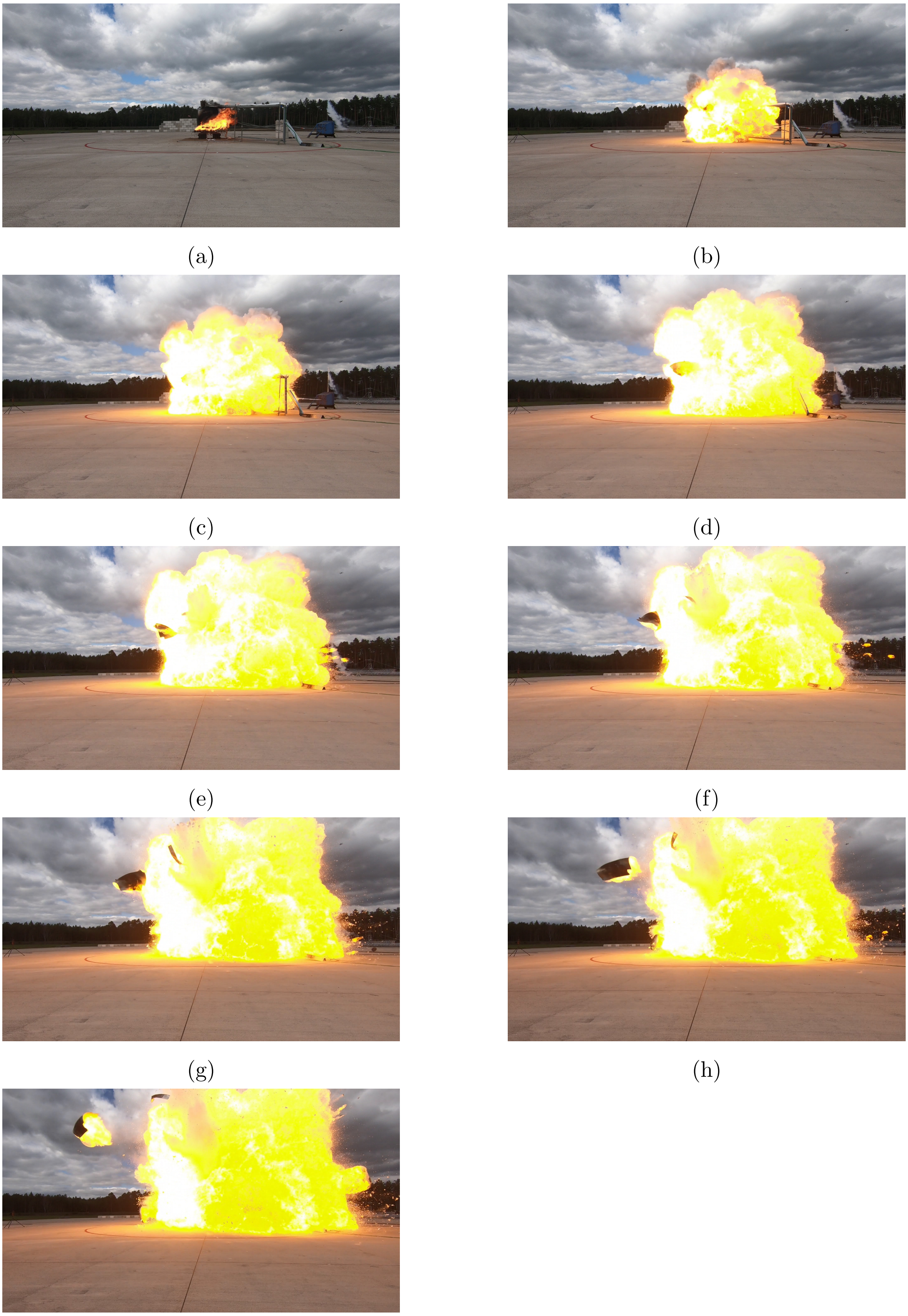

(a) (b) (c) (d) (e) (f) (g) (h) (i)

Figure 6.3: Pictures from GoPro - South.

(a)

(b)

(c)

(d)

(e)

(f)

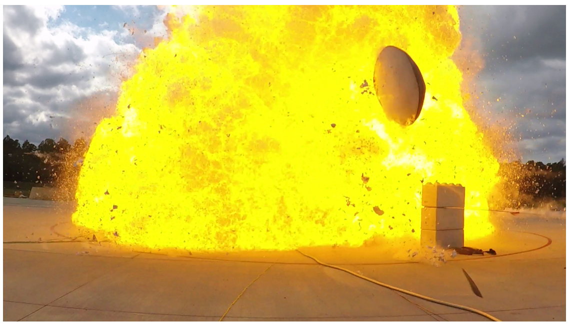

(g)

(h)

Figure 6.4: Pictures from GoPro - East.


(a)


(b)


(c)

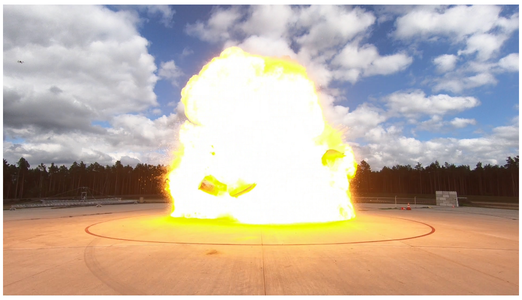
(d)

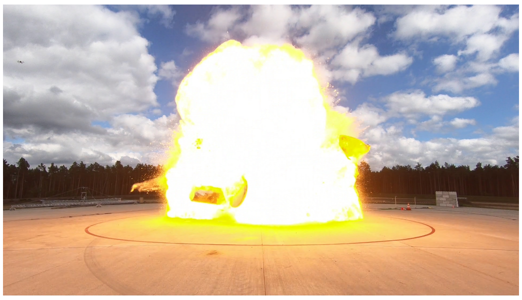
(e)

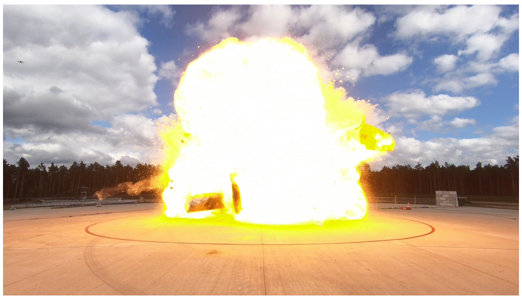
(f)


(g)


(h)

Figure 6.5: Pictures from GoPro - West.

Annex C

Mechanical Energy

```
Sub = 'Parahydrogen'; % name of the substance
% Experimental data
m_i = 27; % total mass of the tank [kg], at the beginning it is total liquid (in the storage tank not in the experimental tank)
V_T = 1; % total volume of the tank [m3]
D_T = 1.115; % vessel diameter [m]
m_T = 730; % vessel mass [kg]
P_0 = 101325; % atmospheric pressure [Pa]
T_c = py.CoolProp.CoolProp.PropsSI('Tcrit','',0,'',0,Sub);
gamma = 1.4;
TNT = 4680 * 10^3;  % heat of explosion for TNT [J/kg]
g = 9.81; % acceleration of gravity in [m/s^2]
R = 8.316; % ideal gas constant [J/molK]
Mw = 2.016 * 10^-3; % molar weight [kg/mol]

 % Pressure of the tank before explosion:50 bar [Pa]
 P_exp = 5000000;

%% INITIAL MASSES AND VOLUMES

% Gas saturated temperature at 9.5 bar [K]
P_vap = 9.5 * 10^5; % [Pa]
T_GH2_1 = % CoolProp Data %
T_GH2_mis = % CoolProp Data %  Gas temperature calculated for the vapour phase [K]

% Gas density at T GH2 1 and 9.5 bar [kg/m 3]
D_GH2_1 =  % CoolProp Data %
D_GH2_lim = % CoolProp Data % Finding the minimum mass at P = 50bar and Tmax=-180C

% Liquid density at T sat and 9.5 bar [kg/m 3]
D_LH2_1 = % CoolProp Data %

```

```
% About m_tot: assume the old scenario, Tvap = T_GH2_1 and P = P_vap -->
% Density is about 13.2kg, so let's consider it as the minimum mass.

m_tot = linspace(D_GH2_lim, m_i, 5);

M_LH2_ft = 10*ones(length(m_tot)); % first try liquid mass

for m = 1:length(m_tot)

% Now it is possible to calculate the volume and the mass of the liquid and the gaseous phase
err = 1; % initialization of the err variable

while err > 0.00001
  V_LH2_ft(m) = %%%%%%%; % first try liquid Volume
  V_GH2_ft(m) = V_T - V_LH2_ft(m); % first try supercritc Volum
  M_GH2_ft(m) = V_GH2_ft(m) * D_GH2_1; % first try supercritic mass

M_LH2_st(m) = M_LH2_ft (m); % redefinition of the first try liquid mass

M_LH2_ft(m) = m_tot(m) - M_GH2_ft(m); % initialization of the variable second try liquid mass


err = abs(M_LH2_st(m) - M_LH2_ft(m)); % definition of the error
end

%%%%%%

M_GH2 = M_GH2_ft;

% EXPLODING TANK PARAMETERS
% Defining an array for different liquid temperature between T_b (boiling temperature at atmospheric pressure) and Tc
T_b = % CoolProp Data %;

T_liquid = T_c; % considering the worst scenario

M_LH2_max (m) = M_LH2 (m);
M_LH2_min = 0;

% Defining an array containing different masses from the minimum to the maximum
liquidM (:, m) = linspace(M_LH2_min,M_LH2_max (m),10);

%% Properties
% Density of the liquid at 50 bar and T liquid [kg/m 3]
```

```
D_LH2 = % CoolProp Data %;

% Vapour state at NBP
rho_Vb = % CoolProp Data %; % H2 density at NBP in [kg/m3]
h_Vb = % CoolProp Data %;   % H2 enthalpy at NBP in [J/kg]
s_Vb = % CoolProp Data %;   % H2 entropy at NBP in [J/kg*K]
u_Vb = % CoolProp Data %;   % H2 internal energy at NBP in [J/kg]
C_p_Vb = % CoolProp Data %; % H2 const press specific heat at NBP in [J/kg*K]
C_v_Vb = % CoolProp Data %;  % H2 const vol specific heat at NBP in [J/kg*K]
v_Vb = 1 / rho_Vb;                                                   % H2 specific volume at NBP in [m3/kg]

% Liquid state at NBP
rho_Lb = % CoolProp Data %;  % LH2 density at NBP in [kg/m3]
h_Lb = % CoolProp Data %;    % LH2 enthalpy at NBP in [J/kg]
s_Lb = % CoolProp Data %;    % LH2 entropy at NBP in [J/kg*K]
u_Lb = % CoolProp Data %     % LH2 internal energy at NBP in [J/kg]
C_p_Lb = % CoolProp Data %;  % LH2 const press specific heat at NBP in [J/kg*K]
C_v_Lb = % CoolProp Data %; % LH2 const vol specific heat at NBP in [J/kg*K]

v_Lb = 1 / rho_Lb;

Delta_h = h_Vb - h_Lb;

s_l = % CoolProp Data %; % specific entropy at 50 bar and T_liquid [J/kg/K]
X_l = (s_l-s_Lb)/(s_Vb-s_Lb);      % fraction of the liquid phase
u_l_is = (1-X_l)*u_Lb + X_l*u_Vb;      % specific energy of the liquid phase after the isoentropic expansion [J/kg]
u_l = % CoolProp Data %;   % Specific energy of the liquid phase before the explosion [J/kg]
h_l = % CoolProp Data %;   % Specific hentalpy of the liquid phase before the explosion [J/kg]
cpl = % CoolProp Data %;

for l = 1:1:10
liquidV(l, m) = liquidM(l, m) / D_LH2;
gaseousV(l, m)= %%%% ; %[m 3]
gaseousM(l,m) = m_tot(m) - liquidM(l,m); %[kg]
gaseousD(l,m) = gaseousM(l,m) / gaseousV(l,m); %[kg/m 3]

%% IDEAL GASES
f = %%%% ; % Definition of f, flashing fraction
```

```
V_exp(l,m) = V_T + liquidM(l,m)*(f/gaseousD(l,m) - 1/D_LH2); %[m 3]

E_Brode(l,m) = ((P_exp-P_0) * V_exp(l,m))/(gamma-1);

E_IE(l,m) = P_exp * V_exp(l,m) * log(P_exp/P_0);

E_TA(l,m) = P_exp * V_exp(l,m) * (log(P_exp/P_0)-(1-P_0/P_exp));

E_Prugh(l,m) = (P_exp * V_exp(l,m) * ((1-P_0/P_exp)^((gamma-1)/gamma))) / (gamma - 1);


%% REAL GASES

T_gas(l,m) = % CoolProp Data %;   % Gas temperature [K]

u_v(l,m) = % CoolProp Data %;  % Specific energy of the vapour phase before the explosion [J/kg]
s_v (l,m) = % CoolProp Data %;  % Specific entropy of the vapour phase before the explosion [J/kg]
X_v(l,m) = (s_v(l,m)-s_Lb)/(s_Vb-s_Lb);     % fraction of the vapour phase
u_v_is(l,m) = (1-X_v(l,m))*u_Lb + X_v(l,m)*u_Vb;

U_Vb = u_Vb / (10^6);          % H2 internal energy at NBP in [MJ/kg]
U_Lb = u_Lb / (10^6);          % LH2 internal energy at NBP in [MJ/kg]
U_v(l,m) = u_v(l,m) / (10^6);
U_l = u_l / (10^6);

U(l,m) = (gaseousM(l,m) * U_v(l,m)) + (liquidM(l,m) * U_l); % overall internal energy of the system just before the explosion in [MJ]
        x_1(l,m) = (m_tot(m) * (P_0 / (10^6)) * v_Lb) - (V_T * (P_0 / (10^6))) + (m_tot(m) * U_Lb) - U(l,m);
        x_2(l,m) = ((U_Lb - U_Vb) - (v_Vb - v_Lb) * (P_0 / (10^6))) * m_tot(m);
        X(l,m) = x_1(l,m)/ x_2(l,m);

E_TNO_L(l,m) = liquidM(l,m) * (u_l - u_l_is);     % contibution in generate the mech. en. by the liquid in [J]
E_TNO_V(l,m) = gaseousM(l,m) * (u_v(l,m) - u_v_is(l,m));          % contibution in generate the mech. en. by the vapour in [J]
E_TNO(l,m) = E_TNO_L(l,m) + E_TNO_V(l,m);           % mechanical energy generated by the explosion in [J]

E_PLANAS(l,m) =  (((U_Lb - U_Vb)* m_tot(m) * X(l,m)) - (m_T * U_Lb) +
```

```
    U(l,m)) *10^6;

k_SE=0.14;
E_SE(l,m) = k_SE * liquidM(l,m)*(h_l-h_Lb);    % mechanical energy
    generated by the explosion in [J]
E_SE_MJ(l,m) = E_SE(l,m) / 10^6;

E_B(l,m) = gaseousM(l,m)*(u_v(l,m)-u_v_is(l,m));
E_B_MJ(l,m) = E_B(l,m) / 10^6;

psi_GE = 0.07;
E_GE(l,m) = psi_GE * liquidM(l,m) * cpl * (T_liquid-T_b);    % mechanical
    energy generated by the explosion in [J]
E_GE_MJ(l,m) = E_GE(l,m) / 10^6;
end
end
```

Prescreening

```
Sub = 'Parahydrogen'; % name of the substance
% Experimental data
m_i = 27; % total mass of the tank [kg], at the beginning it is total
    liquid (in the storage tank not in the experimental tank)
V_T = 1; % total volume of the tank [m3]
D_T = 1.115; % vessel diameter [m]
m_T = 730; % vessel mass [kg]
P_0 = 101325; % atmospheric pressure [Pa]
T_c = py.CoolProp.CoolProp.PropsSI('Tcrit','',0,'',0,Sub);
gamma = 1.4;
TNT = 4680 * 10^3;  % heat of explosion for TNT [J/kg]
g = 9.81; % acceleration of gravity in [m/s^2]
R = 8.316; % ideal gas constant [J/molK]
Mw = 2.016 * 10^-3; % molar weight [kg/mol]

 % Pressure of the tank before explosion:50 bar [Pa]
 P_exp = 5000000;

%% INITIAL MASSES AND VOLUMES

% Gas saturated temperature at 9.5 bar [K]
P_vap = 9.5 * 10^5; % [Pa]
T_GH2_1 =% CoolProp Data %;
T_GH2_mis = -180 + 273.15; % Gas temperature calculated for the vapour
    phase [K]

```

```
% Gas density at T GH2 1 and 9.5 bar [kg/m 3]
D_GH2_1 =  % CoolProp Data %;
D_GH2_lim = % CoolProp Data %; % Finding the minimum mass at P = 50bar and Tmax=-180C

% Liquid density at T sat and 9.5 bar [kg/m 3]
D_LH2_1 = % CoolProp Data %;

% About m_tot: assume the old scenario, Tvap = T_GH2_1 and P = P_vap -->
% Density is about 13.2kg, so let's consider it as the minimum mass.

m_tot = linspace(D_GH2_lim, m_i, 5);

M_LH2_ft = 10*ones(length(m_tot)); % first try liquid mass

for m = 1:length(m_tot)

% Now it is possible to calculate the volume and the mass of the liquid and the gaseous phase
err = 1; % initialization of the err variable

while err > 0.00001
  V_LH2_ft(m) = M_LH2_ft(m) / D_LH2_1; % first try liquid Volume
  V_GH2_ft(m) = %%%%%; % first try supercritc Volum
  M_GH2_ft(m) = V_GH2_ft(m) * D_GH2_1; % first try supercritic mass

M_LH2_st(m) = M_LH2_ft (m); % redefinition of the first try liquid mass

M_LH2_ft(m) = %%%; % initialization of the variable second try liquid mass


err = abs(M_LH2_st(m) - M_LH2_ft(m)); % definition of the error
end

%%%%

M_GH2 = M_GH2_ft;

% EXPLODING TANK PARAMETERS
% Defining an array for different liquid temperature between T_b (boiling temperature at atmospheric pressure) and Tc
T_b = % CoolProp Data %;

T_liquid = T_c; % considering the worst scenario

M_LH2_max (m) = M_LH2 (m);
```

```
M_LH2_min = 0;

% Defining an array containing different masses from the minimum to the
    maximum
liquidM (:, m) = linspace(M_LH2_min,M_LH2_max (m),10);

%% Properties
% Density of the liquid at 50 bar and T liquid [kg/m 3]
D_LH2 = % CoolProp Data %;

% Vapour state at NBP
rho_Vb = % CoolProp Data %; % H2 density at NBP in [kg/m3]
h_Vb = % CoolProp Data %;   % H2 enthalpy at NBP in [J/kg]
s_Vb = % CoolProp Data %;   % H2 entropy at NBP in [J/kg*K]
u_Vb = % CoolProp Data %;   % H2 internal energy at NBP in [J/kg]
C_p_Vb = % CoolProp Data %;   % H2 const press specific heat at NBP in
    [J/kg*K]
C_v_Vb = % CoolProp Data %;  % H2 const vol specific heat at NBP in
    [J/kg*K]
v_Vb = 1 / rho_Vb;                                              % H2
    specific volume at NBP in [m3/kg]

% Liquid state at NBP
rho_Lb = % CoolProp Data %;      % LH2 density at NBP in [kg/m3]
h_Lb = % CoolProp Data %;        % LH2 enthalpy at NBP in [J/kg]
s_Lb = % CoolProp Data %;        % LH2 entropy at NBP in [J/kg*K]
u_Lb = % CoolProp Data %;        % LH2 internal energy at NBP in [J/kg]
C_p_Lb = % CoolProp Data %;      % LH2 const press specific heat at NBP
    in [J/kg*K]
C_v_Lb = % CoolProp Data %; % LH2 const vol specific heat at NBP in
    [J/kg*K]

v_Lb = 1 / rho_Lb;

Delta_h = h_Vb - h_Lb;

s_l = % CoolProp Data %; % specific entropy at 50 bar and T_liquid
    [J/kg/K]
X_l = (s_l-s_Lb)/(s_Vb-s_Lb);     % fraction of the liquid phase
u_l_is = (1-X_l)*u_Lb + X_l*u_Vb;     % specific energy of the liquid
    phase after the isoentropic expansion [J/kg]
u_l = % CoolProp Data %;    % Specific energy of the liquid phase before
    the explosion [J/kg]
h_l = % CoolProp Data %;    % Specific hentalpy of the liquid phase
    before the explosion [J/kg]
cpl = % CoolProp Data %;

```

```
for l = 1:1:10
liquidV(l, m) = liquidM(l, m) / D_LH2;
gaseousV(l, m)= V_T - liquidV(l,m); %[m 3]
gaseousM(l,m) = %%%%%; %[kg]
gaseousD(l,m) = gaseousM(l,m) / gaseousV(l,m); %[kg/m 3]

%% IDEAL GASES
f = %%% ; % Definition of f, flashing fraction

V_exp(l,m) = V_T + liquidM(l,m)*(f/gaseousD(l,m) - 1/D_LH2); %[m 3]

E_IE(l,m) = P_exp * V_exp(l,m) * log(P_exp/P_0);

%% REAL GASES
T_gas(l,m) = % CoolProp Data %;   % Gas temperature [K]

u_v(l,m) = % CoolProp Data %;  % Specific energy of the vapour phase before the explosion [J/kg]
s_v (l,m) = % CoolProp Data %;  % Specific entropy of the vapour phase before the explosion [J/kg]
X_v(l,m) = (s_v(l,m)-s_Lb)/(s_Vb-s_Lb);      % fraction of the vapour phase
u_v_is(l,m) = %%%%%%%;

U_Vb = u_Vb / (10^6);                        % H2 internal energy at NBP in [MJ/kg]
U_Lb = u_Lb / (10^6);                        % LH2 internal energy at NBP in [MJ/kg]
U_v(l,m) = u_v(l,m) / (10^6);
U_l = u_l / (10^6);

U(l,m) = %%%;                 % overall internal energy of the system just before the explosion in [MJ]
        x_1(l,m) = (m_tot(m) * (P_0 / (10^6)) * v_Lb) - (V_T * (P_0 / (10^6))) + (m_tot(m) * U_Lb) - U(l,m);
        x_2(l,m) =%%%%%;
        X(l,m) = x_1(l,m)/ x_2(l,m);

E_TNO_L(l,m) = liquidM(l,m) * (u_l - u_l_is);          % contibution in generate the mech. en. by the liquid in [J]
E_TNO_V(l,m) = gaseousM(l,m) * (u_v(l,m) - u_v_is(l,m));          % contibution in generate the mech. en. by the vapour in [J]
E_TNO(l,m) = E_TNO_L(l,m) + E_TNO_V(l,m);            % mechanical energy generated by the explosion in [J]

end
end
```

```
%% Initial velocity
vi_IE_4 = sqrt(2 * E_IE(10,3) * 0.04 / m_T);
vi_IE_40 = sqrt(2 * E_IE(10,3) * 0.4 / m_T);
vi_TNO_4 = sqrt(2 * E_TNO(10,3) * 0.04 / m_T);
vi_TNO_40 = sqrt(2 * E_TNO(10,3) * 0.4 / m_T);

%% NFF
alpha = 10 * pi() / 180;
R_NFF_IE_4 = vi_IE_4^2 * sin(2 * alpha) / g;
R_NFF_IE_40 = vi_IE_40^2 * sin(2 * alpha) / g;
R_NFF_TNO_4 = vi_TNO_4^2 * sin(2 * alpha) / g;
R_NFF_TNO_40 = vi_TNO_40^2 * sin(2 * alpha) / g;

%% CFF
rho_a = 1.229;  % density of air in [kg/m3]
CD_AD = %%%%;
Mf = m_T / 6;
g = 9.81;

vis_CFF_IE_4 = rho_a * CD_AD * (vi_IE_4^2) / Mf / g;
Rs_IE_4 = 0.751;
R_CFF_IE_4 = Rs_IE_4 * Mf / rho_a / CD_AD;

vis_CFF_IE_40 = rho_a * CD_AD * (vi_IE_40^2) / Mf / g;
Rs_IE_40 = 2.75;
R_CFF_IE_40 = Rs_IE_40 * Mf / rho_a / CD_AD;

vis_CFF_TNO_4 = rho_a * CD_AD * (vi_TNO_4^2) / Mf / g;
Rs_TNO_4 = 0.2055;
R_CFF_TNO_4 = Rs_TNO_4 * Mf / rho_a / CD_AD;

vis_CFF_TNO_40 = rho_a * CD_AD * (vi_TNO_40^2) / Mf / g;
Rs_TNO_40 = 1.265;
R_CFF_TNO_40 = Rs_TNO_40 * Mf / rho_a / CD_AD;

%% Extending the analysis to all the selected mass: IE - CFF - 4%; TNO -
    NFF - 40%.
R_NFF =  (2 * E_TNO * 0.4 / m_T) * sin(2 * alpha) / g;

vis = rho_a * CD_AD * (2 * E_IE * 0.04 / m_T) / Mf / g;

Rs = readtable('CFF_data_1st.txt');
Rs = Rs{:,:};

R_CFF = Rs * Mf / rho_a / CD_AD;
```

Overall analysis

```
Sub = 'Parahydrogen'; % name of the substance
% Experimental data
m_i = 27; % total mass of the tank [kg], at the beginning it is total liquid (in the storage tank not in the experimental tank)
V_T = 1; % total volume of the tank [m3]
D_T = 1.115; % vessel diameter [m]
m_T = 730; % vessel mass [kg]
P_0 = 101325; % atmospheric pressure [Pa]
T_c = py.CoolProp.CoolProp.PropsSI('Tcrit','',0,'',0,Sub);
gamma = 1.4;
TNT = 4680 * 10^3;  % heat of explosion for TNT [J/kg]
g = 9.81; % acceleration of gravity in [m/s^2]
R = 8.316; % ideal gas constant [J/molK]
Mw = 2.016 * 10^-3; % molar weight [kg/mol]

 % Pressure of the tank before explosion:50 bar [Pa]
 P_exp = 5000000;

%% INITIAL MASSES AND VOLUMES

% Gas saturated temperature at 9.5 bar [K]
P_vap = 9.5 * 10^5; % [Pa]
T_GH2_1 =% CoolProp Data %;
T_GH2_mis = -180 + 273.15; % Gas temperature calculated for the vapour phase [K]

% Gas density at T GH2 1 and 9.5 bar [kg/m 3]
D_GH2_1 =  % CoolProp Data %;
D_GH2_lim = % CoolProp Data %; % Finding the minimum mass at P = 50bar and Tmax=-180C

% Liquid density at T sat and 9.5 bar [kg/m 3]
D_LH2_1 = % CoolProp Data %;

% About m_tot: assume the old scenario, Tvap = T_GH2_1 and P = P_vap -->
% Density is about 13.2kg, so let's consider it as the minimum mass.

m_tot = linspace(D_GH2_lim, m_i, 5);

M_LH2_ft = 10*ones(length(m_tot)); % first try liquid mass

for m = 1:length(m_tot)

% Now it is possible to calculate the volume and the mass of the liquid and the gaseous phase
```

```
err = 1; % initialization of the err variable

while err > 0.00001
  V_LH2_ft(m) = M_LH2_ft(m) / D_LH2_1; % first try liquid Volume
  V_GH2_ft(m) = %%%%%; % first try supercritc Volum
  M_GH2_ft(m) = V_GH2_ft(m) * D_GH2_1; % first try supercritic mass

M_LH2_st(m) = M_LH2_ft (m); % redefinition of the first try liquid mass

M_LH2_ft(m) = %%%; % initialization of the variable second try liquid
    mass


err = abs(M_LH2_st(m) - M_LH2_ft(m)); % definition of the error
end

%%%%

M_GH2 = M_GH2_ft;

% EXPLODING TANK PARAMETERS
% Defining an array for different liquid temperature between T_b
    (boiling temperature at atmospheric pressure) and Tc
T_b = % CoolProp Data %;

T_liquid = T_c; % considering the worst scenario

M_LH2_max (m) = M_LH2 (m);
M_LH2_min = 0;

% Defining an array containing different masses from the minimum to the
    maximum
liquidM (:, m) = linspace(M_LH2_min,M_LH2_max (m),10);

%% Properties
% Density of the liquid at 50 bar and T liquid [kg/m 3]
D_LH2 = % CoolProp Data %;

% Vapour state at NBP
rho_Vb = % CoolProp Data %; % H2 density at NBP in [kg/m3]
h_Vb = % CoolProp Data %;   % H2 enthalpy at NBP in [J/kg]
s_Vb = % CoolProp Data %;   % H2 entropy at NBP in [J/kg*K]
u_Vb = % CoolProp Data %;   % H2 internal energy at NBP in [J/kg]
C_p_Vb = % CoolProp Data %;   % H2 const press specific heat at NBP in
    [J/kg*K]
C_v_Vb = % CoolProp Data %;  % H2 const vol specific heat at NBP in
    [J/kg*K]
```

```
v_Vb = 1 / rho_Vb;                                                      % H2 specific volume at NBP in [m3/kg]

% Liquid state at NBP
rho_Lb = % CoolProp Data %;       % LH2 density at NBP in [kg/m3]
h_Lb = % CoolProp Data %;         % LH2 enthalpy at NBP in [J/kg]
s_Lb = % CoolProp Data %;         % LH2 entropy at NBP in [J/kg*K]
u_Lb = % CoolProp Data %;         % LH2 internal energy at NBP in [J/kg]
C_p_Lb = % CoolProp Data %;       % LH2 const press specific heat at NBP in [J/kg*K]
C_v_Lb = % CoolProp Data %; % LH2 const vol specific heat at NBP in [J/kg*K]

v_Lb = 1 / rho_Lb;

Delta_h = h_Vb - h_Lb;

s_l = % CoolProp Data %; % specific entropy at 50 bar and T_liquid [J/kg/K]
X_l = (s_l-s_Lb)/(s_Vb-s_Lb);      % fraction of the liquid phase
u_l_is = (1-X_l)*u_Lb + X_l*u_Vb;      % specific energy of the liquid phase after the isoentropic expansion [J/kg]
u_l = % CoolProp Data %;     % Specific energy of the liquid phase before the explosion [J/kg]
h_l = % CoolProp Data %;     % Specific hentalpy of the liquid phase before the explosion [J/kg]
cpl = % CoolProp Data %;

for l = 1:1:10
liquidV(l, m) = liquidM(l, m) / D_LH2;
gaseousV(l, m)= V_T - liquidV(l,m); %[m 3]
gaseousM(l,m) = %%%%%; %[kg]
gaseousD(l,m) = gaseousM(l,m) / gaseousV(l,m); %[kg/m 3]



%% IDEAL GASES
f = %%%%; % Definition of f, flashing fraction

V_exp(l,m) = V_T + liquidM(l,m)*(f/gaseousD(l,m) - 1/D_LH2); %[m 3]

E_IE(l,m) = P_exp * V_exp(l,m) * log(P_exp/P_0);


%% REAL GASES
T_gas(l,m) = % CoolProp Data %;    % Gas temperature [K]

```

```
u_v(l,m) = % CoolProp Data %;  % Specific energy of the vapour phase before the explosion [J/kg]
s_v (l,m) = % CoolProp Data %;  % Specific entropy of the vapour phase before the explosion [J/kg]
X_v(l,m) = (s_v(l,m)-s_Lb)/(s_Vb-s_Lb);     % fraction of the vapour phase
u_v_is(l,m) = (1-X_v(l,m))*u_Lb + X_v(l,m)*u_Vb;

U_Vb = u_Vb / (10^6);                         % H2 internal energy at NBP in [MJ/kg]
U_Lb = u_Lb / (10^6);                         % LH2 internal energy at NBP in [MJ/kg]
U_v(l,m) = u_v(l,m) / (10^6);
U_l = u_l / (10^6);

U(l,m) =%%%;               % overall internal energy of the system just before the explosion in [MJ]
        x_1(l,m) = (m_tot(m) * (P_0 / (10^6)) * v_Lb) - (V_T * (P_0 / (10^6))) + (m_tot(m) * U_Lb) - U(l,m);
        x_2(l,m) = %%%%%;
        X(l,m) = x_1(l,m)/ x_2(l,m);

E_TNO_L(l,m) = liquidM(l,m) * (u_l - u_l_is);        % contibution in generate the mech. en. by the liquid in [J]
E_TNO_V(l,m) = gaseousM(l,m) * (u_v(l,m) - u_v_is(l,m));        % contibution in generate the mech. en. by the vapour in [J]
E_TNO(l,m) = E_TNO_L(l,m) + E_TNO_V(l,m);           % mechanical energy generated by the explosion in [J]

end
end

%% TNO - NFF - 40%
alpha_deg = linspace(5,10,6);
alpha = alpha_deg * pi() / 180;
R_NFF_5 =  (2 * E_TNO * 0.4 / m_T) * sin(2 * alpha(1)) / g;
R_NFF_6 =  (2 * E_TNO * 0.4 / m_T) * sin(2 * alpha(2)) / g;
R_NFF_7 =  (2 * E_TNO * 0.4 / m_T) * sin(2 * alpha(3)) / g;
R_NFF_8 =  (2 * E_TNO * 0.4 / m_T) * sin(2 * alpha(4)) / g;
R_NFF_9 =  (2 * E_TNO * 0.4 / m_T) * sin(2 * alpha(5)) / g;
R_NFF_10 =  (2 * E_TNO * 0.4 / m_T) * sin(2 * alpha(6)) / g;


%% IE - CFF - 4% - Drag Coefficient TNO
D_I = 0.75;
vi_IE = sqrt(2 * E_IE * 0.04 / m_T);
rho_a =  1.229;  % density of air in [kg/m3]
```

```
% Fragment 1
CD_AD_1 = %%%%;
m_1 = 124;
vis_1 = rho_a * CD_AD_1 * (vi_IE.^2) / (m_1) / g;
Rs_1 = readtable('CFF_fragm_1.txt');
Rs_1 = Rs_1{:,:};
R_CFF_1 = Rs_1 * (m_1) / rho_a / CD_AD_1;

% Fragment 4
CD_AD_4 = %%%%;
m_4 = 61;
vis_4 = rho_a * CD_AD_4 * (vi_IE.^2) / (m_4) / g;
Rs_4 = readtable('CFF_fragm_4.txt');
Rs_4 = Rs_4{:,:};
R_CFF_4 = Rs_4 * (m_4) / rho_a / CD_AD_4;


% Fragment 38
m_38 = 72;
CD_AD_38 =  %%%%;
vis_38 = rho_a * CD_AD_38 * (vi_IE.^2) / (m_38) / g;
Rs_38 = readtable('CFF_fragm_38.txt');
Rs_38 = Rs_38{:,:};
R_CFF_38 = Rs_38 * (m_38) / rho_a / CD_AD_38;

% Fragment 47
m_47 = 76;
CD_AD_47 =  %%%%;
vis_47 = rho_a * CD_AD_47 * (vi_IE.^2) / (m_47) / g;
Rs_47 = readtable('CFF_fragm_47.txt');
Rs_47 = Rs_47{:,:};
R_CFF_47 = Rs_47 * (m_47) / rho_a / CD_AD_47;

% Fragment 48
m_48 = 65; % [kg]
rho_CS = 7840;
s_ext = 4/1000;
Vstrip_48 = m_48 / rho_CS;
Astrip_48 = %%%; % [m2]
L_ext = 2;
w_48 = Astrip_48 / L_ext;
CD_AD_48 = %%%;
vis_48 = rho_a * CD_AD_48 * (vi_IE.^2) / (m_48) / g;
Rs_48 = readtable('CFF_fragm_48.txt');
Rs_48 = Rs_48{:,:};
R_CFF_48 = Rs_48 * (m_48) / rho_a / CD_AD_48;
```

```
% Fragment 19
m_19 = 261;
w_19 = %%%%;
Astrip_19 = w_19 * L_ext; % [m2]
Vstrip_19 = 261 / rho_CS
CD_AD_19 = %%%%;
vis_19 = rho_a * CD_AD_19 * (vi_IE.^2) / (m_19) / g;
Rs_19 = readtable('CFF_fragm_19.txt');
Rs_19 = Rs_19{:,:};
R_CFF_19 = Rs_19 * (m_19) / rho_a / CD_AD_19;

%% IE - CFF - 4% - Drag Coefficient Cozzani et al.

%% OUTER VESSEL: 2 PTE2 and 2 PL
t_OV = 4*10^-3; % [m]
rho_OV = 7840; % [kg/m3]
r_OV = 1.15/2; % [m]
l_OV = 0;
psi = 0;
l1_48 = 1; % [m]
l2_OV = 2; %  [m]
l1_19 = 2.5; % [m]
A_19 = l2_OV * l1_19;
V_19 = 261 / rho_OV;
t_19 = V_19 / A_19;
C_DA = 0.47;
C_DB = 1.2;
C_DC = 2.05;
C_DD = 1.17;

DF_PTE2_OV = %%%%%;
DF_PL_48 = %%%%%;
DF_PL_19_a = %%%%%;
DF_PL_19_b = %%%%%;


% Fragment 38
m_38 = 72;
vis_38_2 = rho_a * DF_PTE2_OV * (vi_IE.^2) / g;

Rs_38_2 = readtable('CFF_fragm_38_2.txt');
Rs_38_2 = Rs_38_2{:,:};
R_CFF_38_2 = Rs_38_2 / rho_a / DF_PTE2_OV;


% Fragment 47
m_47 = 76;
```

```
vis_47_2 = rho_a * DF_PTE2_OV * (vi_IE.^2) / g;

Rs_47_2 = readtable('CFF_fragm_47_2.txt');
Rs_47_2 = Rs_47_2{:,:};
R_CFF_47_2 = Rs_47_2 / rho_a / DF_PTE2_OV;

% Fragment 48
m_48 = 65; % [kg]
vis_48_2 = rho_a * DF_PL_48* (vi_IE.^2)  / g;

Rs_48_2 = readtable('CFF_fragm_48_2.txt');
Rs_48_2 = Rs_48_2{:,:};
R_CFF_48_2 = Rs_48_2 / rho_a / DF_PL_48;


% Fragment 19  (% "b" = considering the stand as the thickness)
m_19 = 261;
vis_19_2a = rho_a * DF_PL_19_a * (vi_IE.^2) / g;
vis_19_2b = rho_a * DF_PL_19_b * (vi_IE.^2) / g;

Rs_19_2a = readtable('CFF_fragm_19_2a.txt');
Rs_19_2a = Rs_19_2a{:,:};
Rs_19_2b = readtable('CFF_fragm_19_2b.txt');
Rs_19_2b = Rs_19_2b{:,:};

R_CFF_19_2a = Rs_19_2a / rho_a / DF_PL_19_a;
R_CFF_19_2b = Rs_19_2b / rho_a / DF_PL_19_b;

%% INNER VESSEL: 2 PTE2
t_IV = 3/1000;
r_IV = 0.75/2;
rho_IV = 7900;
l_IV = 1.5;
psi_IV = 0;

% Fragment 1
m_1 = 124;
DF_PTE2_IV_1 = %%%%%%;

vis_1_2 = rho_a * DF_PTE2_IV_1 * (vi_IE.^2) / g;

Rs_1_2 = readtable('CFF_fragm_1_2.txt');
Rs_1_2 = Rs_1_2{:,:};
R_CFF_1_2 = Rs_1_2 / rho_a / DF_PTE2_IV_1;

% Fragment 4
m_4 = 61;
```

```
DF_PTE2_IV_4 = %%%%%;

vis_4_2 = rho_a * DF_PTE2_IV_4 * (vi_IE.^2) / g;

Rs_4_2 = readtable('CFF_fragm_4_2.txt');
Rs_4_2 = Rs_4_2{:,:};
R_CFF_4_2 = Rs_4_2 / rho_a / DF_PTE2_IV_4;
```

Initial velocity from video analysis

```
rho_a = 1.229;  % density of air in [kg/m3]
g = 9.81;

t_OV = 4*10^-3; % [m]
rho_OV = 7840; % [kg/m3]
r_OV = 1.15/2; % [m]
l_OV = 0;
psi = 0;
l1_48 = 1; % [m]
l2_OV = 2; %  [m]
l1_19 = 2.5; % [m]
A_19 = l2_OV * l1_19;
V_19 = 261 / rho_OV;
t_19 = V_19 / A_19;
C_DA = 0.47;
C_DB = 1.2;
C_DC = 2.05;
C_DD = 1.17;

DF_PTE2_OV = %%%%%;
DF_PL_48 = %%%%%;

%% Fragment 38
m_38 = 72;
vi_exp_38 = 67;
alpha_38 = linspace(10,15,6) * pi()/180;
R_NFF_38 = vi_exp_38^2 * sin(2*alpha_38) / g;
% CFF
vis_38_exp = rho_a * DF_PTE2_OV * (vi_exp_38^2) / g;
Rs_exp_38 = 1.555;
R_CFF_exp_38 = Rs_exp_38 / rho_a / DF_PTE2_OV;

%% Fragment 47
m_47 = 76;
vi_exp_47 = 60;
%NFF
alpha_47 = linspace(5,10,6) * pi()/180;
R_NFF_47 = vi_exp_47^2 * sin(2*alpha_47) / g;
% CFF
vis_47_exp = rho_a * DF_PTE2_OV * (vi_exp_47^2) / g;
Rs_exp_47 = 1.333 ;
R_CFF_exp_47 = Rs_exp_47 / rho_a / DF_PTE2_OV;

%% Fragment 48
m_48 = 65; % [kg]
```

```
vi_exp_48 = 121;
% NFF
alpha_48 = linspace(10,15,6) * pi()/180;
R_NFF_48 = vi_exp_48^2 * sin(2*alpha_48) / g;
% CFF
vis_48_exp = rho_a * DF_PL_48 * (vi_exp_48^2) / g;
Rs_exp_48 = 4.36;
R_CFF_exp_48 = Rs_exp_48 / rho_a / DF_PTE2_OV;
```

Initial velocity: range

```
    % Using Drag Fractor of Cozzani et al. "Assessment of missile hazards:
% Evaluation of the fragment number and drag factors"
v = linspace(40, 120, 9);
alpha = linspace(0, 20, 9);

Data = readtable('CFF_data.txt');
Data = Data{:,:};

% NFF
for i = 1:length(v)
    for j = 1:length(alpha)
        g = 9.81;
        R_NFF(i,j) = v(i)^2 * sin(2*alpha(j)*pi/180) / g;
    end
end

m_1 = 124;
m_4 = 61;
m_19 = 261;
m_38 = 72;
m_47 = 76;
m_48 = 65;

% Drag coefficient
C_DA = 0.47;
C_DB = 1.2;
C_DC = 2.05;
C_DD = 1.17;
t_OV = 4*10^-3;% [m]
rho_OV = 7840; % [kg/m3]
r_OV = 1.15/2; % [m]
l_OV = 0;
psi = 0;
l1_48 = 1; % [m]
l2_OV = 2; %  [m]
l1_19 = 2.5; % [m]
A_19 = l2_OV * l1_19;
V_19 = 261 / rho_OV;
t_19 = V_19 / A_19;

t_IV = 3/1000;
r_IV = 0.75/2;
rho_IV = 7900;
l_IV = 1.5;
```

```
psi_IV = 0;

DF_PTE2_1 = %%%%%;
DF_PTE2_4 = %%%%%;
DF_PTE2_OV = %%%%%; % for fragm no. 47 and 38
DF_PL_19 = %%%%%;
DF_PL_48 = %%%%%;

Rs = readtable('Rs_InitialVelocity.txt');
Rs = Rs{:,:};

%% fragment 1
for k = 1:length(v)
    rho_a = 1.229; % density of air in [kg/m3]
    vis_1(k) = rho_a * DF_PTE2_1 * (v(k)^2) / g;

  Rs_1 = Rs(1,:);
  R_CFF_1(k) = Rs_1(k)/ rho_a / DF_PTE2_1;
    end

%% fragment 4
for k = 1:length(v)
    rho_a = 1.229; % density of air in [kg/m3]
    vis_4(k) = rho_a * DF_PTE2_4 * (v(k)^2) / g;

 Rs_4 = Rs(2,:);
 R_CFF_4= Rs_4 / rho_a / DF_PTE2_4;
    end

%% fragment 19
for k = 1:length(v)
    rho_a = 1.229; % density of air in [kg/m3]
    vis_19(k) = rho_a * DF_PL_19 * (v(k)^2) / g;

    Rs_19 = Rs(3,:);
    R_CFF_19(k) = Rs_19(k) / rho_a / DF_PL_19;
end

%% fragment 38
for k = 1:length(v)
    rho_a = 1.229; % density of air in [kg/m3]
    vis_38(k) = rho_a * DF_PTE2_OV * (v(k)^2) / g;

  Rs_38 = Rs(4,:);
  R_CFF_38(k) = Rs_38(k) / rho_a / DF_PTE2_OV;
end
```

```
%% fragment 47
for k = 1:length(v)
    rho_a =  1.229;  % density of air in [kg/m3]
    vis_47(k) = rho_a * DF_PTE2_OV * (v(k)^2) / g;

   Rs_47 = Rs(5,:);
   R_CFF_47(k) = Rs_47(k) / rho_a / DF_PTE2_OV;
end

%% fragment 48
for k = 1:length(v)
    rho_a =  1.229;  % density of air in [kg/m3]
    vis_48(k) = rho_a * DF_PL_48 * (v(k)^2) / g;

   Rs_48 = Rs(6,:);
   R_CFF_48(k) = Rs_48(k) / rho_a / DF_PL_48 ;
end

R_CFF = [R_CFF_1; R_CFF_4; R_CFF_19; R_CFF_38; R_CFF_47; R_CFF_48];
R_CFF.'
```

Bibliography

[1] IEA (2019). *The Future of Hydrogen*. URL: https://www.iea.org/reports/the-future-of-hydrogen.

[2] Kaveh Mazloomi and Chandima Gomes. “Hydrogen as an energy carrier: Prospects and challenges”. In: *Renewable and Sustainable Energy Reviews* 16.5 (2012), pp. 3024–3033.

[3] L Gas. “Lower and upper explosive limits for flammable gases and vapors (LEL/UEL)”. In: *Matheson gas products* 22 (2013).

[4] Giovanni Nicoletti et al. “A technical and environmental comparison between hydrogen and some fossil fuels”. In: *Energy Conversion and Management* 89 (2015), pp. 205–213.

[5] I. A. Hassan et al. “Hydrogen storage technologies for stationary and mobile applications: Review, analysis and perspectives”. In: *Renewable and Sustainable Energy Reviews* 149 (Oct. 2021). ISSN: 18790690. DOI: 10.1016/j.rser.2021.111311.

[6] *NIST Chemistry WebBook*. URL: https://webbook.nist.gov/.

[7] Federico Ustolin, Nicola Paltrinieri, and Gabriele Landucci. “An innovative and comprehensive approach for the consequence analysis of liquid hydrogen vessel explosions”. In: *Journal of Loss Prevention in the Process Industries* 68 (Nov. 2020). ISSN: 09504230. DOI: 10.1016/j.jlp.2020.104323.

[8] Ramin Moradi and Katrina M. Groth. “Hydrogen storage and delivery: Review of the state of the art technologies and risk and reliability analysis”. In: *International Journal of Hydrogen Energy* 44 (23 May 2019), pp. 12254–12269. ISSN: 03603199. DOI: 10.1016/j.ijhydene.2019.03.041.

[9] H. Barthelemy, M. Weber, and F. Barbier. “Hydrogen storage: Recent improvements and industrial perspectives”. In: *International Journal of Hydrogen Energy* 42 (11 Mar. 2017), pp. 7254–7262. ISSN: 03603199. DOI: 10.1016/j.ijhydene.2016.03.178.

[10] Zhao Yanxing et al. “Thermodynamics analysis of hydrogen storage based on compressed gaseous hydrogen, liquid hydrogen and cryo-compressed hydrogen”. In: *International Journal of Hydrogen Energy* 44.31 (2019), pp. 16833–16840.

[11] AV Zhuzhgov et al. “Low-temperature conversion of ortho-hydrogen into liquid para-hydrogen: Process and catalysts. review”. In: *Catalysis in Industry* 10.1 (2018), pp. 9–19.

[12] Randall F Barron and Gregory F Nellis. *Cryogenic heat transfer.* CRC press, 2017.

[13] K Kunze. “Performance of a cryo-compressed hydrogen storage”. In: *World Hydrogen Energy Conference-WHEC 2012*. 2012.

[14] *Process Safety Glossary.* URL: `https://www.aiche.org/ccps/resources/glossary`.

[15] Jaffee A Suardin et al. “Field experiments on high expansion (HEX) foam application for controlling LNG pool fire”. In: *Journal of hazardous materials* 165.1-3 (2009), pp. 612–622.

[16] Leonardo Giannini. “BOILING LIQUID EXPANDING VAPOR EXPLOSION FOR LIQUID HYDROGEN”. 2022.

[17] Kees van Wingerden et al. “Medium-scale tests to investigate the possibility and effects of BLEVEs of storage vessels containing liquified hydrogen”. In: *Chemical Engineering Transactions* 90 (2022), pp. 547–552.

[18] C.J.H. van den Bosch and R.A.P.M. Weterings. *Methods for the Calculation of Physical Effect: Due to Releases of Hazardous Materials (liquids and Gases) : Yellow Book*. Director-General of Labour, 2005. URL: `https://books.google.no/books?id=6PHYZwEACAAJ`.

[19] Mohammad Esmaeilnia Omran and Somayeh Mollaei. “Comparison between RC frames and concrete shear wall subjected to blast load by finite element method”. In: ().

[20] Amos Necci et al. “Assessment of domino effect: State of the art and research Needs”. In: *Reliability Engineering & System Safety* 143 (2015), pp. 3–18.

[21] B Hemmatian, E Planas, and J Casal. “On BLEVE definition, the significance of superheat limit temperature (T-sl) and LNG BLEVE’s”. In: *Journal of Loss Prevention in the Process Industries* 40 (2016), pp. 81–81.

[22] J. M. Salla, M. Demichela, and J. Casal. “BLEVE: A new approach to the superheat limit temperature”. In: *Journal of Loss Prevention in the Process Industries* 19 (6 Nov. 2006), pp. 690–700. ISSN: 09504230. DOI: `10.1016/j.jlp.2006.04.004`.

[23] Federico Ustolin. “Modelling of Accident Scenarios from Liquid Hydrogen transport and Use”. In: (2021).

[24] Tasneem Abbasi and SA Abbasi. “The boiling liquid expanding vapour explosion (BLEVE): Mechanism, consequence assessment, management”. In: *Journal of Hazardous Materials* 141.3 (2007), pp. 489–519.

[25] Nicola Paltrinieri et al. “Risk reduction in road and rail LPG transportation by passive fire protection”. In: *Journal of hazardous materials* 167.1-3 (2009), pp. 332–344.

[26] Robert C Reid, John M Prausnitz, and Bruce E Poling. “The properties of gases and liquids”. In: (1987).

[27] Nicola Paltrinieri, Knut Øien, and Valerio Cozzani. “Assessment and comparison of two early warning indicator methods in the perspective of prevention of atypical accident scenarios”. In: *Reliability Engineering & System Safety* 108 (2012), pp. 21–31.

[28] K Pehr. *ASPECTS OF SAFETY AND ACCEPTANCE OF LH, TANK SYSTEMS IN PASSENGER CARS**. 1996, p. 387.

[29] Richard W. Prugh. “Quantitative evaluation of ’BLEVE’ hazards”. In: *Journal of Fire Protection Engineering* 3 (1 1991), pp. 9–24. ISSN: 10423915. DOI: 10.1177/104239159100300102.

[30] Harold L Brode. “Blast wave from a spherical charge”. In: *The Physics of Fluids* 2.2 (1959), pp. 217–229.

[31] H.C. Van Ness J.M. Smith. “Introduction to Chemical Engineering”. In: (1996).

[32] Daniel A Crowl. “Using thermodynamic availability to determine the energy of explosion for compressed gases”. In: *Plant/Operations Progress* 11.2 (1992), pp. 47–49.

[33] E. Planas-Cuchi, J. M. Salla, and J. Casal. “Calculating overpressure from BLEVE explosions”. In: *Journal of Loss Prevention in the Process Industries* 17 (6 Nov. 2004), pp. 431–436. ISSN: 09504230. DOI: 10.1016/j.jlp.2004.08.002.

[34] Joaquim Casal and Josep M. Salla. “Using liquid superheating energy for a quick estimation of overpressure in BLEVEs and similar explosions”. In: *Journal of Hazardous Materials* 137 (3 Oct. 2006), pp. 1321–1327. ISSN: 03043894. DOI: 10.1016/j.jhazmat.2006.05.001.

[35] B. Genova, M. Silvestrini, and F.J. Leon Trujillo. "Evaluation of the blast-wave overpressure and fragments initial velocity for a BLEVE event via empirical correlations derived by a simplified model of released energy". In: *Journal of Loss Prevention in the Process Industries* 21.1 (2008), pp. 110–117. ISSN: 0950-4230. DOI: https://doi.org/10.1016/j.jlp.2007.11.004. URL: https://www.sciencedirect.com/science/article/pii/S0950423007001398.

[36] A.M. Birk, C. Davison, and M. Cunningham. "Blast overpressures from medium scale BLEVE tests". In: *Journal of Loss Prevention in the Process Industries* 20.3 (2007), pp. 194–206. ISSN: 0950-4230. DOI: https://doi.org/10.1016/j.jlp.2007.03.001. URL: https://www.sciencedirect.com/science/article/pii/S095042300700006X.

[37] Ashok Kumar. *Guidelines for evaluating the characteristics of vapor cloud explosions, flash fires, and bleves. Center for Chemical Process Safety (CCPS) of the AIChE, Published by the American Institute of Chemical Engineers, New York, NY (1994), 387 pages,[ISBN: 0-8169-0474-X], US List Price: 150.* 1996.

[38] "Chapter 17 - Explosion". In: *Lees' Loss Prevention in the Process Industries (Fourth Edition)*. Ed. by Sam Mannan. Fourth Edition. Oxford: Butterworth-Heinemann, 2012, pp. 1367–1678. ISBN: 978-0-12-397189-0. DOI: https://doi.org/10.1016/B978-0-12-397189-0.00017-3. URL: https://www.sciencedirect.com/science/article/pii/B9780123971890000173.

[39] "CHAPTER 6 - Fragmentation and Missile Effects". In: *Explosion Hazards and Evaluation*. Ed. by W.E. BAKER et al. Vol. 5. Fundamental Studies in Engineering. Elsevier, 1983, pp. 463–528. DOI: https://doi.org/10.1016/B978-0-444-42094-7.50014-8. URL: https://www.sciencedirect.com/science/article/pii/B9780444420947500148.

[40] NASA. *Air properties definitions*. 2020. URL: https://www.grc.nasa.%20gov/www/k-12/BGP/airprop.html.

[41] Joan Charmant Contrib. *Kinovea*. Version 0.9.5. URL: https://www.kinovea.org/.

[42] Gianfilippo Gubinelli and Valerio Cozzani. "Assessment of missile hazards: Identification of reference fragmentation patterns". In: *Journal of Hazardous Materials* 163 (2-3 Apr. 2009), pp. 1008–1018. ISSN: 03043894. DOI: 10.1016/j.jhazmat.2008.07.056.

[43] Gianfilippo Gubinelli, Severino Zanelli, and Valerio Cozzani. "A simplified model for the assessment of the impact probability of fragments". In: *Journal of Hazardous Materials* 116 (3 Dec. 2004), pp. 175–187. ISSN: 03043894. DOI: 10.1016/j.jhazmat.2004.09.002.

[44] Ahmed Mébarki et al. “Structural fragments and explosions in industrial facilities. Part I: Probabilistic description of the source terms”. In: *Journal of Loss Prevention in the Process Industries* 22.4 (2009), pp. 408–416.

[45] P.L. Holden. “Assessment of missile hazards: review of incident experience relevant to major hazard plant”. In: *Safety and Reliability Directorate, Health Safety Directorate* (1988).

[46] A. Mébarki et al. “Structural fragments and explosions in industrial facilities. Part I: Probabilistic description of the source terms”. In: *Journal of Loss Prevention in the Process Industries* 22 (4 July 2009), pp. 408–416. ISSN: 09504230. DOI: 10.1016/j.jlp.2009.02.006.

[47] Ian H Bell et al. “Pure and pseudo-pure fluid thermophysical property evaluation and the open-source thermophysical property library CoolProp”. In: *Industrial & engineering chemistry research* 53.6 (2014), pp. 2498–2508.

[48] Gianfilippo Gubinelli and Valerio Cozzani. “Assessment of missile hazards: evaluation of the fragment number and drag factors”. In: *Journal of Hazardous Materials* 161.1 (2009), pp. 439–449.

NTNU

Norwegian University of
Science and Technology